CHAPTER 3: RESULTS AND DISCUSSIONS

Part 1: Development and Evaluation of Biopolymeric PNAG NPs for Advanced Skin Regeneration in Wound Healing

The outcome of this part:

1. **Published in Materials Advances:** *In vivo* potential of polymeric N-acryloyl-glycine nanoparticles with anti-inflammatory activities for wound healing
2. **Published an Indian Patent:** Patent Application no.: 02311051276, 31/07/2023.

Part 2: Potentiation of Wound Healing Activity of PNAG NPs with NO for Enhanced Skin Regeneration

The outcome of this part:

1. **Published in Nanoscale:** Nitric oxide releasing novel amino acid-derived polymeric nanotherapeutic with anti-inflammatory properties for rapid wound tissue regeneration
2. **Published an Indian Patent:** Patent Application No. 202311041625, 19/06/2023.

Part 3: Comprehensive Biological Activity Assessment of Metal Oxides in Wound Healing

The outcome of this part:

The outcome of Part III is the validation and reproducibility of synthesis method of metal oxide NPs and their biological evaluation (hemolysis, cytocompatibility, angiogenesis, and scratch wound healing assay). These NPs exhibit significant antimicrobial activity, which is useful for microbial infected wounds. Their integration into wound care offers dual benefits: promoting tissue regeneration and combating infections. This dual functionality is crucial for developing next-generation wound care treatments that address both regenerative and antimicrobial needs.

CHAPTER 3: PART I

3.1 Development and Evaluation of Biopolymeric PNAG NPs for Advanced Skin Regeneration in Wound Healing

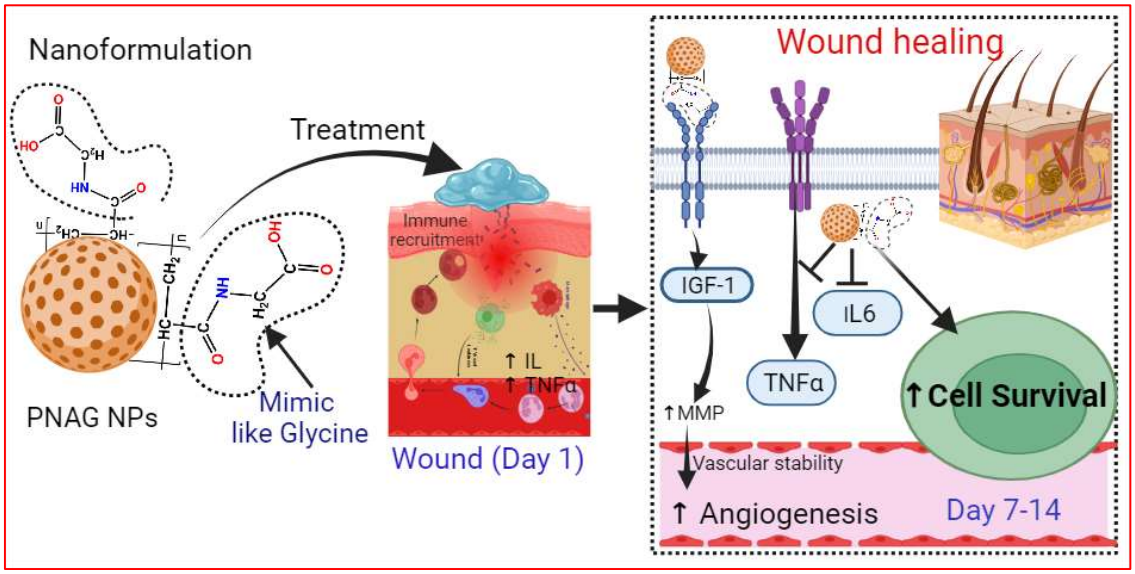

Figure 3.1.1: Prepared PNAG NPs are formulated into nanoformulation, and applied on rats' wounds. Accelerated wound healing was observed due to a reduction in inflammation and induction of cell migration, proliferation and angiogenesis.

3.1.1 ABSTRACT

An optimal wound-healing process necessitates intricately coordinated and regulated interactions between the immune and biological systems, given that long-term wounds present severe clinical challenges, rendering patients susceptible to potentially life-threatening microbial infections. Consequently, imperative efforts are directed towards developing innovative treatments and therapeutic strategies. In this study, we devised a formulation based on polymeric PNAG NPs to expedite skin restoration. PNAG NPs synthesized via the mini-emulsion radical polymerization technique exhibited a diameter of approximately 35 nm and were incorporated into an ointment base for application in WH. The resultant PNAG nanoformulation demonstrated characteristics such as biocompatibility, hemocompatibility, proliferation enhancement, and migration facilitation. *In vivo* assessments revealed a remarkable ~31% increase in WH efficiency

compared to the control group. Periodic monitoring of inflammatory markers, namely TNF-α and IL6, exhibited temporal fluctuations in their levels. TNF-α levels followed a similar pattern in both the PNAG treatment group and the control, while the IL6 expression was lower in the PNAG treatment group.

The elevated level of IGF-1 in the PNAG treatment group correlated with increased angiogenesis and subsequent accelerated WH. This investigation illustrated that PNAG NPs orchestrate rapid coordination between cell proliferation and migration, exert anti-inflammatory effects, and facilitate simultaneous regeneration of skin tissues without the need for external synergistic factors such as drugs, genes, or cells. In conclusion, the intriguing findings suggest that PNAG NPs hold promise in overcoming existing challenges in WH and may serve as a potential material for regenerative applications.

3.1.2 INTRODUCTION

Cutaneous tissue functions as a pivotal organ, crucial for safeguarding the body against the potential loss of fluids, electrolytes, and nutrients while simultaneously serving as a barrier against external threats [1, 2]. The integrity of this protective function is compromised in instances of extensive tissue damage caused by mechanical, chemical, physical, or biological factors, leading to the development of cutaneous wounds and, in severe cases, multi-organ failure [3]. Although the innate immune system promptly initiates a response to such tissue damage [4, 5], various internal factors, such as diabetes and malnutrition, as well as external conditions like infections and secondary trauma, can disrupt the intricate mechanisms of WH [6], This impairment poses a significant global healthcare challenge [7]. The projected annual costs associated with impaired WH are anticipated to range from 28.1 to 96.8 billion USD by the year 2030 [8]. Furthermore, it has been reported that over 38 million chronic wound infections are correlated with unfavourable prognoses [9]. The persistence of wounds, particularly in the elderly

population, contributes to heightened rates of co-morbidities and mortality [10]. Notably, diabetic foot ulcers (DFU) alone exhibit a 5-year death rate ranging from 43% to 55%, surpassing which is more than the mortality rate associated with certain cancers [11]. Consequently, there exists a pressing need for research focused on promoting the restoration of healthy skin through cost-effective therapeutic interventions, concurrently with the exploration of optimal biomaterials for facilitating WH.

Critical attributes for WH materials encompass porosity, adhesion, and high mechanical strength [12], with careful consideration to mitigate potential toxicity issues. The synergistic conjugation of materials, encompassing polymers and nanomaterials, holds promise for enhancing healing efficiency. Notably, the incorporation of nanomaterials, such as Ag NPs within alginate/ gelatin hydrogels [13], presents advantages surpassing those of conventional WH materials [14]. Despite their benefits, these materials may fall short in fully adapting to the dynamic nature and microenvironment of the wound and its healing process, hindering the anticipated enhancement of healing efficiency. In recent investigations, natural polymers have gained attention for their inherent biocompatibility, biodegradability, and structural resemblance to biological tissues, positioning them as potential candidates for wound treatment [15]. Alternatively, polymeric carriers facilitating the delivery of antibiotics, growth factors, or therapeutic stem cells represent viable options for WH [16-18]. However, the application of these approaches is hindered by drug-associated side effects and elevated costs. Conventional dressing materials, such as gauze, bandages, and cotton wool, exhibit limitations in preventing wound bed desiccation due to their high absorbency of wound exudates, thereby attracting microbes and fostering infections that compromise regenerative tissues.

Similarly, synthetic polymers, characterized by high hydrophobicity, pose challenges in cell adhesion during the WH process [19]. Existing clinical wound dressings often fail to

support the controlled growth of wound-healing cells [20]. Consequently, despite the prevalent use of numerous wound dressings in current clinical settings, significant unmet needs persist within the realm of WH materials.

In response to these challenges, polymeric NPs emerge as a burgeoning solution with increasing interest. Wound-healing polymeric NPs exhibit the potential to modulate various cellular and molecular mechanisms within the wound microenvironment, manifesting anti-inflammatory and angiogenic actions. This transformative capacity holds the promise of converting a non-healing environment into one conducive to healing, thereby addressing some of the limitations posed by existing WH materials [21].

In this study, we endeavoured to address certain limitations and enhance the efficacy of WH, specifically focusing on the parameters of repair/healing time. To achieve this, we synthesized poly(N-acryloyl-glycine) (PNAG) polymer and subsequently prepared it into NPs through a free radical emulsion polymerization process. The PNAG polymer itself is derived from a weak polyacid monomer, synthesized using the Schotten-Baumann reaction mechanism involving acryloyl chloride and glycine amino acid. The fabrication of PNAG NPs aimed to preserve the haemostatic activity associated with the carboxyl groups present in the PNAG polymer, with a primary goal of enhancing WH efficiency. Extensive assessments were conducted to evaluate the biocompatibility and hemocompatibility of PNAG NPs, ensuring their non-toxic and non-antigenic nature when interfacing with living tissues or biological systems.

Furthermore, the proliferative and migratory performance of PNAG NPs was systematically investigated through a scratch wound assay, utilizing L929 cell line (mouse fibroblast) as a model system. This analysis provided insights into the efficiency of PNAG NPs in promoting cellular activities such as proliferation and migration critical for WH. The angiogenic potential of PNAG NPs was explored using the chicken embryo

membrane angiogenesis (CEMA) assay under *in ovo* conditions. This investigation aimed to ascertain the capability of PNAG NPs to contribute to the development of blood vasculature, a pivotal aspect for ensuring effective and prompt WH.

Subsequently, a nanoformulation derived from PNAG NPs was formulated, and an *in vivo* dermal irritation study was conducted to evaluate its biocompatibility and potential adverse effects. Furthermore, an assessment of the *in vivo* WH efficacy of PNAG NPs was conducted utilizing a rat model. The study further involved in a comprehensive temporal profiling of pro-inflammatory cytokines and chemokines during the WH process. The obtained results were meticulously compared to those of control samples to ascertain the effectiveness of PNAG NPs in facilitating and expediting the WH process.

3.1.3 EXPERIMENTAL

3.1.3.1 Synthesis of NAG Monomer and PNAG NPs

The method has been described in the experimental section in Chapter 2 (Page No. 62-63, Section 2.2.1).

3.1.3.2 Characterization of NAG Monomer and PNAG NPs

The method has been described in the experimental section in Chapter 2 (Page No. 65-67, Section 2.3).

3.1.3.3 Biocompatibility and Hemocompatibility of PNAG NPs

The methodology for assessment of biocompatibility and hemocompatibility have been described in the experimental section in Chapter 2 (Page No. 67, Section 2.4.1, and Page No. 70, Section 2.5, respectively).

3.1.3.4 Cell Migration and Proliferation Assay

The method adopted for assessment of cell proliferation and migration potentioal of PNAG NPs has been described in the experimental section in Chapter 2 (Page No. 69, Section 2.4.2).

3.1.3.5 Angiogenesis Assay

The angiogenic effect of PNAG NPs were evaluated using CAM assay for which methodology has been described in the experimental section in Chapter 2 (Page No. 77, Section 2.8.1).

3.1.3.6 Development of PNAG Nanoformulation and Quality Evaluation

Nanoformulation development and quality evaluation has been described in the experimental section of Chapter 2 (Page. No. 73-76, Section 2.7).

3.1.3.7 *In vivo* Skin Irritation and Skin Sensitivity Evaluation

In vivo skin irritation and skin sensitivity evaluation of PNAG nanoformulation has been described in the experimental section of Chapter 2 (Page No. 79, Section 2.8.3).

3.1.3.8 *In vivo* Wound Healing Study

The methodology and protocol for conducting *in vivo* WH study is described in experimental section of Chapter 2 (Page No. 80, Section 2.8.4).

3.1.3.9 Histological Analysis

The methodology and protocol for conducting histological evaluation is described in experimental section of Chapter 2 (Page No. 81, Section 2.8.5).

3.1.3.10 Immunomarker Evalution During the Treatment with PNAG Nanoformulation

The methodology for the evaluation of impact of PNAG nanoformulation on immunomarkers has been described in experimental section of Chapter 2 (Page No. 81, Section 2.8.6).

3.1.3.11 Statistical Analysis

Statistical analysis was conducted using Origin 2021 software and data are expressed as mean values (±SD). Statistics applied on the work are described in the experimental section of Chapter 2 (Page No. 83, Section 2.9).

3.1.4 RESULTS

3.1.4.1 Synthesis and Characterization of NAG Monomer and PNAG NPs

The synthesis of NAG monomer was achieved through the adaptation of the Schotten-Baumann reaction mechanism. Schotten-Baumann reaction mechanism is operating in an alkaline medium, facilitates the synthesis of amides by reacting acyl chlorides and amines. The NAG monomer synthesis process is illustrated in Figure 3.1.3.

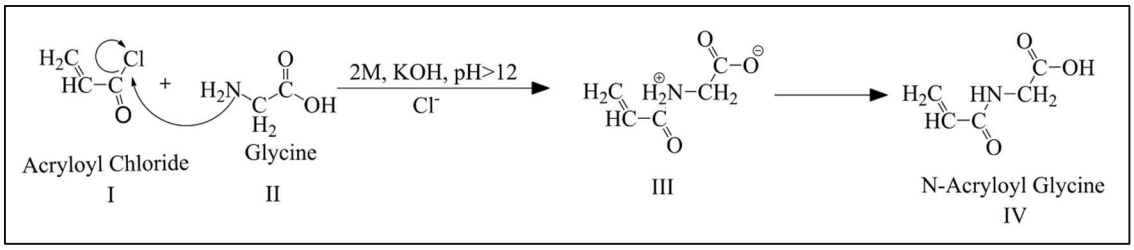

Figure 3.1.2: Synthesis mechanism of N-Acryloyl Glycine (NAG) monomer

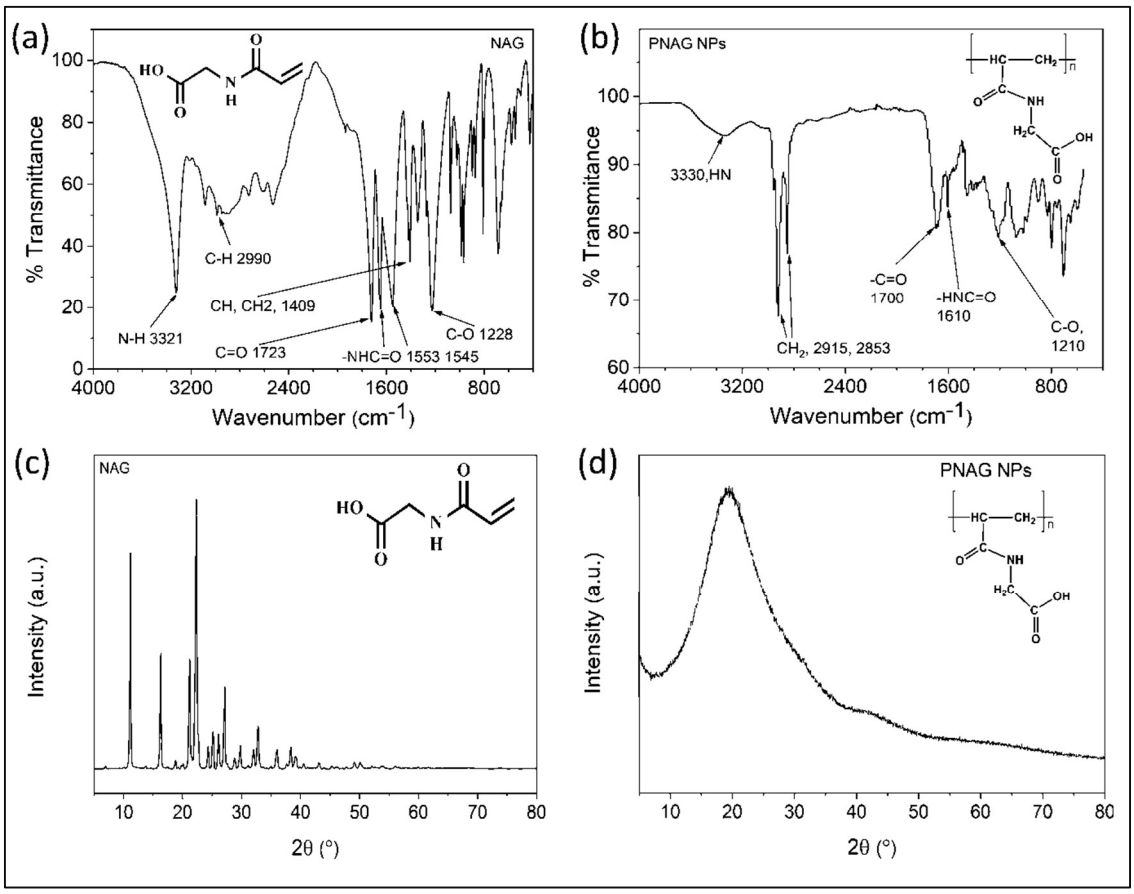

Figure 3.1.3: FTIR spectra and XRD pattern of NAG monomer and PNAG NPs. FTIR spectra show the absorption bands for (a) NAG monomer and (b) PNAG polymer; the XRD pattern (c) shows that NAG monomer is highly crystalline, while (d) the synthesised PNAG NPs show reduced crystallinity compared to the NAG monomer.

Initially, acryloyl chloride (I) and glycine amino acid (II) underwent reaction in an alkaline solution, resulting in the formation of acryloylated amino acid (III). Subsequently, acryloylated amino acid experienced a charge rearrangement, yielding the NAG monomer (IV) (Figure 3.1.2). The synthesis of the NAG monomer was validated by analysing the FTIR spectrum (Figure 3.1.3a), revealing functional groups at 3321 cm^{-1} for secondary amine (-NH-), 2990 cm^{-1} for alkane (-CH-), 2728 cm^{-1} for carboxylic group (-COOH), 1723 cm^{-1} for carbonyl ketone (-C=O) group attached to an acid group, and 1553 and 1545 cm^{-1} for carbonyl ketone attached to amide group.

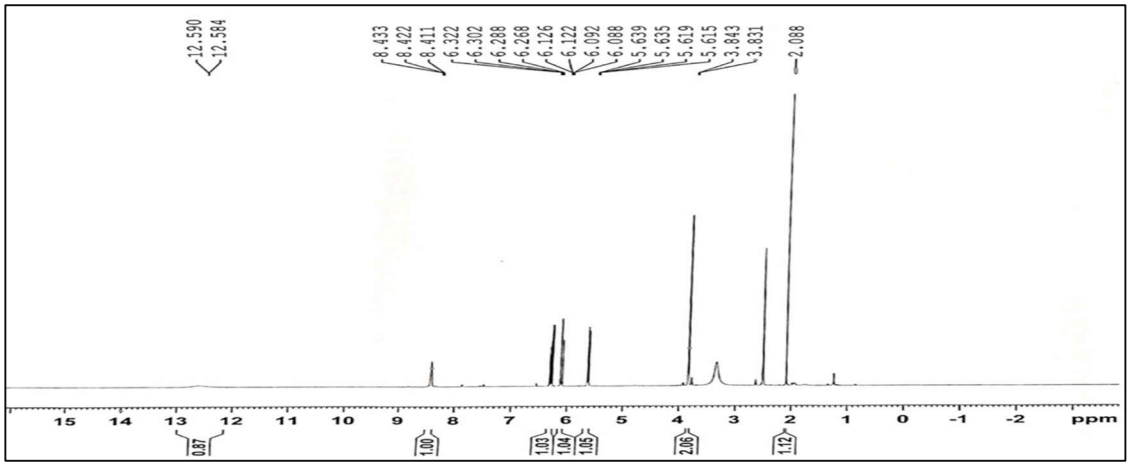

Figure 3.1.4: ^{1}H-NMR spectrum of N-acryloyl-glycine (NAG), monomer recorded in DMSO deuterated (500 MHz)

Structural confirmation of NAG monomer was further obtained through ^{1}H NMR (Figure 3.1.4) and ^{13}C-NMR analyses (Figure 3.1.5) in DMSO-D6 solvent. NMR revealing characteristic peaks at 12.57 ppm (1H, s), 8.41 ppm (-CONH, t), 6.26 and 6.09 ppm (-CONH-, 1H, cis, t), 5.63 and 5.61 ppm (-CONH-, 1H, trans, t), 3.844 and 3.832 ppm (-CH_2, CH-, 2H, vinyl hydrogen, d), 3.5 ppm (-CH_2-, 2H, d), and 2.56 ppm (=CH-, 1H, t). The ^{13}C-NMR spectrum provided valuable information, with notable peaks at 171.66 ppm (-CO-OH), 165.37 ppm (-CO-NH), 131.77 and 126.12 ppm (H_2C=CH-), and 41.10 ppm (-N-CH2).

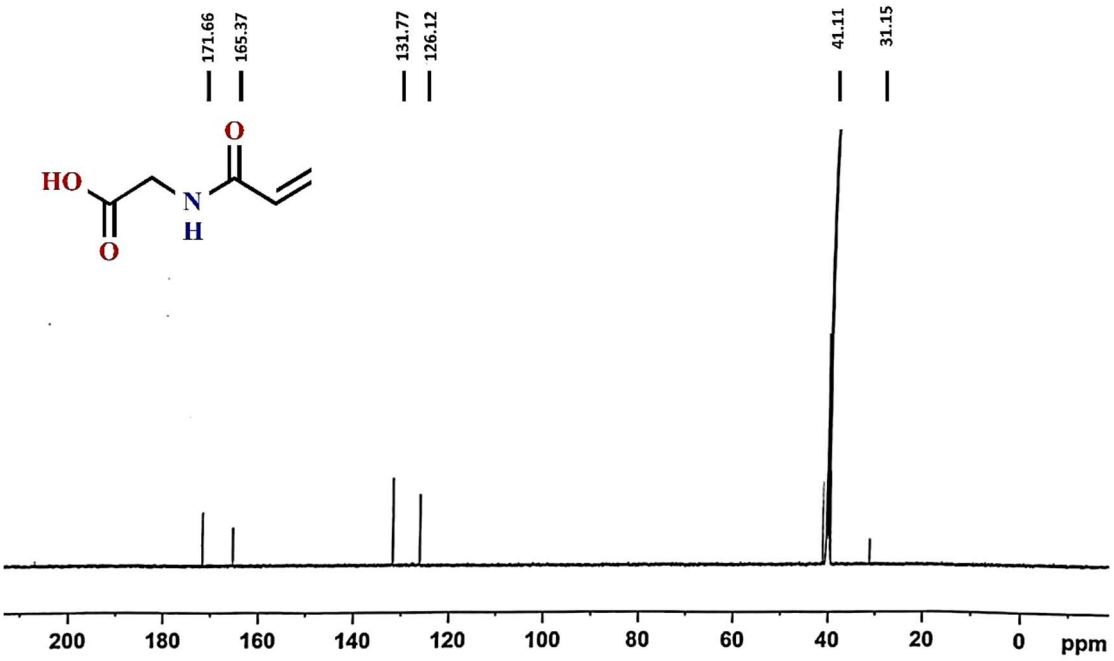

Figure 3.1.5: ^{13}C-NMR spectrum of N-acryloyl-glycine (NAG), monomer recorded in DMSO deuterated (500 MHz)

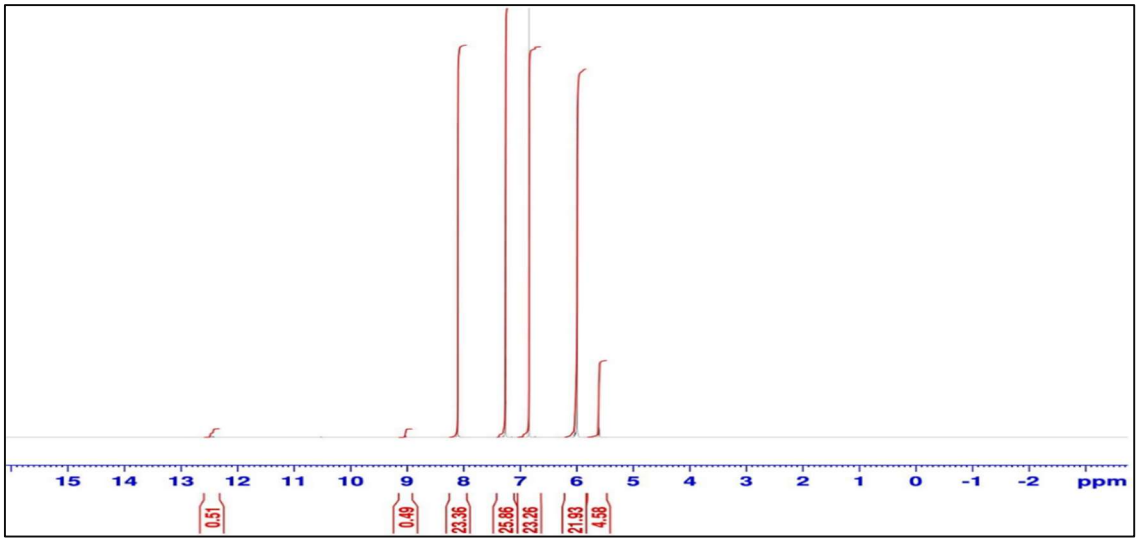

Figure 3.1.6: ^{1}H-NMR spectrum of Poly-N-acryloyl-glycine (PNAG), monomer recorded in $CDCl_3$ deuterated (500 MHz)

The synthesized NAG monomer served as the precursor for a mini-emulsion radical polymerization process. This method yielded complex polymeric particle structures through the mini-emulsification of the NAG monomer in an oil phase (toluene), forming tiny droplets of monomer particles. AIBN, an organic soluble radical initiator, activated at a temperature range of 70-75 °C, initiating radical polymerization at the interfaces of

NAG monomer droplets.

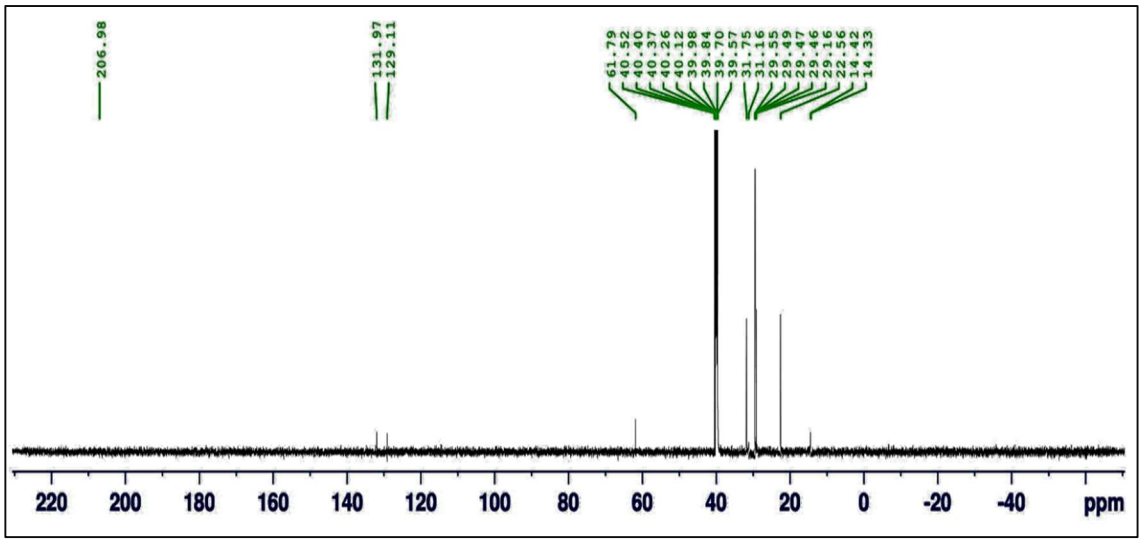

Figure 3.1.7: ^{13}C-NMR spectrum of Poly-N-acryloyl-glycine (PNAG), monomer recorded in $CDCl_3$ deuterated (500 MHz)

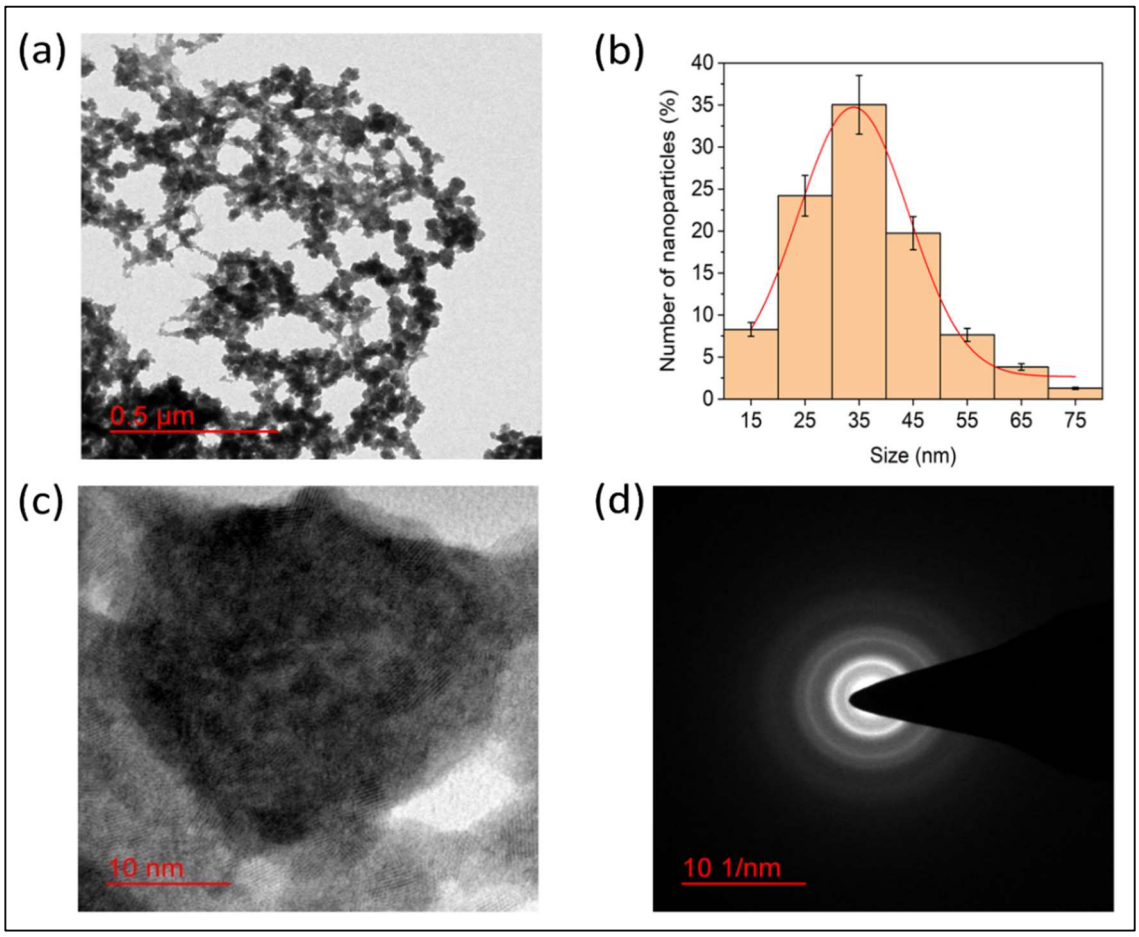

Figure 3.1.8: TEM micrograph and particle size distribution of PNAG NPs; (a) reveal net-like co-connect arrangements; (b) particle size distribution of PNAG NPs calculated considering 300 particles; (c) shows porous particle structure and (d) SAED pattern shows diffused rings and confirms semi-crystalline nature of PNAG NPs.

The above process generated particles with an oily core surrounded by a thin polymeric linear membrane. Cross-linking with DVB stabilized the polymeric linear membrane, providing particle stability and introducing porosity. The co-stabilizer, hexadecane (HD) an alkane, prevented Ostwald ripening. Polymerization occurred at an elevated temperature (75-80 °C), promoting porosity through the evaporation of the oily core. The surfactant SDS was employed to prevent emulsion coalescence and acted as a primary stabilizer for the particles. While it is possible to prepare NPs without surfactant, it adversely affects their physical stability, leading to aggregate formation during storage under such conditions.

The structural characteristics of PNAG (NPs) were extensively elucidated through characterization, including FTIR spectroscopy (Figure 3.1.3b), ^{1}H NMR (Figure 3.1.4), and ^{13}C-NMR (Figure 3.1.5).

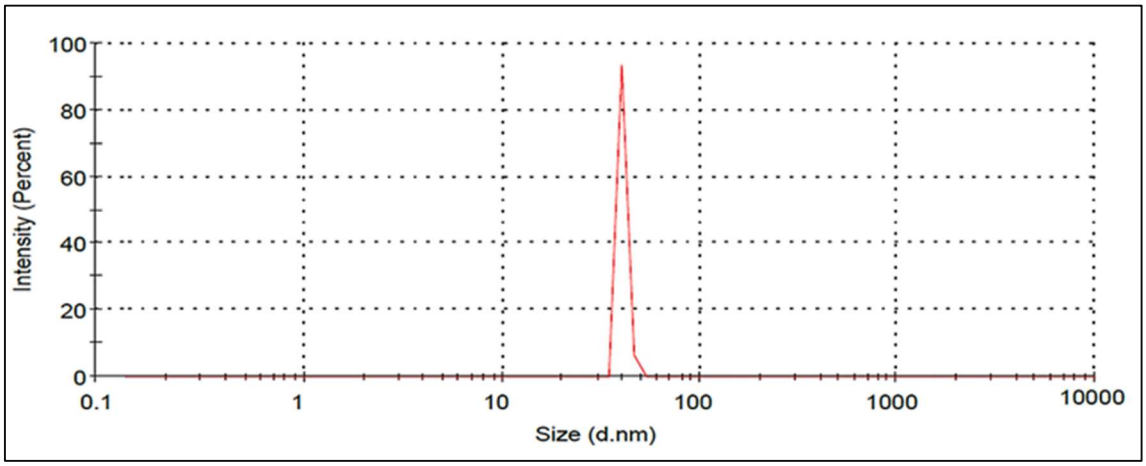

Figure 3.1.9: PNAG NPs particle size recorded by dispersing in PBS (pH 7.4)

In the FTIR spectrum of PNAG NPs (Figure 3.1.4b), distinctive peaks were observed at 3330 cm^{-1}, corresponding to the secondary amine (-NH-) vibrations, 2915 and 2853 cm^{-1} indicative of alkane (-CH-) stretching, 1700 cm^{-1} representing the carbonyl ketone (-C=O) group attached to an acid group, and 1610 cm^{-1} indicating the carbonyl ketone attached

to the amide group. These results collectively contribute to a comprehensive understanding of the structural features and chemical composition of PNAG NPs.

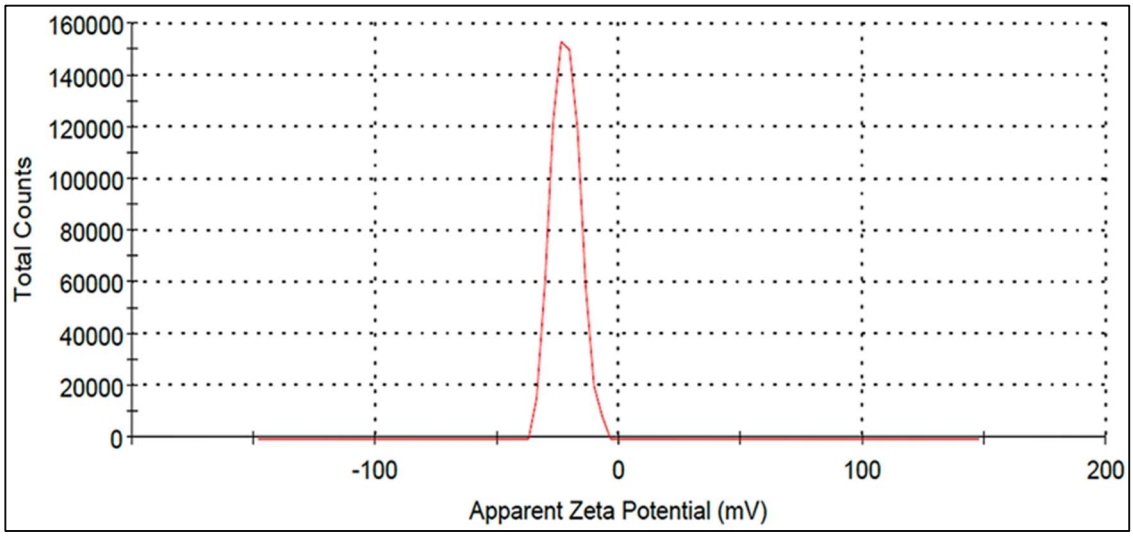

Figure 3.1.10: PNAG NPs zeta potential recorded by dispersing in PBS (pH 7.4)

The formulation of a final product in an amorphous state contributes to enhanced apparent solubility and bioavailability, a crucial factor in pharmaceutical applications, therefore, X-ray diffraction (XRD) patterns, as depicted in Figure 3.1.4c and Figure 3.1.4d were employed to analyse the structural arrangement and crystalline and amorphous state characteristics of both NAG monomer and PNAG NPs. The XRD pattern of the NAG monomer (Figure 3.1.4c) and PNAG NPs (Figure 3.1.4d) reveals that the NAG monomer exhibited a relatively higher degree of crystallinity compared to the PNAG NPs. The crystallinity index (CI) for the NAG monomer was determined to be 81.40%. This high crystallinity ensures structural stability during various processes such as transportation, packaging, or storage [22]. However, it is known that amorphous solids generally exhibit better oral bioavailability [23]. The XRD results indicate that PNAG NPs possess a semi-crystalline nature, suggesting increased amorphousness compared to the NAG monomer, potentially enhancing bioavailability.

The morphology and particle size of PNAG NPs were further explored using high-

resolution transmission electron microscopy (HRTEM), as shown in Figure 3.1.8. TEM micrographs illustrate the formation of co-connected porous network structures with substantial void spaces. The particles exhibit an approximate diameter of ~35 nm with pores ranging from 2 to 3 nm in size (Figure 3.1.8b). The selected area electron diffraction (SAED) pattern (Figure 3.1.8d) confirms the semi-crystalline nature of PNAG NPs, corroborating the XRD findings. Dynamic light scattering (DLS) was employed to ascertain the hydrodynamic diameter of PNAG NPs (Figure 3.1.9), revealing an average size of 40.2 nm, consistent with the HRTEM results (ca. ~35 nm). Additionally, the negative zeta potential value (ξ) of -21.9 mV (Figure 3.1.10) indicates colloidal stability [24], a crucial aspect for applications in various formulations.

3.1.4.2 Biocompatibility and Hemocompatibility of PNAG NPs

In mammals, fibroblast cells, which abundantly populate the skin, play a pivotal role in the development of the extracellular matrix and epithelial-mesenchymal interactions [25]. As such, the cell viability assay of PNAG NPs was conducted using L929 cell line. For biomaterials intended for skin regenerative applications, it is imperative to maintain a low cytotoxic profile, especially on fibroblasts [26]. Increased vasculature is crucial in regenerative medicine, enhancing the supply of blood, nutrients, oxygen, and stem cells at the regenerative site. Human umbilical vein endothelial cells (HUVEC) are frequently employed for *in vitro* angiogenic studies [27]. Thus, toxicity assessments were performed using the MTT assay.

Figure 3.1.11a illustrates the cell viability results for NAG monomer and PNAG NPs on L929 cell line, while Figure 3.1.11b focuses on HUVEC cell line in presence of PNAG NPs. PNAG NPs exhibited excellent cytocompatibility compared to NAG monomers in L929 cell line, with almost 100% cell viability at a concentration of 150 μg mL^{-1} PNAG NP, whereas NAG monomers shows cell viability more than 85%. At the highest tested

concentration (250 µg mL^{-1}), the viability of L929 cell line with NAG monomer and PNAG NPs was 77.01 ±11.16 and 88.92 ±9.43%, respectively (Figure 3.1.11a).

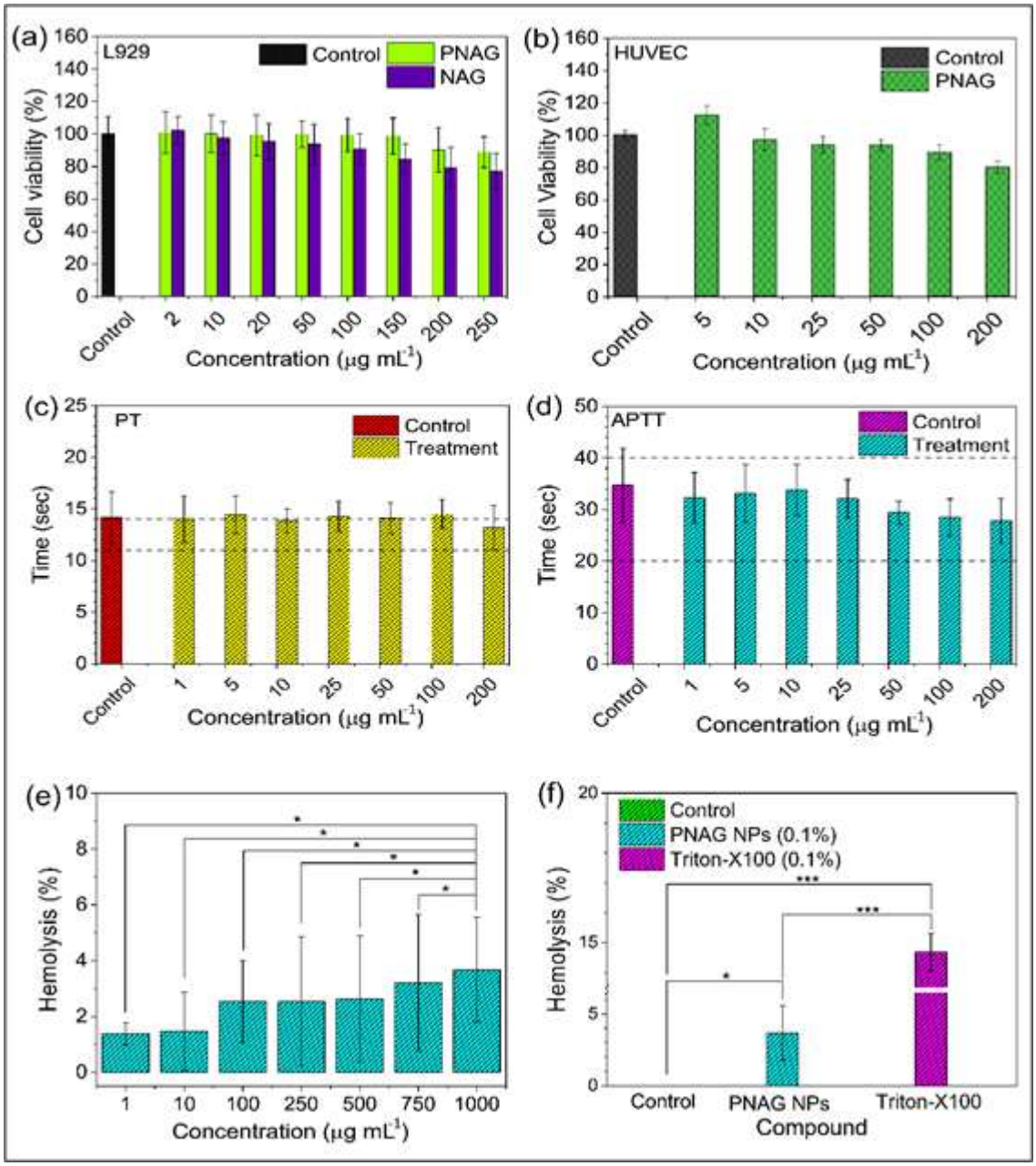

Figure 3.1.11: Cell viability and haemocompatibility of PNAG NPs. (a) Cell viability of the NAG monomer and PNAG NPs in the L929 cell line and (b) PNAG NPs in HUVEC cells. (c) and (d) Effect of different concentrations of PNAG NPs on the blood coagulation cascade in terms of PT (c) and APTT (d). The zones between the black dashed lines represent reference values for PT and APTT. Both the coagulation pathways (PT and APTT) were tested separately. (e) Dose–response curve for the haemolytic activity of PNAG NPs in rat erythrocytes, showing no significant difference (p 4 0.05); (f) haemolysis (%) compared to the control caused by 0.1% dispersion of PNAG NPs and 0.1% Triton X-100 solution in PBS (P>0.05); the outcomes represent the mean ±SD of three separate studies.

In HUVEC cell line (Figure 3.1.11b), treatment with PNAG NPs at a higher concentration (200 µg mL^{-1}) resulted in viability exceeding 80% (80.13 ±3.75), and at lower concentrations down to 5 µg mL^{-1}, it induces cell proliferation up to 115%. This suggests that PNAG NPs can have angiogenic potential at lower concentrations tested in *in ovo* systems.

Furthermore, the assessment of hemocompatibility is crucial to instill confidence in the utilization of biomaterials for therapeutic applications. The systemic circulation of NPs and their potential to induce adverse effects can pose limitations to therapeutic benefits [28, 29]. Therefore, we conducted a thorough evaluation of the hemocompatibility of PNAG NPs using blood coagulation and haemolysis assays. The coagulation of blood involves a complex sequence of protein interactions known as the entire plasma coagulation cascade [30]. Blood samples obtained from Wister rats were collected, and the plasma fraction was separated. Subsequently, these samples were treated with PNAG NPs across a concentration range of 1 to 200 µg mL^{-1}. The assessment focused on activated partial thromboplastin time (APTT) and prothrombin time (PT), as depicted in Figure 3.1.11c and Figure 3.1.11d. The prothrombin time (PT, in seconds) values for PNAG NPs and the control were determined following a 30-minute incubation period. The results revealed values of 14.17 ± 2.48 seconds for the control group (PBS), and for PNAG NPs, the values were 14.01 ± 2.28, 14.43 ± 1.81, 13.86 ± 1.19, 14.29 ± 1.49, 14.11 ± 1.51, 14.48 ± 1.41, and 13.21 ± 2.16 seconds at concentrations of 1, 5, 10, 25, 50, 100, and 200 µg mL^{-1}, respectively. Similarly, the activated partial thromboplastin time (APTT), representing the intrinsic coagulation pathway, was assessed. The APTT values were found to be 34.71 ± 8.10, 32.25 ± 5.50, 33.13 ± 6.25, 33.77 ± 5.58, 32.10 ± 4.23, 29.42 ± 2.48, 28.44 ± 4.10, and 27.81 ± 4.87 seconds at the corresponding concentrations of PNAG (Figure 3.1.11d). The influence on plasma coagulation was negligible at lower

concentrations of PNAG NPs, as depicted in Figure 3.1.11c. However, at higher concentrations, such as 200 μg mL^{-1}, PNAG NPs exhibited a reduction in PT values (13.21 ± 2.16 seconds) compared to the control (14.17 ± 2.48 seconds).

Furthermore, the haemolytic potential of PNAG NPs was systematically assessed in a dose-dependent manner ranging from 1 to 1000 μg mL^{-1}. Various degrees of haemolysis were observed, quantified as 1.38 ± 0.38, 1.46 ± 1.404, 2.53 ± 1.46, 2.55 ± 2.30, 2.62 ± 2.27, 3.20 ± 2.44, and 3.68 ± 1.88% for distinct doses during the 24-hour treatment period, with control values depicted in Figure 3.1.11e. The extent of haemolysis exhibited an increasing trend with escalating doses of PNAG NPs. Nonetheless, even at the highest tested dose, the haemolysis did not exceed 5% compared to the control. Statistical analysis comparing the haemolytic activity of the PNAG NPs treatment group with the negative control (PBS) revealed no statistically significant difference (P>0.05). In contrast, a statistically significant difference was observed when comparing the haemolytic activity of the PNAG NPs treatment group with the positive control (Triton-X-100, 0.1% v/v). Additionally, the comparison between the negative control (PBS) and the positive control (Triton-X-100, 0.1% v/v) demonstrated a statistically significant haemolysis in the positive control group (P<0.05) (Figure 3.1.11f).

In summary, PNAG NPs exhibit a favorable profile of hemocompatibility, with no discernible adverse effects on blood coagulation and blood toxicity. Notably, even at elevated concentrations up to 1000 μg mL^{-1}, PNAG NPs demonstrate suitability for therapeutic applications.

3.1.4.3 PNAG NPs Improve the Wound Closer; *In vitro*

Cellular migration is a pivotal aspect of WH processes [31]. In this study, we systematically investigated the pro-migratory effects of PNAG NPs through an *in vitro* WH assay conducted over a specified period (0 to 48 hours) and at varying concentrations

ranging from 50 to 200 µg mL^{-1} (Figure 3.1.12).

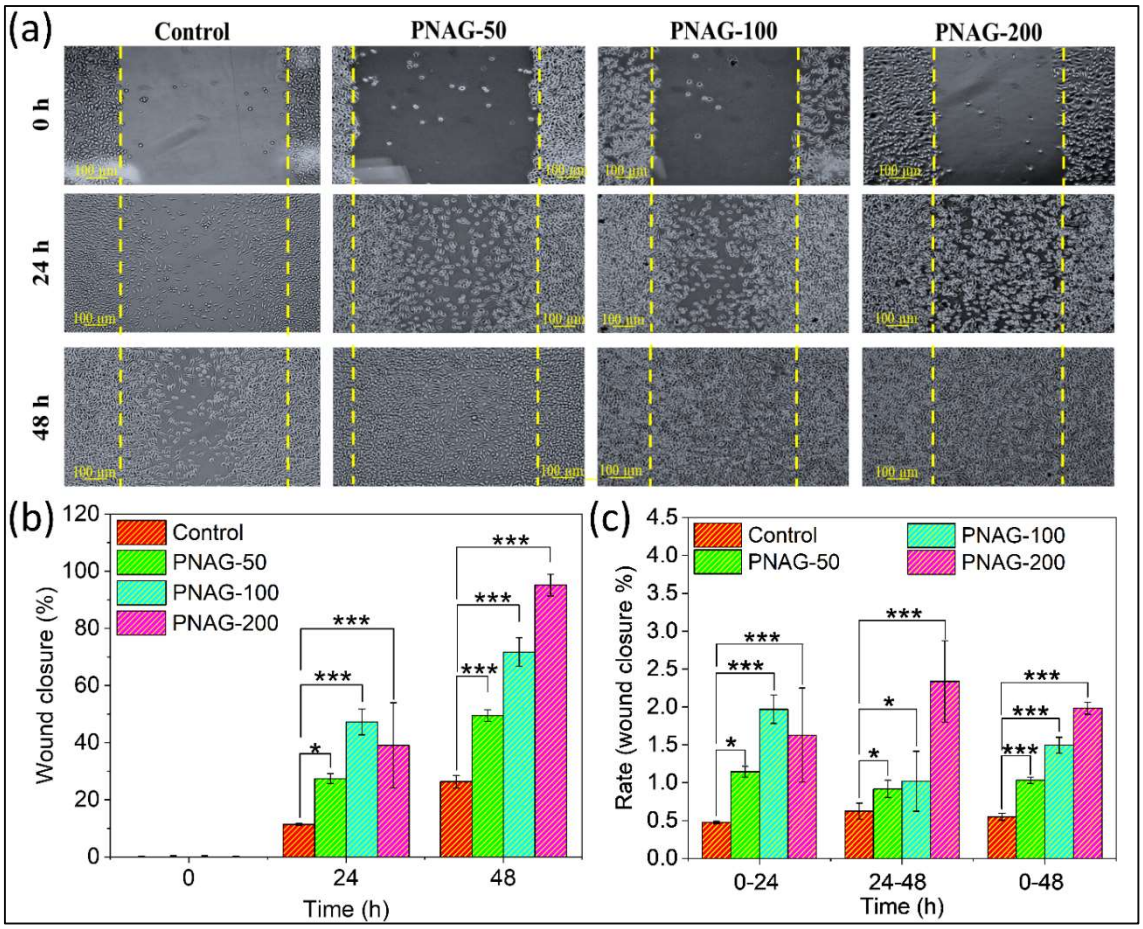

*Figure 3.1.12: In vitro scratch wound healing assay; (a) microscopic images of assay obtained at 0, 24 and 48 h. Images were captured at 10X magnification, and the scale bars indicate 100 µm. Assay was conducted using PNAG NPs in a concentration and time-dependent manner. Treatment: Control (complete cell culture media) and PNAG50, 100 and 200 (PNAG NPs in complete cell culture media at a concentration of 50, 100 and 200 µg mL^{-1}); (b) L929 cells showing in vitro wound closure (%) and (c) rate wound closure (%). Data are given as mean, ±standard deviation (n = 3), (*P ~0.05, ***P<0.001).*

Photographic documentation was employed to analyse the PNAG NPs' influence on fibroblast (L929) cell migration and proliferation, as depicted in Figure 3.1.12a. The results demonstrate the efficient ability of PNAG NPs to induce wound closure in mouse fibroblast cells. After 24 h of scratch wound initiation, control (untreated) cells exhibited a coverage of only 11.38 ±0.42% of the scratched space. In contrast, PNAG NPs-treated cells displayed significantly higher coverage, with values of 27.43 ±1.73%, 47.27 ±4.51%, and 39.08 ±14.90% for PNAG-50, PNAG-100, and PNAG-200, respectively

(Figure 3.1.12b). Notably, during the initial 24 h, the PNAG-200 cell group exhibited a lower coverage compared to PNAG-100; however, in the subsequent 24 h, the WH rate increased, demonstrating a concentration-dependent effect of PNAG NPs (Figure 3.1.12b and Figure 3.1.12c).

In control cells, even after 48 h, only 26.35 ± 2.23% of the scratched space was covered. In contrast, PNAG NPs-treated cells exhibited a significantly higher coverage due to the induction of cell migration and proliferation. After 48 h, cells treated with PNAG-50, PNAG-100, and PNAG-200 displayed coverages of 49.37 ± 2.05%, 71.46 ± 4.72%, and 94.56 ± 2.12%, respectively (Figure 3.1.12b). Remarkably, PNAG-200 treated cells appeared to have nearly complete coverage (94.56 ± 2.12%) of the scratched space, suggesting substantial WH (Figure 3.1.12a).

The experimental findings indicate a substantial enhancement in wound closure efficiency, ranging from 2 to 4 times, upon the administration of PNAG NPs in treated cells compared to untreated counterparts. Additionally, there was an evident escalation in the overall wound closure rate over the 0–48-hour period, as illustrated in Figure 3.1.12c, when contrasted with untreated cells. The temporal dynamics of wound closure within the initial 24 hours revealed an increment in the rate corresponding to lower concentrations of PNAG NPs, whereas higher concentrations exhibited a comparatively lower rate. Following 24 hours of treatment, the rates at lower concentrations were observed to be lower than those at higher concentrations (Figure 3.1.12c). These findings underscore a concentration-dependent influence on wound closure, highlighting the superior WH efficiency associated with lower PNAG NP concentrations.

3.1.4.4 PNAG NPs Exhibit Concentration-Dependent Pro-angiogenic Effects

As indicated by the findings in Figure 3.1.11b, PNAG demonstrates a concentration-dependent promotion of HUVEC cell proliferation, exhibiting 100% viability at 100 µg

mL^{-1} and a slight inhibitory effect at 200 µg mL^{-1}.

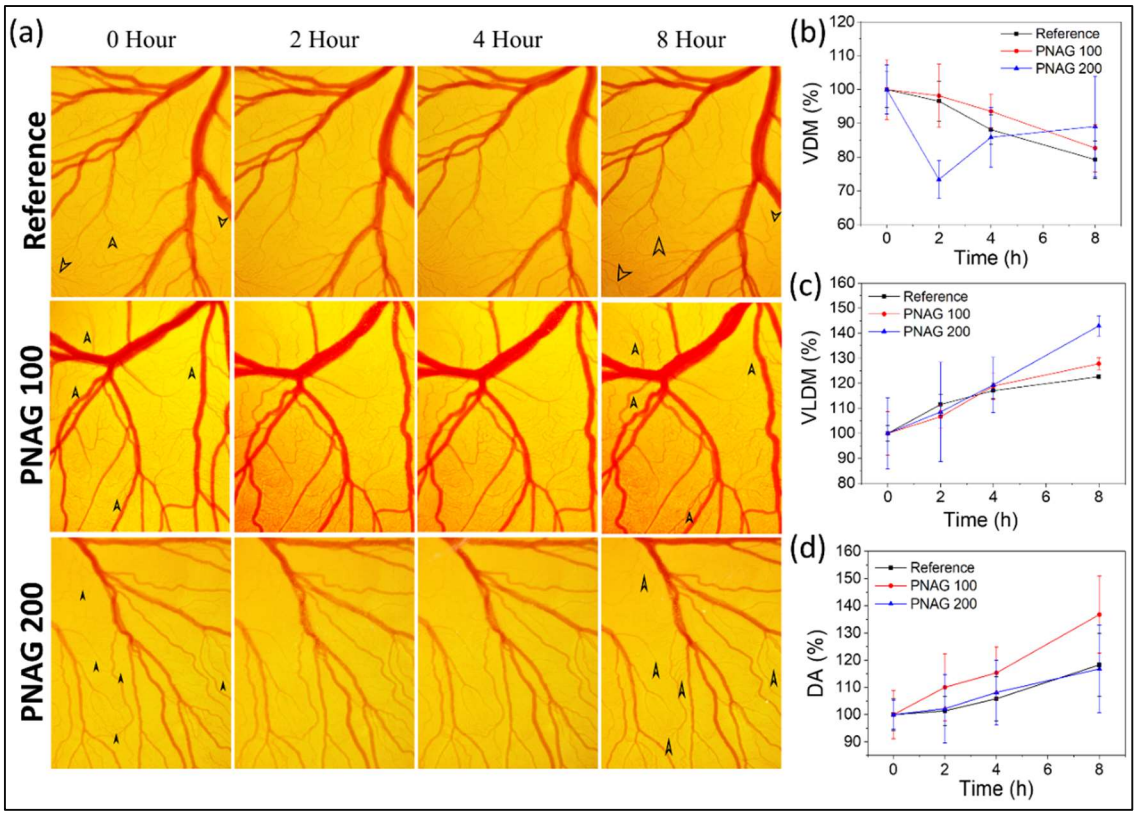

*Figure 3.1.13: Angiogenic assay: Angiogenic effect of PNAG NPs in chicken embryo membrane Assay (CEMA). (a) PNAG NPs stimulate vessels sprouting in the CAM model compared to the reference. Histogram shows the increase in vascular density (b), vascular length density (c) and mean development area (d) as a function of time for a specified vessel structure compared with the reference. The values presented are the mean ±SD of three independent experiments. *p<0.05 is considered significant when compared to normal (n=3)*

To elucidate the angiogenic role of PNAG NPs, an *in vivo* angiogenesis assay, specifically the Chicken Embryo Membrane Angiogenesis (CEMA), was conducted. PNAG NPs exhibited their involvement in vascular sprouting or angiogenesis, as evidenced by the mature and developed blood vasculatures observed after 8 hours of chick embryo incubation with different concentrations (100 and 200 µg mL^{-1}) of PNAG NPs, denoted by black arrows (Figure 3.1.13a).

Moreover, to validate the occurrence of angiogenesis, the analysis involved the determination of increased Vascular Density Measurement (VDM) (refer to Figure 3.1.13b), Vasculature Length Density Measurement (VLDM) (refer to Figure 3.1.13c),

and Developmental Area (DA) (refer to Figure 3.1.13d) utilizing FijiJ software. The VDM results revealed that over the duration from '0' hours to 8 hours, a reduction in vascular density occurred in the reference control, as well as in both the lower (100 µg mL^{-1}) and higher concentration (200 µg mL^{-1}) treated groups of PNAG NPs. Notably, at the higher concentration, an intricate pattern of behaviour was observed during the initial 2 hours. However, by the 8th hour, the vascular density demonstrated an increase in both test groups (refer to Figure 3.1.13b).

The overall Vasculature Length Density Measurement (VLDM) (refer to Figure 3.1.13c) demonstrated an increment, reaching 142.91 ± 4.05% at higher concentrations (200 µg mL^{-1}) and 126.61 ± 0.72% at lower concentrations (100 µg mL^{-1}) of PNAG, in comparison to the reference VLDM value (122.61 ± 0.72%). This trend was consistent across all reference and treated groups. The total length of vessels exhibited an increase over time and with the concentration of PNAG NPs used, despite a reduction in the number density of measured vessels over time. Relative to the reference group, the VLDM enhancements in the treatment group were more pronounced, ranging from 6 ± 4.64% to 27.82 ± 2.40% and 8.56 ± 19.88% to 42.91 ± 4.05% for PNAG NPs at concentrations of 100 µg mL^{-1} and 200 µg mL^{-1}, respectively.

Furthermore, a statistically significant increase in developmental area was observed (refer to Figure 3.1.13d). The developmental area in the reference control is increased by 18.27% within 8 hours while in the treatment group, the results exhibited a concentration-dependent response. The relative increase in developmental area in the treatment groups compared to the reference group was 18.48% and -1.47% at lower concentrations (100 µg mL^{-1}) and higher concentrations (200 µg mL^{-1}) of PNAG NPs, respectively. This observation establishes a correlation between the *in vitro* wound closure as well as cell viability assay. Consequently, these findings suggest that PNAG NPs exhibit angiogenic

properties *in vivo* and may contribute to tissue regeneration at lower concentrations.

3.1.4.5 Development and Quality Assessment of PNAG Nanoformulation

Ointments represent a prevalent semi-solid dosage form for the topical administration of pharmaceuticals, particularly for dermal applications. Typically, medicaments are dispersed within hydrocarbon-oleaginous bases, serving as a crucial component in commercial ointments. In this study, we investigated the use of a hydrocarbon-based oleaginous base (Table 2.2) for formulating PNAG nanoformulation. A 5% glycerine, acting as a humectant, was incorporated into both the PNAG nanoformulation and the formulation base. A qualitative assessment of the formulations was conducted, evaluating physical attributes such as color, appearance, consistency (homogeneity), phase separation, and odor (Table 3.1.1). Both the formulation base and PNAG nanoformulation exhibited smooth, homogeneous, and white or off-white characteristics without agglomeration or grittiness. pH and spreadability were examined at 37 ±2 °C, with the pH values of both formulations falling within the desired range of pH 6.8-7.2, an optimal pH for topical applications to avoid skin sensitivity or irritation [32].

Table 3.1.1: Qualitative characterization of base formulation and PNAG-nanoformulation on the basis of observational parameters

S. No.	Quality Parameter	Required quality	Formulation base	PNAG-nanoformulation
1	Colour	Same as API's colour or white/ off white	Colourless/White	Colourless/White
2	Appearance	Homogenous	Homogenous	Homogenous
3	Consistency/ Homogeneity	Good	Good	Good
4	Phase Separation	No	No	No
5	Odour	Same as API's odour/ Odourless	Odourless	Odourless

Spreadability, which refers to a topical formulation's capacity to distribute evenly over the skin and provide a standard dose of medication to the skin, is a critical factor influencing the effectiveness of topical therapies [33], was evaluated. The spreadability

test revealed that the formulation base and PNAG nanoformulation exhibited spreadabilities of 17.65 ±3.8 and 17.09 ±2.6 gm cm s^{-1}, respectively, indicating comparable spreadability of the prepared PNAG nanoformulation to the formulation base. A higher spreadability coefficient signifies improved distribution and application of the formulation on the skin.

3.1.4.6 PNAG Nano Formulation Assists Dermal Safety

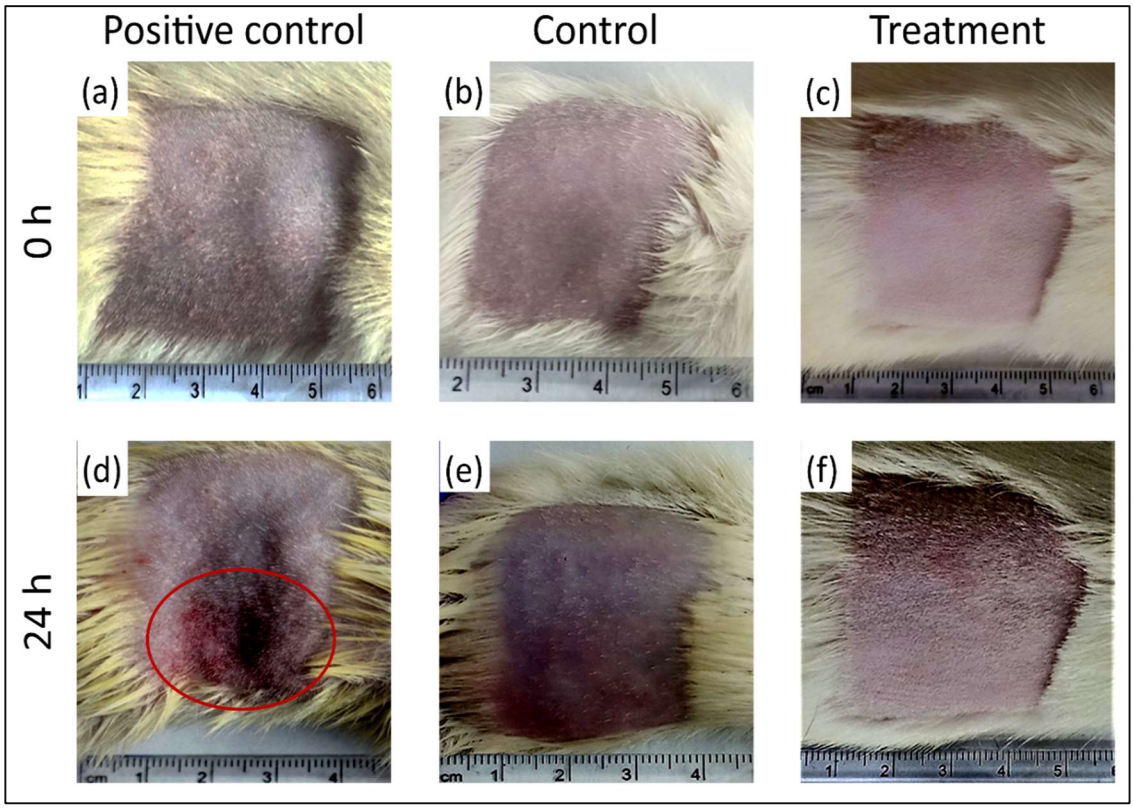

Figure 3.1.14: In vivo skin irritation study in Wistar rats. (A) Results show the dermal irritation study in Wistar rats after dermal application. Images were taken before (0 h) and after (24h) application of samples; (a, d) Positive control (1% formalin soln), (b, e) control (formulation base), (c, f) treatment (PNAG-nanoformulation), respectively. After 24 h of application, control group (e) and treatment group (f) does not show any sign and symptoms of dermal toxicity, i.e., dermal irritancy, while in the positive control group (d) showed significant erythema and oedema at the site of application (in red circle).

Anticipating the potential adverse effects of a biomaterial during the preclinical phase constitutes a valuable strategy to address challenges encountered in subsequent preclinical and clinical stages of drug development. Here, as essential components of preclinical assessment on dermal formulation, dermal irritation and skin sensitization

studies have been conducted, which provide insights into the fundamental characteristics of potential hazards. This information is particularly critical when toxicity data conforming to regulatory guidelines are not readily available.

This study aimed to determine the potential for skin irritation in rats following a single topical treatment with the formulation. The formulations were topically administered to the skin of rats, and alterations in skin color (erythema) and skin swelling (oedema) were systematically investigated. Evaluation of the Primary Dermal Irritancy Index (PDII) was performed using Draize scoring, as outlined in table 2.3. The results of skin irritation, both prior to application (at 0 h) and after application (at 24 h), are illustrated in Figure 3.1.14. Notably, both the treatment and control groups exhibited an absence of erythema and oedema, indicating no discernible signs or symptoms of skin irritation.

In contrast, the positive control group exhibited notable erythema and oedema. These findings indicate that both the formulation base and PNAG nanoformulation were non-irritating and non-sensitizing to the skin, with no significant adverse effects observed after 24 hours of application. The Primary Dermal Irritancy Index (PDII) values were less than 0.25 for both the control and treatment groups, whereas it exceeded 2 in the positive control group. Following the testing period, the animals were monitored for an additional 7 days. All animals, including those in the positive control, control, and treatment groups, displayed good activity and health, without any signs or symptoms of adverse toxicity, abnormal behaviour, or any treatment-related issues noted in the PNAG nanoformulation treated and control groups. Furthermore, a decrease in the overall incidence of irritation and sensitization severity was also observed over time in the animals from the positive treatment group.

3.1.4.7 PNAG Nano Formulation Accelerates Wound Closer; *In vivo*

Table 3.1.2: In vivo wound healing results shown in terms of relative area of wound

Days	Formulation base (Mean ±SD)	PNAG Nanoformulation (Mean ±SD)
0	100.00 ±2.80	100.00 ±0.97
1	104.79 ±2.74	105.08 ±1.62
3	96.45 ±2.38	95.12 ±0.71
5	92.96 ±2.47	90.19 ±3.25
7	83.15 ±4.28	72.63 ±5.44
9	70.91 ±4.81	25.33 ±0.34
11	67.17 ±7.17	4.49 ±0.88
13	55.47 ±3.83	2.93 ±0.43
14	30.74 ±3.11	0.00 ±0.1

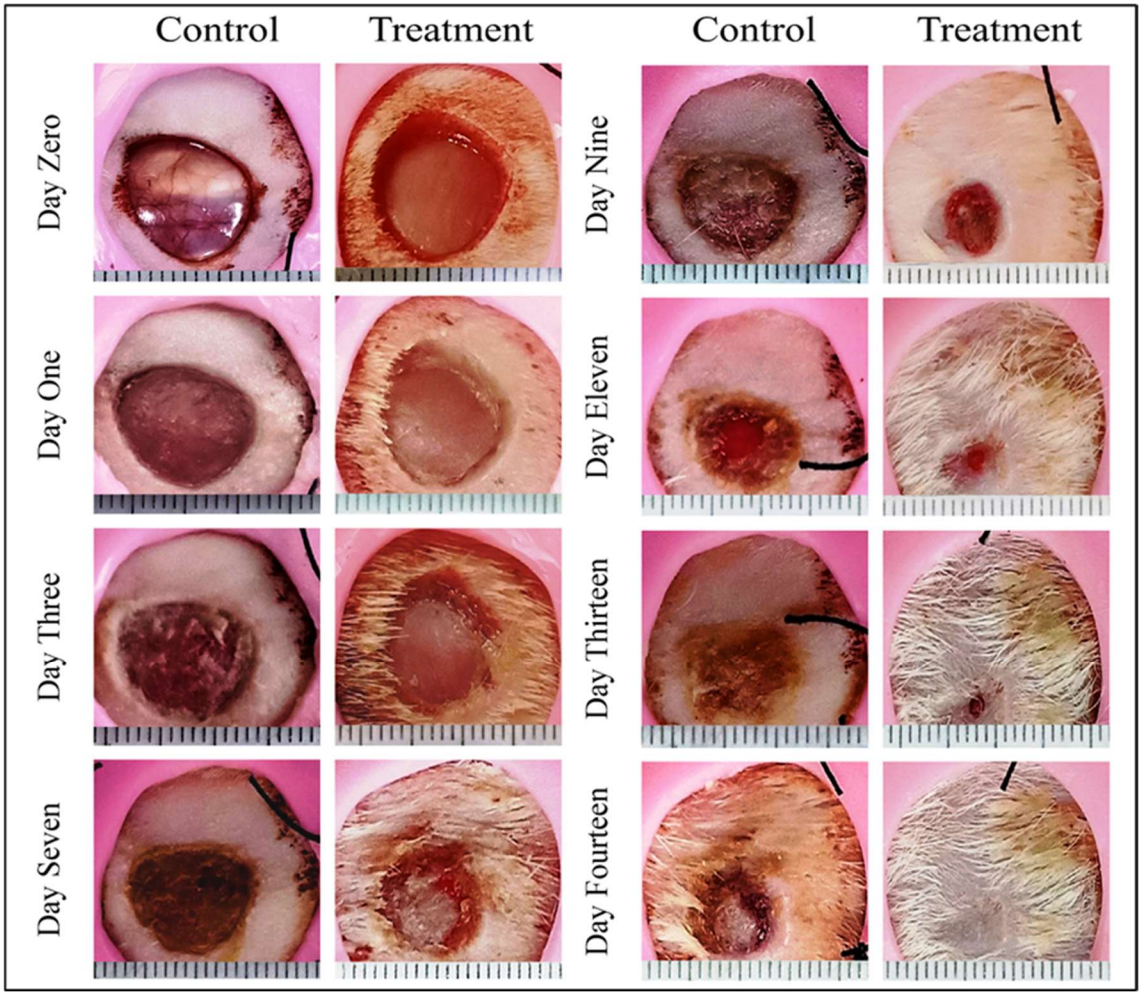

Figure 3.1.15: In vivo wound healing study conducted in Wistar rats. Photo images of wound healing after 0, 1, 3, 7, 9, 11, 13 and 14 days; in Wistar rats treated with formulation base (control) and PNAG nanoformulation (treatment group).

A full-thickness *in vivo* skin wound model using Wistar rats was employed to further

evaluate the potential of the PNAG nanoformulation in light of the previously discussed results. This assessment considered the known properties of PNAG NPs in promoting cell proliferation, migration, and supporting angiogenesis, all of which are beneficial for the process of skin wound repair. The detailed outcomes of this investigation can be found in Table 3.1.2 and are visually represented in Figure 3.1.15 and Figure 3.1.16.

As PNAG NPs exhibit enhanced cell viability, proliferative capacity, and migratory effects *in vitro*, the nanoformulation demonstrated accelerated WH (Figure 3.1.15) and a reduction in wound size compared to the control groups (Figure 3.1.16).

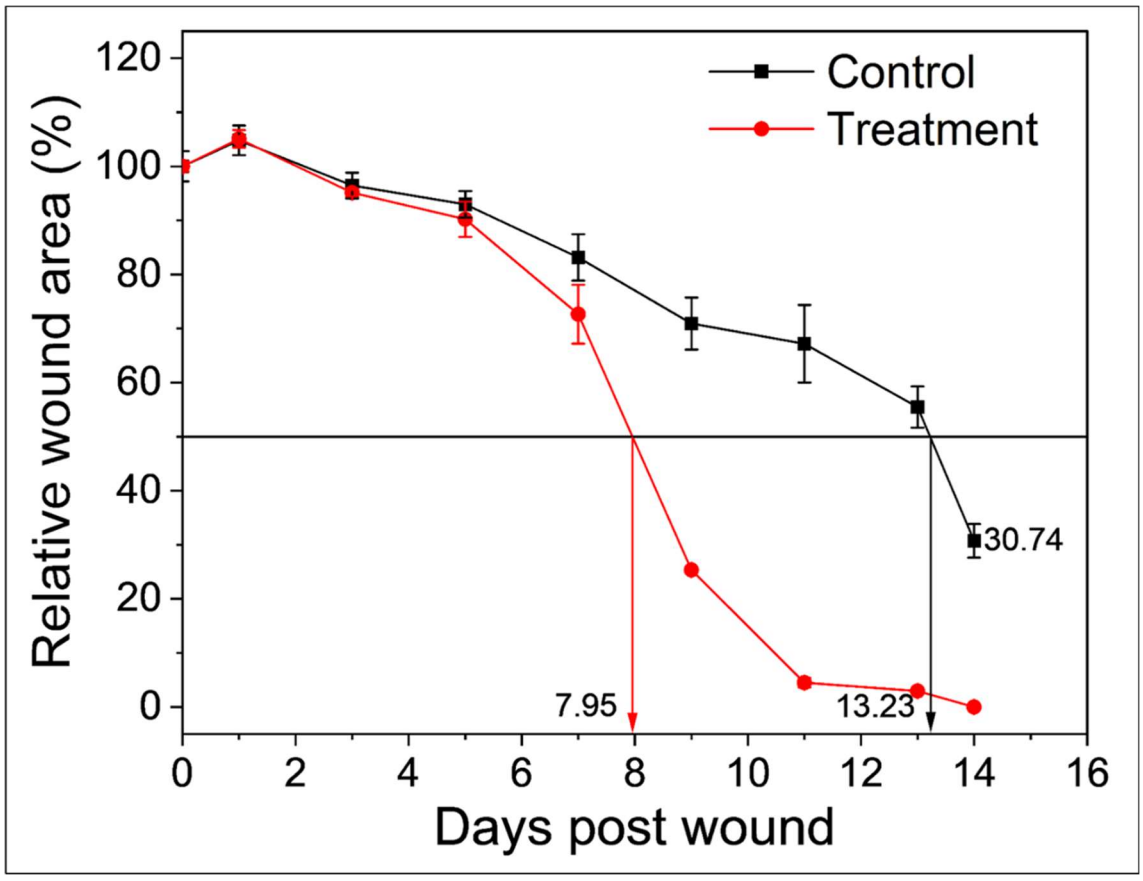

Figure 3.1.16: In vivo wound healing study conducted in Wistar rats. Wound closure profiles of animals treated with formulation base (control group) and PNAG nanoformulation (treatment group) ($p<0.05$). Data are presented as the mean ± standard deviation (n=3).

Figure 3.1.15 illustrates the macroscopic view of the wound at various time points (0, 3, 7, 9, and 14th day) following treatment with PNAG nanoformulation and the formulation base. Additionally, the relative wound area (%) was quantified by measuring the wound

area (Table 3.1.2). The PNAG nanoformulation significantly contributed to substantial wound size reduction in the treatment group compared to the control group, exhibiting clean wound surfaces. Our results indicate that the PNAG nanoformulation was more effective in promoting WH than the formulation base (Figure 3.1.15). On days 0, 1, 3, 5, 7, 9, 11, and 14 post-surgery, the control group (formulation base) exhibited wound areas (%) of 100.00 ± 2.80, 104.79 ± 2.74, 96.45 ± 2.38, 92.96 ± 2.47, 83.15 ± 4.28, 70.91 ± 4.81, 67.17 ± 7.17, 55.47 ± 3.83, and 30.74 ± 3.11, respectively. In contrast, the treatment group (PNAG nanoformulation) displayed wound areas (%) of 100.00 ± 0.97, 105.08 ± 1.62, 95.12 ± 0.71, 90.19 ± 3.25, 72.63 ± 5.44, 25.33 ± 0.34, 4.49 ± 0.88, 2.93 ± 0.43, and 0.00 ± 0.1, respectively. This pronounced healing effect may be attributed to the PNAG nanoformulation creating a conducive environment at the wound site and promoting cell growth. Thus, based on the presented data, we can conclude that the PNAG nanoformulation was highly effective in the treatment of cutaneous wounds.

3.1.4.8 Histological Examinations

Following the wound treatment, an extensive histological analysis was conducted to evaluate various parameters of skin regeneration, including re-epithelialization, granulation tissue formation, and the overall progress of WH, as detailed [34]. Hematoxylin and eosin (H&E) staining were applied to skin sections, facilitating the visualization and confirmation of key aspects of the healing process. This staining method provided insights into the general morphology of skin layers, as illustrated in Figure 3.1.17. The histological evaluation specifically centered on a comparative analysis of the healing status of injured tissue on the 14^{th} day post-wounding, juxtaposed with that of healthy tissue. Notably, the injured tissue samples underwent embedding in paraffin blocks, followed by the preparation of histological slides through H&E staining.

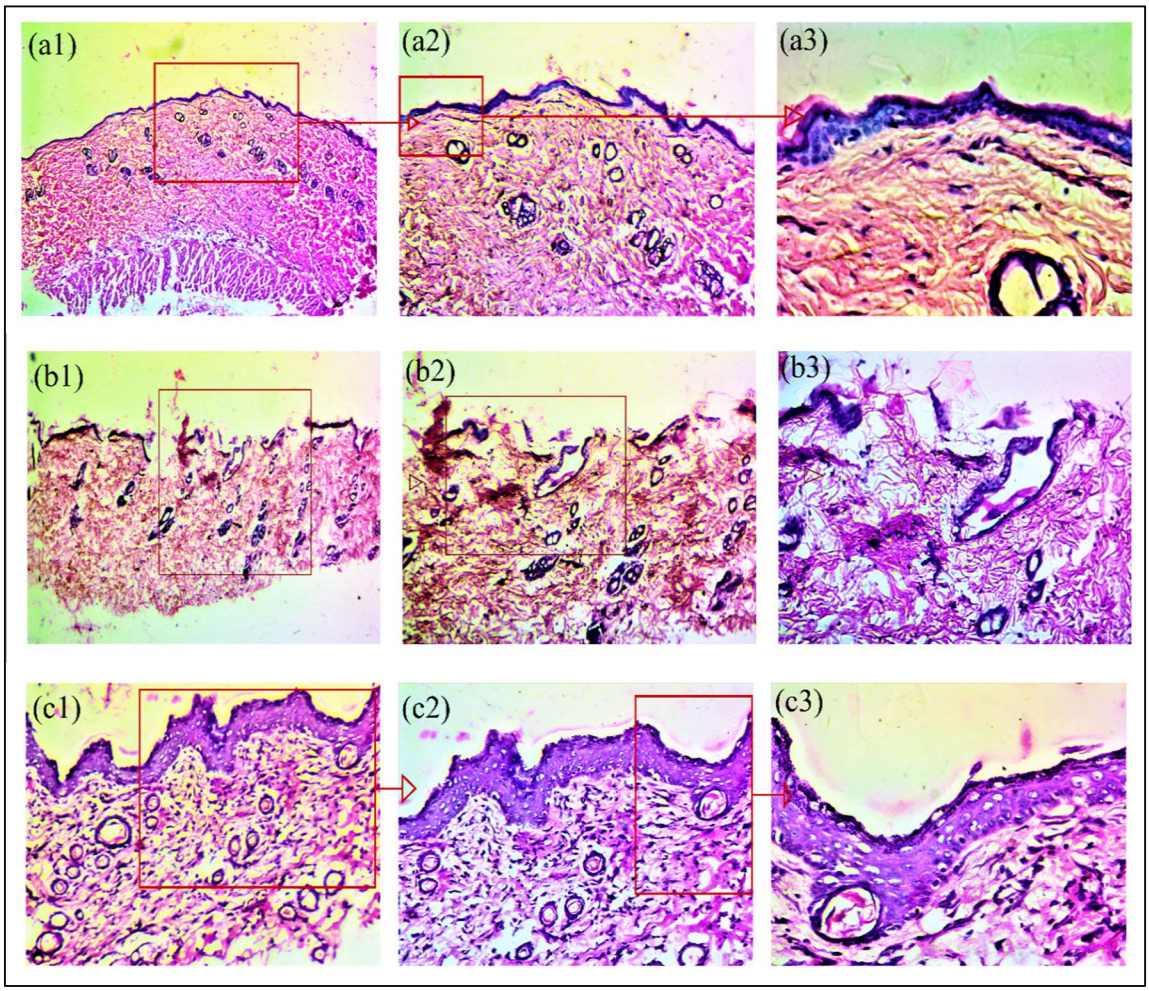

Figure 3.1.17: Histological evaluation on day 14th post-wounding involved a comparison with healthy skin tissue (a), control tissue (base nanoformulation) (b), and PNAG nanoformulation (c). Images at 4x, 10x, and 40x magnifications (denoted by numbers 1, 2, and 3). Healthy skin images (a1, a2 and a3) exhibited well-defined structures such as dead skin, epithelium, collagen fibre-rich dermis, hypodermis, smooth muscle fibre, sweat gland, sebaceous gland, hair follicle, blood vessels, nerve endings, papillary dermis, and reticular dermis rete ridges. Control skin images (b1, b2 and b3) displayed compromised healing, evidenced by broken epithelium, underdeveloped dermis fibres, the absence of hypodermis, undifferentiated reticular dermis, and no rete ridges of the epidermis. While, PNAG nanoformulation-treated skin images (c1, c2 and c3) showcased a well-differentiated epidermis, underdeveloped basal layer, fully differentiated and grown blood vessels, thickened epidermis layers in some areas, fully developed epidermal ridges, mature granuloma, phases of remodelling, and a meshy structure in the papillary dermis and reticular dermis, with the presence of large fibres.

The comparative examination encompassed three distinct types of tissues: healthy skin tissue (a), tissue from the control group animals (Formulation base (b)), and tissue from the treatment group animals (PNAG nanoformulation (c)), as depicted in Figure 3.1.17. This approach allowed for a comprehensive understanding of the histological differences

between the various tissue types, shedding light on the efficacy of the PNAG nanoformulation in promoting WH.

Microscopic images depicting healthy skin tissue [Figure 3.1.17 (a1), (a2), and (a3)] reveals distinct structural components. In (a1), notable features include dead skin, epithelium, collagen fibers in the dermis, hypodermis, and smooth muscle fibers. In (a2), structures such as sweat glands, sebaceous glands, hair follicles, larger blood vessels, nerve endings, papillary dermis, reticular dermis, and rete ridges of the epidermis are observed. Finally, (a3) showcases the basal layer of the epidermis, thick fat collagen fibers, and blood vessels. This detailed analysis provides a comprehensive understanding of the intricate composition of healthy skin tissue at the microscopic level.

Images of tissue from the control group [Figure 3.1.17 (b1), (b2), and (b3)] reveal specific structural characteristics. In (b1), there is evidence of a disrupted or ruptured epithelium. In (b2), observations include underdeveloped dermis fibers, the absence of the hypodermis, lack of rete ridges in the epidermis, an undifferentiated reticular dermis, and papillary dermis. Lastly, (b3) displays features such as an underdeveloped superficial vascular plexus, numerous blood vessels and capillaries, and a spongy epithelium/dermis indicative of edema and inflammation. This detailed analysis provides insights into the histological alterations present in the tissue from the control group.

Images of tissue from the treatment group [Figure 3.1.17 (c1), (c2), and (c3)] reveal distinctive structural features. In (c1), there is a clear and differentiated epidermis, although the basal layer appears underdeveloped. (c2) exhibits fully differentiated and grown large, dilated blood vessels. At some locations, a thick layer of the epidermis is observed, and the epidermis ridges are fully differentiated. Lastly, (c3) displays a fully grown granuloma, indicative of some phases of remodeling. The papillary dermis and reticular dermis exhibit a mushy texture, with the presence of large fibers. This

comprehensive examination provides detailed insights into the histological changes present in the tissue from the treatment group. The outcomes indicate that wounds treated with the PNAG nanoformulation exhibited a heightened presence of fibroblast-like cells and a reduction in mononuclear inflammatory cells, resulting in healed skin structures closely resembling the normal healthy dermis. In contrast, the control group manifested signs of ulceration, including damaged epidermis, edema, and an abundance of mononuclear inflammatory cells, with a notable deep inflammatory infiltration extending through the dermal layer. These observations underscore the beneficial impact of PNAG nanoformulation on tissue repair and inflammatory responses in WH process [35].

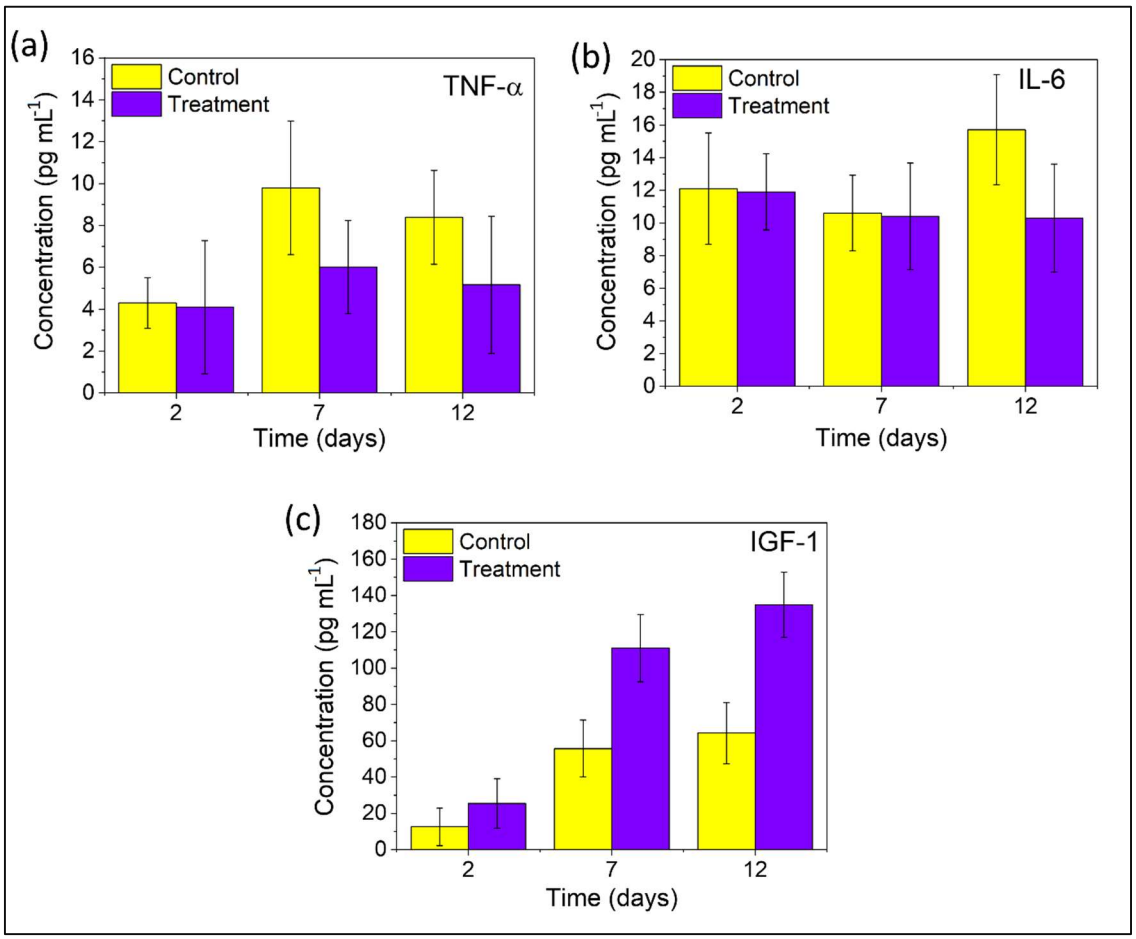

Figure 3.1.18:Immunochemical analysis: (a) TNF-α, (b) IL-6, and (c) IGF. PNAG NPs enhance the concentration and levels of IGF-1 (c) and regulate pro-inflammatory cytokines and chemokines TNF-α (a) and IL-6 (b).

Moreover, histological examination of the PNAG nanoformulation-treated group, as

depicted in H&E images, revealed a morphological profile more closely resembling healthy skin compared to the control group. Within the treatment group, notable features included enhanced neo-vascularization, well-formed dermal and epidermal tissues, sebaceous glands, hair follicles, and a pronounced degree of re-epithelialization, as illustrated in Figure 3.1.17c. These findings underscore the positive impact of the PNAG nanoformulation on tissue regeneration and structural restoration in the context of skin histology.

3.1.4.9 PNAG Nanoformulation Impact on Immune Response, *In vivo* Analysis

The WH trajectory unfolds through distinct phases, encompassing hemostasis, inflammation, proliferation, and remodeling. The pivotal inflammatory phase, occurring second in the sequence, plays a critical role in activating the innate immune system. This activation facilitates the removal of debris and toxins, prevents coagulation, mitigates bacterial infection, and initiates the formation of the fibrin plug. Subsequent to the decline of the inflammatory phase, the proliferative phase commences from day 3 through day 10, marked by the release of growth factors [36]. In order to elucidate the underlying mechanisms governing the WH properties of PNAG NPs, we conducted a comprehensive assessment of the expression of key proteins-TNF-α, IL-6, and IGF-1 known for their exceptional regulatory roles. This examination utilized blood samples obtained from rats at specific intervals, namely the 2nd, 7th, and 12th day, corresponding to distinct stages of the WH process.

Tumor Necrosis Factor-alpha (TNF-α) serves as a regulated chemoattractant at the wound site, exerting control over the activities of keratinocytes, fibroblasts, and vascular endothelial cells [37-39]. Our results indicate TNF-α levels in the control group to be 4.30 ± 1.21, 9.80 ± 3.19, and 8.39 ± 2.24 pg mL^{-1}, while in the treatment group, corresponding levels were 4.10 ± 3.18, 6.02 ± 2.22, and 5.17 ± 3.27 pg mL^{-1} on the 2^{nd}, 7^{th}, and 12^{th} day,

respectively (Figure 3.1.18a). Notably, TNF-α levels in the treatment group, particularly on the 7th and 12th day, coincide with the proliferative phase stimulated by PNAG. During this phase, TNF-α facilitates the production of macrophages, promoting the synthesis of proteoglycan and fibronectin in fibroblasts. Subsequently, these fibroblasts contribute to the formation of the extracellular matrix (ECM) in the injured area, enhancing the overall efficiency of WH [38]. Consequently, the observed lower levels of TNF-α in the treatment group suggest an efficient promotion of WH and closure. Interleukin 6 (IL-6) assumes a pivotal role in cell signaling, lymphocyte regulation, and acute inflammation, crucial for the prompt resolution of WH. It achieves this by overseeing leukocyte infiltration, angiogenesis, and the synthesis and release of collagen by immune cells [40, 41]. In our investigation, the IL-6 levels in the treatment group exhibited relatively minor fluctuations on the 2nd day (11.93 ± 2.34 pg mL^{-1}), 7th day (10.41 ± 3.26 pg mL^{-1}), and 12th day (10.33 ± 3.31 pg mL^{-1}). In contrast, the control group displayed higher values on the 12th day (15.7 ± 3.37 pg mL^{-1}) compared to the 2nd day (10.63 ± 2.32 pg mL^{-1}) and 7th day (12.11 ± 3.41 pg mL^{-1}) (Figure 3.1.18b). This observed elevation in IL-6 expression aligns with the remodelling phase of conventional wound repair. These findings underscore the anti-inflammatory response elicited by PNAG NPs and the nanoformulation, indicating enhanced wound closure efficiency.

Insulin-like growth factor-1 (IGF-1) holds substantial importance in the repair of human tissues and organs due to its anabolic effects [42]. As per Barreca et al., human fibroblasts play a crucial role by producing IGF-1 peptides, which, in a paracrine manner, stimulate keratinocyte growth, underscoring their regulatory function in keratinocyte proliferation, skin growth, and WH [43]. The levels of IGF-1 on the 2nd, 7th, and 12th day were meticulously assessed and demonstrated a significant increase across all groups, as illustrated in Figure 3.1.18c. On the 2nd day, the IGF-1 value for the treatment group was

25.41 ±13.56 ng mL^{-1}, escalating to 134.83 ±17.90 ng mL^{-1} on the 12^{th} day. In comparison, the control group exhibited levels of 12.53 ±10.32 ng mL^{-1} on the 2^{nd} day and 64.22 ± 16.93 ng mL^{-1} on the 12^{th} day post-treatment. Our experimental findings reveal a substantial increase in IGF-1 levels, contributing to the enhancement of keratinocyte migration, thereby expediting wound re-epithelialization and contraction. Consequently, it is evident that during the remodelling phase of WH upon PNAG nanoformulation application, IGF-1 plays a pivotal role in facilitating keratinocyte migration [44].

3.1.5 DISCUSSION

Polymeric NPs (NPs) exert significant influence owing to their capacity to exert essential effects while preserving the integrity of healthy physiological functions. The diminutive size of polymeric NPs enhances cellular uptake and augments interaction points with biological entities. This is attributed to their expansive surface area relative to micro-sized or macro-sized particles, providing heightened accessibility to diverse cellular and intracellular targets. Unlike micro-sized particles, nanosized particles traverse through submucosal layers, with micro-sized particles predominantly localized in the epithelial lining. Consequently, nanosized particles exhibit a superior absorption rate compared to their micro-sized counterparts, underscoring their potential advantages in various biomedical applications [45].

In this investigation, we engineered PNAG NPs possessing noteworthy therapeutic capabilities, biocompatibility, cost-effectiveness, and high yield. The synthesis of PNAG NPs employed the mini-emulsion radical polymerization method [46], ensuring precise control over their size and shape. AIBN, an organic-soluble radical initiator, instigated the generation of free radicals at elevated temperatures (exceeding 75°C), facilitating polymerization within the emulsion droplets. Hexadecane (HD), a long-chain alkane

acting as a co-stabilizer, elevated osmotic pressure and mitigated the coalescence of oil droplets induced by Laplace pressure (Ostwald ripening) [47]. The concentration of co-stabilizer played a crucial role, necessitating a ratio greater than 1:250 of co-stabilizer to monomer [48]. The mechanical stability and porosity of PNAG NPs were achieved through the use of DVB, introducing substantial cross-linking between linear polymer chains. However, an excessive concentration of DVB could lead to the formation of nanoaggregates and nanoclusters. Emulsifiers, represented by surfactants, played a vital role in promoting colloidal stability. SDS was employed as an emulsifier in our synthesis, ensuring uniform PNAG NP size. In the absence of SDS, PNAG NPs exhibited poor physical stability, aggregating and forming larger particles during storage. The micrograph in Figure 3.1.8a reveals a dense nanoporous web-like network arrangement of PNAG NPs, complemented by an approximate diameter of ~35 nm (Figure 3.1.8b), positioning it as a prospective synergistic delivery system. The zeta potential of PNAG NPs (Figure 3.1.10) in an aqueous suspension was measured at -21.9 mV, significantly approaching the deflocculation zone and contributing to the colloidal stability of the PNAG NPs aqueous suspension [49].

Beyond the safety considerations of the bulk material, the physicochemical attributes of NPs (NPs), encompassing monodispersed size distribution, spherical morphology, and surface charge, play a pivotal role in determining their biocompatibility. In this context, both the NAG monomer and PNAG NPs exhibit commendable biocompatibility, demonstrating no apparent toxicity in mouse fibroblasts (L929) cells (Figure 3.1.11a). The assessment of cell viability on HUVEC cells was constrained to PNAG NPs due to their intended utilization in nanoformulation. The outcomes parallel those observed with L929 cells, reinforcing the excellent biocompatibility of PNAG NPs with HUVEC cells, which are known for their heightened sensitivity to biomaterials. Across a concentration

range spanning 5-200 μg mL^{-1}, PNAG NPs exhibited a notable absence of cytotoxic effects, with lower concentrations (5 μg mL^{-1}) even stimulating proliferation in HUVEC cells (Figure 3.1.11b).

The entry of NPs (NPs) into the systemic circulation raises concerns about potential adverse effects that could compromise therapeutic outcomes [28]. Hemocompatibility studies were conducted to ascertain the impact of PNAG NPs on rat red blood cells (RBCs) in comparison to the control (Figure 3.1.11f). The results unequivocally indicate that PNAG NPs do not induce significant hemolysis, affirming their compatibility with the mechanisms governing aquaporins and Na+/K+ ATPase. These mechanisms, crucial for water permeability, diffusion, and erythrocyte osmotic fragility, remain unaltered in the presence of PNAG NPs [50]. Dose-dependent investigations into hemolysis reveal a gradual increase in hemolytic activity with escalating concentrations of PNAG NPs (Figure 3.1.11e).

In the context of blood coagulation, the study encompassed various concentrations of PNAG NPs (up to 200 μg mL^{-1}), demonstrating no discernible impact on prothrombin time (PT) and activated partial thromboplastin time (APTT) levels, despite an increase in PNAG NP concentration (Figure 3.1.11c and Figure 3.1.11d). Notably, PNAG NPs exhibit no adverse effects on the blood coagulation system, cellular components, or hemolysis, even at concentrations considered clinically relevant. These findings collectively affirm the biocompatibility of PNAG NPs with rat RBCs, mitigating concerns regarding potential erythrocyte toxicity.

The process of fibroblast migration and proliferation in the presence of biomaterial plays a pivotal role in the intricate steps of cutaneous WH. The observed effects on proliferation and migration, as demonstrated by PNAG NPs (Figure 3.1.12), substantiate the proposition that these NPs contribute to the re-epithelialization process and the restoration

of skin functionality. The activation of fibroblast proliferation and migration is instrumental in amplifying the rate of granulation tissue formation, culminating in an expedited and efficient WH process [51].

In the context of injury, damage to the blood vasculature results in a deficiency of nutrients and oxygen in the affected tissue. Efficient wound repair necessitates the formation of a robust neo-capillary bed that is subsequently pruned to restore the tissue to its pre-injury state. In our investigation, it was noted that PNAG NPs play a role in promoting vascular sprouting and angiogenesis, expediting the migration of blood vessels toward the wound bed (Figure 3.1.13), particularly at lower concentrations.

The preliminary evidence supporting the non-toxic nature of PNAG NPs is evidenced by their high vitality in L929 and HUVEC cells (Figure 3.1.11a and Figure 3.1.11b) and the absence of significant hemolysis (Figure 3.1.11e and Figure 3.1.11f) in mouse RBCs. The induction of proliferation in HUVEC cells, biocompatibility with fibroblasts, hemocompatibility, and the demonstrated pro-angiogenic behavior collectively validate the safety profile of PNAG NPs, thereby providing a foundational basis for subsequent *in vivo* WH investigations.

The preparation of the PNAG nanoformulation involved the utilization of medical-grade materials. To meet the standards required for preclinical studies, the nanoformulation derived from PNAG NPs underwent a series of quality control assessments aimed at evaluating its suitability for topical applications. Key parameters, including appearance, odor, color, homogeneity, pH, spreadability, and potential dermal irritancy effects, were scrutinized, as these factors play a crucial role in determining patient acceptance of formulations. To ensure compatibility with the skin's pH, the nanoformulation was appropriately adjusted using triethanolamine.

Additional critical parameters include the homogeneity and spreadability of the PNAG

nanoformulation. The uniformity and ease of spread of the nanoformulation are of paramount importance, as any lack of homogeneity or difficulty in spreading may lead to friction from gritty particles, causing secondary injury, pain, prolonged healing times, the necessity for pain management therapy, and an overall increase in therapeutic costs, imposing an economic burden.

Dermal irritancy is a form of hypersensitivity that is assessed by evaluating formulations for erythema and edema after application, employing the Draize scoring scale (Table 2.3). The resulting scores are converted into Primary Dermal Irritancy Index (PDII) values using equation 2.6, where a PDII value of '0' indicates no irritation, 0.5-1.9 indicates modest discomfort, 2 - 4.9 indicates mild irritation, and values above 5 indicate severe irritation. In the evaluation on rat skin against a standard irritant, all animals, excluding the positive control group, exhibited no cutaneous irritation. Conversely, the positive control animals displayed several flares on their skin (Figure 3.1.14d). Throughout a 7-day observation period, the animals displayed no signs of unpleasant toxicity or abnormal behavior, maintaining an active and healthy demeanor. The interconnected and uniformly porous structure of PNAG NPs supports epithelial cell infiltration and proliferation, exudate absorption, and preservation of oxygen supply to the wound tissue. Consequently, the PNAG nanoformulation proves to be a suitable formulation for dermal application.

In Wistar rats, an *in vivo* evaluation of the expeditious WH potential of PNAG NPs was conducted (Figure 3.1.15 and Figure 3.1.16). Notably, on a 10-12 mm diameter excisional wound, we noted a reduction in the levels of exudates secreted during the WH process. This observation finds reinforcement in the histological analysis of 14-day-old wounds, revealing a densely granulated and more efficiently re-epithelialized tissue in the wound center when treated with the PNAG nanoformulation, as opposed to the formulation base (Figure 3.1.17).

On the 2nd, 7th, and 12th days, we systematically investigated the impact of topically administered PNAG nanoformulation on various chemokines, cytokines, and growth factors circulating in the systemic blood of both control and treated animals. Specifically, these analyses were conducted at key time points representing the inflammatory, proliferative, and remodelling phases of WH. The treatment group exhibited lower levels of TNF-α and IL-6 (Figure 3.1.18), indicating a proficient modulation of the anti-inflammatory effects induced by PNAG NPs. Notably, on the 12th day, the treatment group displayed a substantial increase in IGF-1 growth factor levels, suggesting heightened potential for keratinocyte migration in the injured area during the remodelling phase. This upregulation of IGF-1 is associated with increased vasculature, as IGF-1 activates the PI3-Kinase/Akt signaling pathway and concurrently up-regulates the expression of PDGFB, MMPs, and other angiogenic growth factors [52]. Consequently, our findings imply that PNAG NPs play a pivotal role in supporting WH by fostering the formation of new vasculature through angiogenesis, ensuring a nutrient- and oxygen-rich environment in the wound bed [53]. This elucidates the supportive role of PNAG NPs in the intricate process of WH.

3.1.6 CONCLUSIONS

Biocompatibility, hemocompatibility, anti-inflammatory response, and angiogenesis represent pivotal considerations in the context of WH. In this study, we employed the mini emulsion polymerization method to synthesize PNAG NPs, and their successful fabrication was substantiated through comprehensive characterization techniques. Extensive *in vitro* analyses, encompassing assessments of hemocompatibility, cell viability, and *in vitro* WH, provided compelling evidence supporting the appropriateness of PNAG NPs for evaluation in an *in vivo* WH model.

The synthesized PNAG NPs exhibited a moderate expression of WH markers, indicative

of a certain degree of anti-inflammatory potential. Notably, the findings underscored that PNAG NPs contribute to an accelerated healing rate in a full-thickness *in vivo* skin wound model. This study elucidates the ability of PNAG NPs to induce angiogenesis and mitigate inflammation within the microenvironment of skin cells and tissues. The prominent attributes of PNAG NPs, including angiogenesis promotion, facilitation of cell migration and proliferation, and anti-inflammatory activity, collectively advocate their efficacy in promoting WH and overall tissue well-being. These observations suggest the promising potential of PNAG NPs for topical applications in WH and regenerative nanomedicine, obviating the need for external synergistic factors such as drugs, genes, cytokines, growth factors, or cells.

3.1.7 REFERENCES

1. Ijaola, A.O., et al., *Polymeric Biomaterials for Wound Healing Applications: a Comprehensive Review.* Journal of Biomaterials Science, Polymer Edition, 2022. **33**(15): p. 1998-2050. DOI: 10.1080/09205063.2022.2088528.

2. Zhao, X., et al., *Antibacterial Anti-oxidant Electroactive Injectable Hydrogel as Self-Healing Wound Dressing with Hemostasis and Adhesiveness for Cutaneous Wound Healing.* Biomaterials, 2017. **122**: p. 34-47. DOI: 10.1016/j.biomaterials.2017.01.011.

3. Langer, R. and J.P. Vacanti, *Tissue Engineering.* Science, 1993. **260**(5110): p. 920-926. DOI: doi:10.1126/science.8493529.

4. Alberts, B., A. Johnson, and P. Walter, *Molecular Biology of the Cell*. 4 ed. 2002, New York: Garland Science.

5. Krafts, K.P., *Tissue Repair: The Hidden Drama.* Organogenesis, 2010. **6**(4): p. 225-33. DOI: 10.4161/org.6.4.12555.

6. Guo, S. and L.A. Dipietro, *Factors Affecting Wound Healing.* Journal of Dental Research, 2010. **89**(3): p. 219-29. DOI: 10.1177/0022034509359125.

7. Haalboom, M., *Chronic Wounds: Innovations in Diagnostics and Therapeutics.* Current Medicinal Chemistry, 2018. **25**(41): p. 5772-5781. DOI: 10.2174/0929867324666170710120556.

8. Nussbaum, S.R., et al., *An Economic Evaluation of the Impact, Cost, and Medicare Policy Implications of Chronic Nonhealing Wounds.* Value Health, 2018. **21**(1): p. 27-32. DOI: 10.1016/j.jval.2017.07.007.

9. Nosrati, H., et al., *Nanocomposite Scaffolds for Accelerating Chronic Wound Healing by Enhancing Angiogenesis*. Journal of Nanobiotechnology, 2021. **19**(1): p. 1. DOI: 10.1186/s12951-020-00755-7.

10. Mihai, M.M., et al., *Nanocoatings for Chronic Wound Repair-Modulation of Microbial Colonization and Biofilm Formation.* International Journal of Molecular Sciences, 2018. **19**(4). DOI: 10.3390/ijms19041179.

11. Ge, Y. and Q. Wang, *Current Research on Fungi in Chronic Wounds.* Frontiers in Molecular Biosciences, 2022. **9**: p. 1057766. DOI: 10.3389/fmolb.2022.1057766.

12. Deng, X., M. Gould, and M.A. Ali, *A Review of Current Advancements for Wound Healing: Biomaterial Applications and Medical Devices.* Journal of Biomedical Materials Research Part B: Applied Biomaterials, 2022. **110**(11): p. 2542-2573. DOI: 10.1002/jbm.b.35086.

13. Diniz, F.R., et al., *Silver Nanoparticles-Composing Alginate/Gelatine Hydrogel Improves Wound Healing In vivo.* Nanomaterials, 2020. **10**(2). DOI: 10.3390/nano10020390.

14. Paladini, F. and M. Pollini, *Antimicrobial Silver Nanoparticles for Wound Healing Application: Progress and Future Trends.* Materials, 2019. **12**(16). DOI: 10.3390/ma12162540.

15. Sheokand, B., et al., *Natural Polymers Used in the Dressing Materials for Wound Healing: Past, Present and Future.* Journal of Polymer Science, 2023. **n/a**(n/a). DOI: https://doi.org/10.1002/pol.20220734.

16. Henderson, P.W., et al., *Stromal-Derived Factor-1 Delivered via Hydrogel Drug-Delivery Vehicle Accelerates Wound Healing In vivo.* Wound Repair Regen, 2011. **19**(3): p. 420-5. DOI: 10.1111/j.1524-475X.2011.00687.x.

17. Liu, W., et al., *Synthetic Polymeric Antibacterial Hydrogel for Methicillin-Resistant Staphylococcus aureus-Infected Wound Healing: Nanoantimicrobial Self-Assembly, Drug- and Cytokine-Free Strategy.* ACS Nano, 2020. **14**(10): p. 12905-12917. DOI: 10.1021/acsnano.0c03855.

18. Xu, Q., et al., *A Hybrid Injectable Hydrogel from Hyperbranched PEG Macromer as A Stem Cell Delivery and Retention Platform for Diabetic Wound Healing.* Acta Biomaterialia, 2018. **75**: p. 63-74. DOI: 10.1016/j.actbio.2018.05.039.

19. Ranjbar Mohammadi, M., et al., *An Excellent Nanofibrous Matrix Based on Gum Tragacanth-Poly (Ɛ-Caprolactone)-Poly (Vinyl Alcohol) for Application in Diabetic Wound Healing.* Polymer Degradation and Stability, 2020. **174**: p. 109105. DOI: https://doi.org/10.1016/j.polymdegradstab.2020.109105.

20. Fitridge, R. and M. Thompson, *Mechanisms of Vascular Disease: A Reference Book for Vascular Specialists*. 2011, Adelaide (AU): University of Adelaide Press.

21. Kushwaha, A., L. Goswami, and B.S. Kim, *Nanomaterial-Based Therapy for Wound Healing.* Nanomaterials, 2022. **12**(4). DOI: 10.3390/nano12040618.

22. Schittny, A., J. Huwyler, and M. Puchkov, *Mechanisms of Increased Bioavailability Through Amorphous Solid Dispersions: A Review.* Drug Delivery, 2020. **27**(1): p. 110-127. DOI: 10.1080/10717544.2019.1704940.

23. Purohit, H.S., et al., *Investigating the Impact of Drug Crystallinity in Amorphous Tacrolimus Capsules on Pharmacokinetics and Bioequivalence Using Discriminatory In vitro Dissolution Testing and Physiologically Based Pharmacokinetic Modeling and Simulation.* Journal of Pharmaceutical Sciences, 2018. **107**(5): p. 1330-1341. DOI: https://doi.org/10.1016/j.xphs.2017.12.024.

24. Samimi, S., et al., *Lipid-Based Nanoparticles for Drug Delivery Systems*, in *Characterization and Biology of Nanomaterials for Drug Delivery*, S.S. Mohapatra, et al., Editors. 2019, Elsevier. p. 47-76. DOI: https://doi.org/10.1016/B978-0-12-814031-4.00003-9.

25. Wong, T., J.A. McGrath, and H. Navsaria, *The Role of Fibroblasts in Tissue Engineering and Regeneration.* British Journal of Dermatology, 2007. **156**(6): p. 1149-55. DOI: 10.1111/j.1365-2133.2007.07914.x.

26. Lee, J., et al., *In vitro and In vivo Evaluation of a Novel Nitric Oxide-Releasing Ointment for the Treatment of Methicillin-Resistant Staphylococcus Aureus-Infected Wounds.* Journal of Pharmaceutical Investigation, 2020. **50**(5): p. 505-512. DOI: 10.1007/s40005-020-00472-1.

27. Medina-Leyte, D.J., et al., *Use of Human Umbilical Vein Endothelial Cells (HUVEC) as a Model to Study Cardiovascular Disease: A Review.* Applied Sciences, 2020. **10**(3). DOI: 10.3390/app10030938.

28. Chen, L., et al., *Influence of Charge on Hemocompatibility and Immunoreactivity of Polymeric Nanoparticles.* ACS Applied Bio Materials, 2018. **1**(3): p. 756-767. DOI: 10.1021/acsabm.8b00220.

29. Maksimenko, O., et al., *Doxorubicin-Loaded PLGA Nanoparticles for the Chemotherapy of Glioblastoma: Towards the Pharmaceutical Development.* International Journal of Pharmaceutics, 2019. **572**: p. 118733. DOI: https://doi.org/10.1016/j.ijpharm.2019.118733.

30. Laloy, J., et al., *Impact of Silver Nanoparticles on Haemolysis, Platelet Function and Coagulation.* Nanobiomedicine, 2014. **1**: p. 4. DOI: 10.5772/59346.

31. Cometa, S., et al., *Carboxymethyl Cellulose-Based Hydrogel Film Combined with Berberine as an Innovative Tool for Chronic Wound Management.* Carbohydrate Polymers, 2022. **283**: p. 119145. DOI: 10.1016/j.carbpol.2022.119145.

32. Yamamoto, Y., et al., *Pharmaceutical Evaluation of Steroidal Ointments by ATR-IR Chemical Imaging: Distribution of Active and Inactive Pharmaceutical Ingredients.* International Journal of Pharmaceutics, 2012. **426**(1): p. 54-60. DOI: https://doi.org/10.1016/j.ijpharm.2012.01.017.

33. Djiobie Tchienou, G.E., et al., *Multi-Response Optimization in the Formulation of a Topical Cream from Natural Ingredients.* Cosmetics, 2018. **5**(1). DOI: 10.3390/cosmetics5010007.

34. Kang, Y., et al., *Nitric Oxide-Releasing Polymer Incorporated Ointment for Cutaneous Wound Healing.* Journal of Controlled Release, 2015. **220**: p. 624-630. DOI: https://doi.org/10.1016/j.jconrel.2015.08.057.

35. Nurhasni, H., et al., *Nitric Oxide-Releasing Poly(Lactic-Co-Glycolic Acid)-Polyethylenimine Nanoparticles for Prolonged Nitric Oxide Release, Antibacterial Efficacy, and In vivo Wound Healing Activity.* International Journal of Nanomedicine, 2015. **10**: p. 3065-80. DOI: 10.2147/ijn.S82199.

36. Davis, J. and A. McLister, *Chapter One-Introduction to Wound Management*, in *Smart Bandage Technologies*, J. Davis, et al., Editors. 2016, Academic Press. p. 1-35. DOI: https://doi.org/10.1016/B978-0-12-803762-1.00001-1.

37. Mast, B.A. and G.S. Schultz, *Interactions of Cytokines, Growth Factors, and Proteases in Acute and Chronic Wounds.* Wound Repair and Regeneration, 1996. **4**(4): p. 411-420. DOI: https://doi.org/10.1046/j.1524-475X.1996.40404.x.

38. Ritsu, M., et al., *Critical Role of Tumor Necrosis Factor-a in the Early Process of Wound Healing in Skin.* Journal of Dermatology & Dermatologic Surgery, 2017. **21**(1): p. 14-19. DOI: https://doi.org/10.1016/j.jdds.2016.09.001.

39. Mckay, I.A. and I.M. Leigh, *Epidermal Cytokines and their Roles an Cutaneous Wound Healing.* British Journal of Dermatology, 1991. **124**(6): p. 513-518. DOI: https://doi.org/10.1111/j.1365-2133.1991.tb04942.x.

40. Avazi, D.O., et al., *Evaluation of Levels of Interleukin-6, Interleukin-8 and Some Haematologic Parameters of Dogs with Cutaneous Wounds.* Cytokine, 2019. **113**: p. 128-138. DOI: 10.1016/j.cyto.2018.06.024.

41. Lin, Z.-Q., et al., *Essential Involvement of IL-6 in The Skin Wound-Healing Process as Evidenced by Delayed Wound Healing in IL-6-Deficient Mice.* Journal of Leukocyte Biology, 2003. **73**(6): p. 713-721. DOI: https://doi.org/10.1189/jlb.0802397.

42. Grazul-Bilska, A.T., et al., *Wound Healing: The Role of Growth Factors.* Drugs Today, 2003. **39**(10): p. 787-800.

43. Barreca, A., et al., *Effect of Epidermal Growth Factor on Insulin-Like Growth Factor-I (IGF-I) and IGF-Binding Protein Synthesis by Adult Rat Hepatocytes.* Molecular and Cellular Endocrinology, 1992. **84**(1-2): p. 119-26. DOI: 10.1016/0303-7207(92)90078-k.

44. Ando, Y. and P.J. Jensen, *Epidermal Growth Factor and Insulin-Like Growth Factor I Enhance Keratinocyte Migration.* Journal of Investigative Dermatology, 1993. **100**(5): p. 633-9. DOI: 10.1111/1523-1747.ep12472297.

45. Singh, R. and J.W. Lillard, Jr., *Nanoparticle-Based Targeted Drug Delivery.* Experimental and Molecular Pathology, 2009. **86**(3): p. 215-23. DOI: 10.1016/j.yexmp.2008.12.004.

46. Yamala, A.K., et al., *Poly-N-Acryloyl-(L-Phenylalanine Methyl Ester) Hollow Core Nanocapsules Facilitate Sustained Delivery of Immunomodulatory Drugs*

and Exhibit Adjuvant Properties. Nanoscale, 2017. **9**(37): p. 14006-14014. DOI: 10.1039/c7nr03724d.

47. Shen, Y., et al., *The Facile Modification of Polyacrylate Emulsion via Hexadecane to Enhance Controlled-Release Profiles of Coated Urea.* Scientific Reports, 2018. **8**(1): p. 12279. DOI: 10.1038/s41598-018-30585-5.

48. Jeng, J., et al., *Influence of Hexadecane on the Formation of Droplets and Growth of Particles for Methyl Methacrylate Miniemulsion Polymerization.* Journal of Polymer Science Part A: Polymer Chemistry, 2006. **44**(15): p. 4603-4610. DOI: https://doi.org/10.1002/pola.21534.

49. Gupta, P.S., V. Sharma, and K. Pathak, *Melt Sonocrystallized Piroxicam for Oral Delivery: Particle Characterization, Solid State Analysis, and Pharmacokinetics.* Expert Opinion on Drug Delivery, 2013. **10**(1): p. 17-32. DOI: https://doi.org/10.1517/17425247.2013.736961.

50. Greco, I., et al., *Correlation Between Hemolytic Activity, Cytotoxicity and Systemic In vivo Toxicity of Synthetic Antimicrobial Peptides.* Scientific Reports, 2020. **10**(1): p. 13206. DOI: 10.1038/s41598-020-69995-9.

51. Han, G., et al., *Nitric Oxide–Releasing Nanoparticles Accelerate Wound Healing by Promoting Fibroblast Migration and Collagen Deposition.* The American Journal of Pathology, 2012. **180**(4): p. 1465-1473. DOI: https://doi.org/10.1016/j.ajpath.2011.12.013.

52. Lin, S., et al., *IGF-1 Promotes Angiogenesis in Endothelial Cells/Adipose-Derived Stem Cells Co-culture System with Activation of PI3k/Akt Signal Pathway.* Cell Proliferation, 2017. **50**(6). DOI: 10.1111/cpr.12390.

53. DiPietro, L.A., *Angiogenesis and Wound Repair: When Enough is Enough.* Journal of Leukocyte Biology, 2016. **100**(5): p. 979-984. DOI: https://doi.org/10.1189/jlb.4MR0316-102R.

CHAPTER 3: PART II

3.2 Potentiation of Wound Healing Activity of PNAG NPs with Nitric Oxide for Enhanced Skin Regeneration

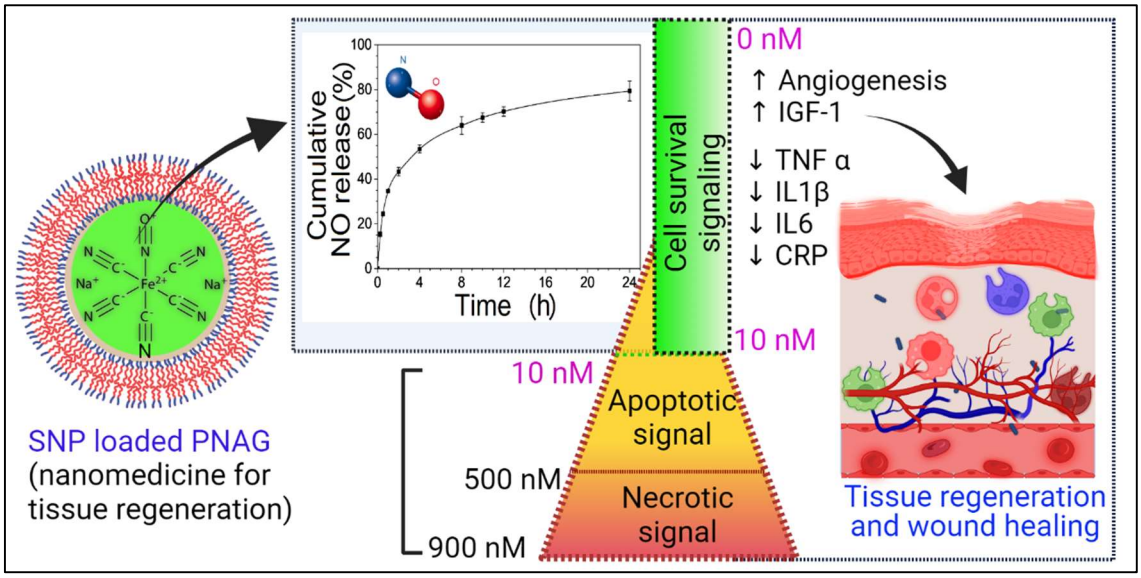

Figure 3.2.1: Prepared PNAG NPs loaded with sodium nitroprusside (SNP a nitric oxide gas-releasing molecule) induce cell migration, proliferation, and angiogenesis, reducing inflammation and accelerating in vivo wound healing.

3.2.1 ABSTRACT

Endogenous gasotransmitter nitric oxide (NO) is a central signalling molecule that modulates WH by maintaining homeostasis, collagen formation, wound contraction, anti-microbial action and accelerating tissue regeneration. Optimum delivery of NO using NPs is clinically challenging; hence, it is drawing significant attention in WH. A novel polymeric nanoplatform loaded with sodium nitroprusside (SP NPs) has been fabricated and used for WH to obtain the sustained release of NO in therapeutic quantities. SP NPs induced excellent proliferation (~300%) of mouse fibroblast (L929) cells have been observed. With the increase in the SP NPs dose, at 200 μg mL^{-1} concentration, a 200% upsurge in proliferation is observed along with enhanced migration, and only 17.09 h is required to fill the 50% gap compared to the control group, which requires 37.85 h.

Further, SP NPs showed an insignificant impact on the coagulation cascade, revealing safer WH treatment when tested in isolated rat RBCs. Additionally, SP NPs have excellent angiogenic activity at 10 μg mL^{-1} dose. Excitingly, formulated SP nanoformulation is non-irritant, non-toxic and does not produce any skin sensitivity reaction on rat's skin. Further, an *in vivo* WH study revealed that within 11 days of treatment with SP nanoformulation, 99.2 ±1.0% of the wound was closed, while for the control group, only 45.5 ±3.8% was repaired. These results directed us that due to sustained NO release, the SP NPs and SP nanoformulation are paramount with enormous clinical potential for the regeneration of wound tissues.

3.2.2 INTRODUCTION

Chronic wounds or hard-to-heal acute wounds negatively impact the quality of life, cause psychological stress and increase the substantial annual financial burden on the healthcare system [1, 2]. According to the epidemiology studies, in India, the prevalence rate is estimated 4.5/1000 population for the chronic wound. Further, trauma-infatuated major injuries are generally associated with diabetic cases. Various indigenous or exogenous factors impair WH mechanisms, followed by the leading severe pathological sequels, significant clinical challenges, and also considered a civilisation disease [3].

Although many works on WH have been reported, however, a deeper understanding of the mechanism and implementation of more effective and cheaper treatment is an essential requirement. Further, WH in embryos and adults has some differences [4] the significant differences observed are associated with the immune/ and inflammatory system and NO production, which is higher in the embryonic system than in the adult wound. It is reported that in WH mechanism, the endogenous gastro transmitter NO plays a crucial role in the regulation of overlapping phases of WH cascaded [5, 6]. Out of the many research available on different materials for therapeutic applications [7]. NO is

mainly associated with the inflammation, antibacterial, collagen production, cell proliferation, re-epithelialisation, and angiogenesis, etc., [8] in adult WH. Therefore, if a controlled dose can apply, NO-induced WH could be one of the most effective therapeutic options. Because NO could have several positive impacts on accelerated WH, its metabolites have been reported in correlation with the healing trajectory, suggesting the propensity for recovery or aggravation [9]. It is reported that mice lacking inducible or endothelial NO synthase exhibit delayed wound repair and poor angiogenesis [10-12]. The impaired WH also results by blocking the knockdown of NOs or by removal of NO occurred by scavengers, and the emergence of chronic wounds is directly linked to turning down the supply of NO at the wounded sites [13, 14]. However, controlled release of NO content is crucial in WH. To increase the level of NO and consequently therapeutic efficiency, exogenous NO donors or stimulators can be used and administered either in the form of direct topical NO donors [15] or indirectly in the form of NO synthase (NOs) stimulator [16] the transfer of the NOs gene, and the systemic delivery of the NOs substrate [15]. Earlier, silica NPs, gold NPs, liposomes, and dendrimers were used for the delivery of NO [17, 18]. Polymeric NPs can be used for the NO delivery due to their advantages such as precise and controlled release of NO as discussed in our previous report [19, 20]. Although, several researches are focused on developing stable and precise delivery of exogenous NO donors to increase NO level at wound site to accelerate the healing process [21], but the current challenges are remained such as initial burst release poor biocompatibility, and low loading capacity [22]. Therefore, developing the NO-releasing delivery system requires extreme care and expertise. Polymeric nanocarrier-based therapeutics of NO proved promising as earlier from our proof of concept and reported that NO delivery through these could enhance WH efficiency [19]. Further, due to fungi static, bacteriostatic, hemostatic, and collagen-forming properties of gelatin,

chitosan and antimicrobial peptides, they have some degree of wound-healing ability [23, 24], however, their therapeutic efficiency are unsatisfactory, and side effects including scar formation and infection, poor adhesive, hydrophobic nature and uncontrolled polymerization were there in long run, arising the essential supply of new therapeutics which will fulfil the current demand [25]. Arison of toxicity with highly potent drugs always reduces their regular use in clinics, but with nanomedicine always a hope that it will reduce the systemic damage and lower toxicity by acting as nanoantidot and deliver compounds in sustained and controlled manner with improved pharmaceutical stability [26, 27].

With the aim to overcome the above challenges and motivated with positive outcomes of nanomedicine, the present work is focused on the synthesis of an advanced biosafe material of poly-N-acryloyl glycine (PNAG) and formulated with a NO donor, sodium nitroprusside (SNP). Acryloyl glycine-based PNAG NPs are biocompatible, proven effective, and safe wound-healing material with angiogenic and biodegradable capabilities and low cytotoxicity effects. Due to the high NO content, quick metabolism and ideal NO release property, SNP can be used as a NO-releasing drug. Clinically, SNP is frequently used to treat hypertensive emergencies and abrupt heart failure and is listed as one of the essential medicines by the WHO [28]. NO-releasing polymeric NPs could allow predictable and regulated NO delivery. The easiest and most efficient method to deliver NO to a cutaneous wound is the topical administration of NO-releasing or NO-generating biomaterials [29]. Therefore, to achieve the optimum NO release, we designed a NO-releasing nanoformulation (SP nanoformulation) from NO-loaded PNAG NPs (SP NPs) and used it for WH. Here, we have scrutinised the toleration of SP NPs against the mouse fibroblast (L929) cell lines and rat RBCs to show the effect on hemolysis. Further, we have studied the extent of proliferation and migration of L929 cells. The skin

sensitisation and irritation of SP nanoformulation have also been studied, and the levels of pro-inflammatory cytokines and chemokines during *in vivo* WH assessment have been investigated. Further, compared to previous NO-releasing therapeutics [30], how these SP NPs and SP nanoformulation are advantageous such as stability, simplicity of application, and prolonged NO release have also been studied. Additionally, the cumulative impact of PNAG NPs and NO co-delivery has not yet been established; therefore, the synergistic effect on full-thickness skin WH has been investigated here.

3.2.3 EXPERIMENTATION

3.2.3.1 Synthesis of NAG monomer, PNAG NPs preparation and SP NPs formation

The method has been described in the experimental section in Chapter 2 (Page No. 62-63, Section 2.2.1).

3.2.3.2 Loading of gas releasing molecule and its quantitative evaluation

Sodium nitroprusside (SNP) was loaded as NO releasing molecule. The methodology for loading of SNP is described in theexperimental section of Chapter 2 (Page No. 72, Section 2.6.1). The loading of SNP was evaluated in terms of entrapment efficiency (%EE) and loading capacity (%LC). Methodology for EE and LC is also described in Experimental section of Chapter 2 (Page No. 72, Section 2.6.2).

3.2.3.3 Characterization of SP NPs

The method has been described in the experimental section in Chapter 2 (Page No. 65-67, Section 2.3).

3.2.3.4 Drug content and drug release determination from SP NPs

The methodology for the assessment of drug content and %CDR have been described in the experimental section of Chapter 2 (Page No.72, Section 2.6.3).

3.2.3.5 Biocompatibility and hemocompatibility of SP NPs

The methodology for assessment of biocompatibility and hemocompatibility have been

described in the experimental section in Chapter 2 (Page No. 67, Section 2.4.1, and Page No. 70-72, Section 2.5, respectively).

3.2.3.6 Cell migration and proliferation assay

The method adopted for assessment of cell proliferation and migration potentioal of SP NPs has been described in the experimental section in Chapter 2 (Page No. 69, Section 2.4.2).

3.2.3.7 Live/ dead assay

The method adopted for assessment of cell's live /dead assay in presence of SP NPs has been described in the experimental section in Chapter 2 (Page No. 70, Section 2.4.3).

3.2.3.8 Angiogenesis assay

The angiogenic potential of SP NPs were evaluated using CAM assay. CAM assay has been described in the experimental section in Chapter 2 (Page No. 77, Section 2.8.1).

3.2.3.9 Development and evaluation of SP nanoformulation

Nanoformulation development and quality evaluation has been described in the experimental section of Chapter 2 (Page. No. 73-76, Section 2.7).

3.2.3.10 *In vivo* skin irritation and skin sensitivity evaluation

In vivo skin irritation and skin sensitivity evaluation of SP nanoformulation has been described in the experimental section of Chapter 2 (Page No. 79, Section 2.8.3).

3.2.3.11 *In vivo* wound healing study

The methodology and protocol for conducting *in vivo* WH study is described in experimental section of Chapter 2 (Page No. 80, Section 2.8.4).

3.2.3.12 Histological analysis

The methodology and protocol for conducting histological evaluation is described in experimental section of Chapter 2 (Page No. 81, Section 2.8.5).

3.2.3.13 Immunomarker evalution during the treatment with SP NPs

containing nanoformulation

The methodology for the evaluation of impact of SP NPs containing nanoformulation on immunomarkers has been described in experimental section of Chapter 2 (Page No. 81, Section 2.8.6).

3.2.3.14 sqRT-PCR

The methodology for sqRT-PCR is described in the experimental section of Chapter 2 (Page No. 82-83, Section 2.8.7).

3.2.3.15 Statistical analysis

Statistical analysis was conducted using Origin 2021 software and data are expressed as mean values (±SD). Statistical test applied on the work are described in the experimental section of Chapter 2 (Page No. 83, Section 2.9).

3.2.4 RESULTS

3.2.4.1 Characterisation of SP NPs

NAG monomer and PNAG NPs were synthesised using a modified procedure (Chapter 2, Section 2.2.1) with 64.21% yield and characterized (Chapter 2, Section 2.3).

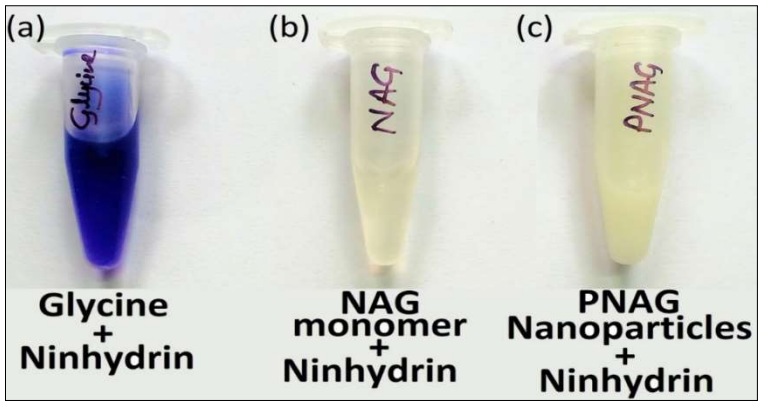

Figure 3.2.2: Ninhydrin test. (a) Glycine amino acid gives vibrant blue/ violet colour, (b and c) NAG monomer and PNAG NPs does not respond to ninhydrin test, showing absence of free amino group (-NH2).

Unlike glycine, which reacts with ninhydrin to give vibrant violet, revealing the lack of a free amino group (Figure 3.2.2). NAG monomer and PNAG NPs were tested for free

amino groups using ninhydrin reagent that showed the lack of free primary amine groups and free from glycine contamination. Further, PNAG NPs formulated with raw SNP, which results in the formation of SP NPs. Functional groups present in synthesised SP NPs and raw SNP were confirmed through FTIR and compared for the loading of SNP in the PNAG NPs.

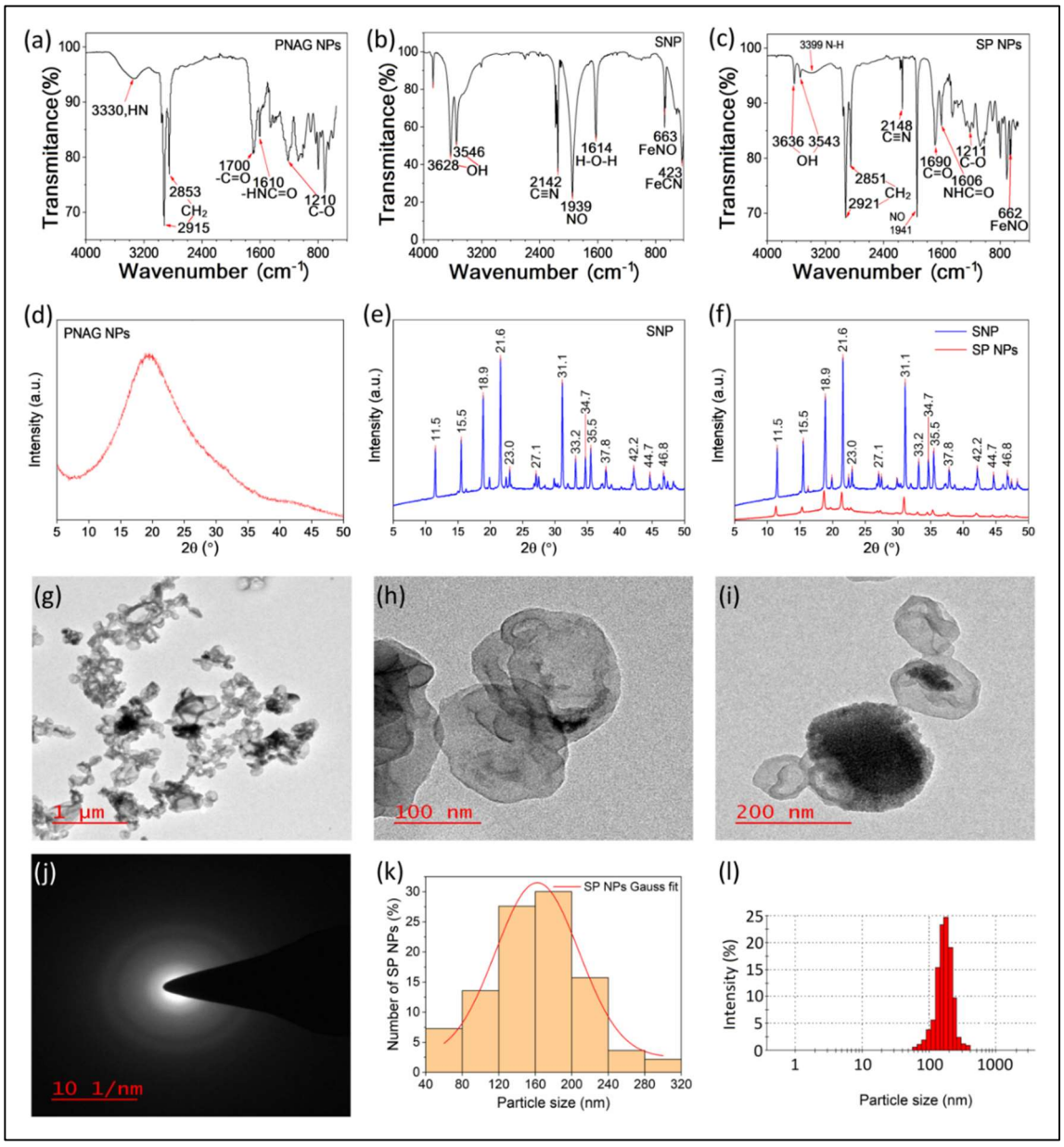

Figure 3.2.3: Characterisation of SP NPs. FTIR spectra of (a) PNAG NPs, (b) Sodium nitroprusside (SNP) and (c) SP NPs. XRD pattern of (d) PNAG NPs, (e) SNP and (f) SP NPs. TEM images of SP NPs (g, h and i), SAED pattern (j), and particle sizes (k) were calculated from TEM images (number of particles > 400) and DLS (l).

FTIR spectrum of SP NPs (Figure 3.2.3c) reveals the characteristic distinct bands for the -C≡N and -NO appeared at 2148 cm^{-1} and 1941 cm^{-1} respectively, which are characteristic of SNP band appeared in FTIR spectra at 2142 cm^{-1} and 1939 cm^{-1} (Figure 3.2.3b) [31, 32]. Further, the bands appeared at 3628-3546 cm^{-1} attributed to the νs, OH of SNP and bands at 3636-3399 cm^{-1} corresponds to the νs -OH and -NH2 of SP-NPs, which confirmed the loading of SNP in PNAG NPs and consequently formation of SP NPs.

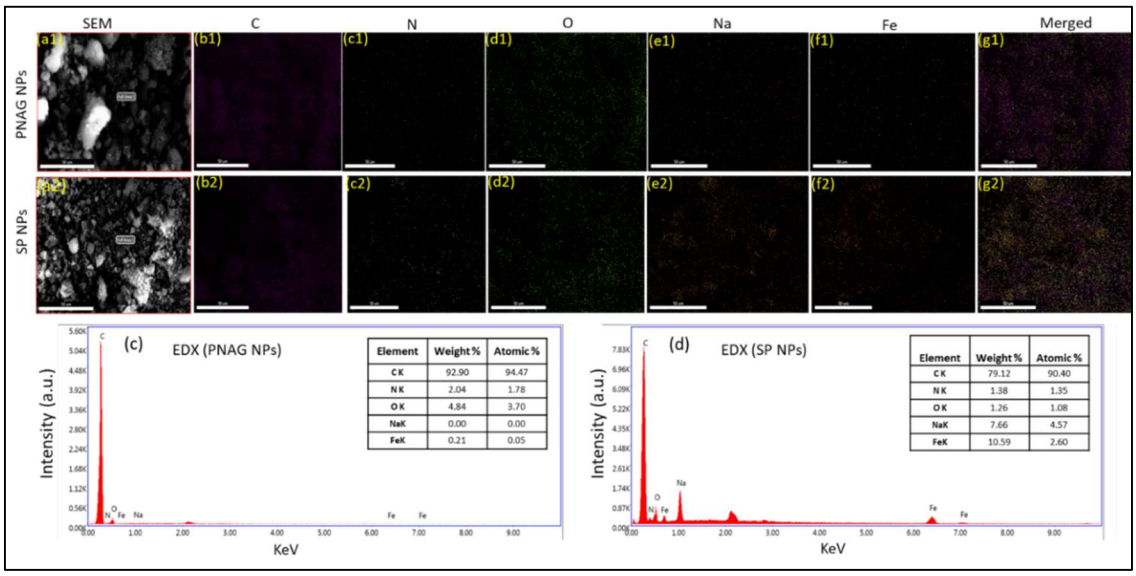

Figure 3.2.4: SEM Images and Elemental Mapping Images of PNAG NPs (a1-g1) and SP NPs (a2-g2). Elements overlay for PNAG NPs, 92.9 (b1), 2.04 (c1), 4.84 (d1), 0.0 (e1), 0.21 (g1), and for SP NPs, 79.12 (b2), 1.38 (c2), 1.26 (d2), 7.66 (e2), and 10.59 (f2) %, respectively of C, N, O, Na and Fe. Mapping of C elements (b1, b2), Mapping of N elements (c1, c2), Mapping of O elements (d1, d2), Mapping of Na elements (e1, e2) and Mapping of Fe element (f1, f2) and merged of all element mapping (g1, g2), in the sample of PNAG NPs and SP NPs, respectively

The XRD pattern of PNAG NPs, SNP and SP NPs are shown in Figure 3.2.3d, e and f. XRD pattern shows, PNAG NPs are semi-crystalline in nature while raw SNP shows fourteen major crystalline peaks at 2θ = 11.5º, 15.5º, 18.9º, 21.6º, 23.0º, 27.1º, 31.1º, 33.2º, 34.7º, 35.5º, 37.8º, 42.2º, 44.7º and 46.8º in addition to a number of peaks that correspond to the high degree of crystallinity. On the other hand, the primary diffraction peaks in SP NPs are also appeared at 2θ = 11.5º, 15.5º, 18.9º, 21.6º, 31.1º, 35.5º, 37.8º and 42.2º confirming that the SNP are loaded in PNAG particles and decreased intensity

of peaks shows the crystallinity of SNP reduced after loading into PNAG NPs. Further, XRD again confirmed the loading of SNP into PNAG NPs with reduced crystallinity of SNP which results in the formation of SP NPs.

Further, the size and surface morphology of the SP NPs have been confirmed through the TEM (Figure 3.2.3g, h and i). TEM micrograph shows co-connected and the balloon-like structure of SNP-loaded NPs, and the dense core seen in particles supports that SNP is loaded inside the particles. Further, diffused ring pattern (Figure 3.2.3j) of the SAED confirmed that SP NPs are semi-crystalline in nature, which supports the results obtained from XRD.

The particle size of SP NPs is found to be in the range of 120-200 nm (Figure 3.2.3k). Particle size results were further confirmed through the DLS (Figure 3.2.3l) and hydrodynamic diameter of particles are found to be ca. 167 nm in diameter. The stability of the SP NPs was confirmed through the Zeta potential (ξ) measurement and the value obtained to be -32.8 mV, confirming the excellent colloidal stability of SP NPs.

Further, the elemental analysis/ mapping was performed using EDS through the scanning and focusing of different area of PNAG NPs and SP NPs and their corresponding peaks are shown (Figure 3.2.4). Both the element, Fe and Na are present in SP NPs while the same are absent in PNAG NPs, this again confirms the loading of SNP into PNAG NPs and successful formation of SP NPs. In the EDS spectrum, the quantity estimation of Fe, Na, O, N and C for PNAG NPs and SP NPs are shown.

SEM images and elemental mapping images of PNAG NPs (Figure 3.2.4a1-g1) and SP NPs (Figure 3.2.4a2-g2) are shown. Elements overlay for PNAG NPs found to be 92.9 (Figure 3.2.4b1), 2.04 (Figure 3.2.4c1), 4.84 (Figure 3.2.4d1), 0.0 (Figure 3.2.4e1), 0.21 (Figure 3.2.4g1), and for SP NPs, 79.12 (Figure 3.2.4b2), 1.38 (Figure 3.2.4c2), 1.26 (Figure 3.2.4d2), 7.66 (Figure 3.2.4e2), and 10.59 (Figure 3.2.4f2) %, respectively of C,

N, O, Na and Fe. Mapping of C element Figure 3.2.4(b1, b2), N elements (c1, c2), O element (d1, d2), Na element (e1, e2) and Fe element (f1, f2) and merged of all element maging (g1, g2) are shown, for the PNAG NPs and SP NPs, respectively. Elemental mapping of PNAG NPs and SP NPs shows the uniform presence of Na and Fe in SP NPs while the same elements are absent in PNAG NPs. Detail of EDX spectra of PNAG NPs and SP NPs values measured in atomic and weight % are listed in Table 3.2.1. Further, elemental mapping results confirmed that the SNP molecules are properly loaded in PNAG NPs.

Table 3.2.1: Elemental mapping results of PNAG NPs and SP NPs showing in weight percentage and atom percentage

		PNAG NPs		SP NPs	
S. No.	**Element Name**	**Weight (%)**	**Atom (%)**	**Weight (%)**	**Atom (%)**
1	**Fe**	0.21	0.05	14.15	3.6
2	**Na**	0	0	7.4	4.57
3	**O**	4.84	3.7	2.92	2.6
4	**N**	2.04	1.78	0.42	0.42
5	**C**	92.9	94.47	75.1	88.81

3.2.4.2 Drug Content loading/entrapment efficiency and NO release efficiency from SP NPs

After accessing the cytotoxicity of PNAG NPs in mouse fibroblast (L929) cells (Figure 3.1.11a, green bars), SNP was loaded in PNAG NPs following the method mentioned in the experimental section (Chapter 2, Page No. 75, Section 2.6.1). The EE (%) of SNP was evaluated through a indirect method by measuring the amount of SNP that remained in the supernatants, and found that almost 40.97 ±1.52% SNP was loaded in PNAG NPs, resulting in nearly 4.86% of absolute NO loadings. SNP is a hydrophilic molecule and is entrapped in hydrophilic PNAG NPs easily. Simultaneously, the LC (%) of PNAG NPs, for SNP is found to be 48.23 ±5.63%. The quantification of NO content was done using UV-Vis spectroscopic method using Griess reagent for the unit weight of SP NPs and found to be 98.29 ±2.79%, which is equivalent to 1.59 ±0.04 µmol mg^{-1} of SP NPs.

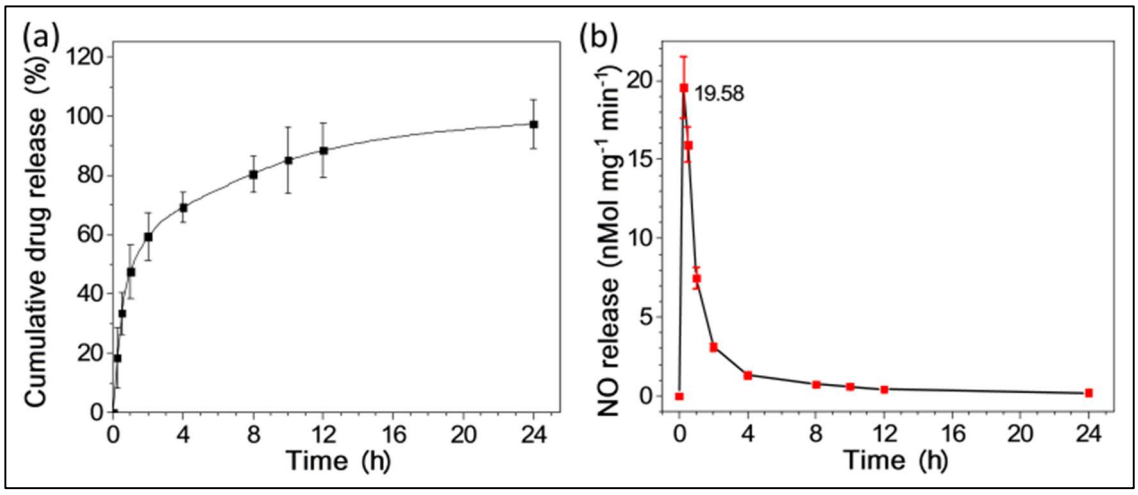

Figure 3.2.5: In vitro NO release profile. (a) Cumulative NO release profile (%, CDR). (b) real-time NO release determination. NO release study was conducted from SP NPs in PBS (pH 7.4) at 37 °C. Data presented as mean ± SD (n=3).

Further, SNP was loaded in PNAG NPs, enabling the release of NO sustainably. The rate of NO release in PBS (pH 7.4) was quantified using the Griess Reagent method. The real-time NO release profile and plot of the total NO release in percentage are shown in Figure 3.2.5. It is observed that NO flux was observed to be 19.58 ±1.97 nmol mg^{-1} min^{-1} within the first 15 min of the start of the release. The total NO content released from the 5 mg of SP NPs within 24 h is 7.95 ±0.23 µmol, or % CDR is 97.37 ±8.19%. Further, it was also observed that SP NPs can able to release NO for more than 24 h at a concentration enough below the toxic level. From % CDR profile, it can be further concluded that 47.64% of NO is released within first one hour from SP NPs. However, after this the rate of NO release continuously decreases with time, as shown in Figure 3.2.5 and follows a sustained release behaviour for 38% of remaining NO for over a 22 h of duration. Further, it can be concluded that due to the hydrophilic nature of PNAG NPs and the SNP's water-soluble characteristics, the release occurred in two stages. In the first stage, NO release was speedy due to the entrapment of SNP on the surface pores of the porous network structure of PNAG NPs. The second stage of NO release is relatively slow because the NO is released from the core part of PNAG NPs.

3.2.4.3 Cytocompatibility/ Cell proliferation and Hemocompatibility of SP NPs

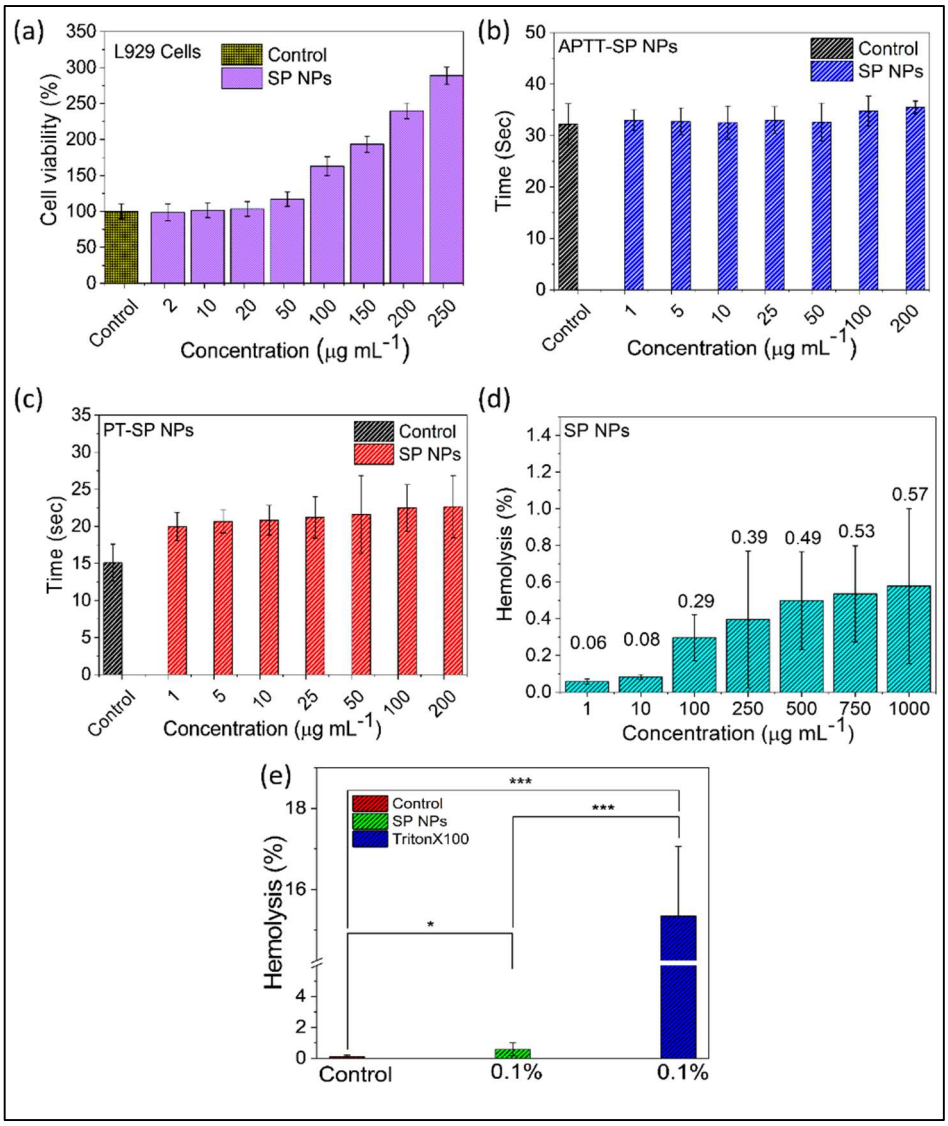

Figure 3.2.6: Cytocompatibility and Hemocompatibility of SP NPs. (a) Cytocompatibility assay: treatment of mouse fibroblast (L929) cells with SP NPs shows proliferation instead of cytotoxicity. (P<0.05). (b) Activated partial thromboplastin time (APTT) and (c) Prothrombin time (PT) tested using different concentrations of SP NPs in the range of 1-200 μg mL^{-1} and compared to the control group (PBS-treated group). (p> 0.05). Data are presented as mean ±SD (n = 3). Hemolytic effect of SP NPs (d and e) on rat RBCs. (d) dose-response curves of hemolysis caused by SP NPs with concentrations ranging from 1 to 1000 μg mL^{-1} (p>0.05). (e) SP NPs show less than 1% hemolytic activity, even at the highest tested concentration (1000 μg mL^{-1}), and hemolysis occurred in rat RBCs by SP NPs dispersion (0.1% w/v in PBS) compared with triton-X100 (0.1% v/v, positive control) against rat erythrocytes. Positive control shows ~15% hemolysis, while SP NPs show ~0.57% (p<0.05).

For any wound dressing material, it is essential to have cellular proliferative and migration stimulatory activity along with hemocompatibility. Therefore, low cytotoxicity

is one of the essential requirements for using SP NP's proliferative capacity in wound dressings.

The cytotoxicity of SP NPs was assessed using an MTT assay using mouse fibroblast cells (L929) line, and PBS was used as the control group. It is noticed that the SP NPs treated L929 cell line survived more than 100% compared to the control, proving that the SP NPs are not cytotoxic. Additionally, with the increase in the concentration of SP NPs, the metabolic activity of cells steadily increased, showing that SP NPs have a strong proliferative potential to promote cell growth. The impact of concentrations of SP NPs on the proliferation of L929 cells is shown in Figure 3.2.6a. After incubation of L929 cells with SP NPs at different concentrations of 2, 10, 20, 50, 100, 200 and 250 μg mL^{-1}, the cell viability (%) relative to control group is found to be very high as 98.5 ±11.7%, 101.4 ±10.0%, 103.4 ±10.2%, 117.0 ±10.0%, 163.0 ±13.0%, 193.3 ±11.1%, 239.8 ±10.8% and 288.7 ±12.0%, respectively, indicating that the SP NPs exhibits a significant growth-promoting effect on the proliferation of mouse fibroblasts are biocompatible.

These studies show that the SP NPs are non-toxic over the concentration range of 2 to 250 μg mL^{-1} and ensure the potential use of SP NPs *in vivo* WH. These results also revealed the cytoprotective effect of NO. Further, the hemocompatibility of SP NPs was evaluated by an *in vitro* blood coagulation test (Figure 3.2.6b and Figure 3.2.6c) and *in vitro* hemolysis that are represented in the consecutive section (Figure 3.2.6d and Figure 3.2.6e).

3.2.4.3.1 Blood coagulation cascade

The anticoagulant properties of the NO-releasing SP NPs to examine potential biological interactions with the blood coagulation cascade have been studied, and the results are shown in Figure 3.2.6b and c. Using APTT and PT, the *in vitro* anticoagulant activity of the synthesised SP NPs has been studied. The APTT values (Figure 3.2.6b) for SP NPs

were found to be 33.0 ±2.1, 32.7 ±2.6, 32.5 ±3.2, 33.0 ±2.6, 32.6 ±3.7, 34.7 ±2.9 and 35.5 ±1.2 sec, for the animals treated at 1, 5, 10, 25, 50, 100 and 200 μg mL^{-1} of SP NPs, respectively. These APTT values marginally deviated from the values reported for the control group of animals (33.0 ±2.1 sec); however, they do not significantly ($P>0.05$) differ from the control group of animals. Similarly, the SP NPs could not substantially alter the PT values ($P>0.05$). Therefore, it can be concluded that the coagulation cascade is unaffected by SP NPs in the concentration range of 1-200 μg mL^{-1}, even though the PT time is risen compared to the control. These results suggest the anticoagulant potential of SP NPs and while the enhanced concentrations have no appreciable impact on the PT.

3.2.4.3.2 Study the hemolysis

Some times death is a consequence of severe blood loss during surgery and accidental trauma. As soon as tissue injury occurs, the wound has to cease bleeding immediately. Consequently, a dressing for WH should have high hemostatic [33] or low hemolytic activity. Due to the ease of separation of erythrocytes, the hemolysis assay is routinely considered in studies of novel xenobiotics and membrane-active biomaterials, and the hemolytic activity test provides a versatile approach for swift initial toxicity evaluation. Therefore, the hemolytic activity of SP NPs (Figure 3.2.6d and e) was measured at different concentrations (0 to 1000 μg mL^{-1}) and compared with the results obtained for PBS. Figure 3.2.6d shows the dose-dependent hemolysis caused by SP NPs. The hemolysis extent is found to be 0.06 ±0.01, 0.08 ±0.01, 0.29 ±0.12, 0.39 ±0.37, 0.49 ±0.26, 0.53 ±0.26 and 0.57 ±0.42 % for the SP NPs concentrations of 1, 10, 100, 250, 500, 750 and 1000 μg mL^{-1}, respectively, after 24 h of treatment. It is observed that hemolysis was below 2% at the maximum investigated dose (Figure 3.2.6d), considered safe [34] for topical use or dermal application and does not cause significant hemolytic activity compared to triton X-100, which causes 15.34 ±1.71% hemolysis at 0.1% v/v

concentration (Figure 3.2.6e). The reason behind high hemolysis caused by adding a detergent like Triton X-100 at 0.1% (v/v) is that it completely hemolyzed the cells, and haemoglobin was released, which consequently showed high hemolysis. It can be noted that positive control shows ~15% hemolysis, while SP NPs show ~0.57% hemolysis which is relatively lower than the hemolysis caused by positive control. Thus it can be concluded that the SP NPs can be used effectively in topical application and safe for WH.

3.2.4.4 *In vitro* wound healing and live dead assay

The ability of SP NPs to promote WH is thoroughly examined by establishing the fibroblasts migration assay to the wounded area. The outcomes of a scratch WH experiment are shown in Figure 3.2.7 (a), (b) and (c) which demonstrates migration of mouse fibroblast (L929) cells in presence and absence of SP NPs. In comparison to untreated cells, SP NPs-treated L929 cells migrate more swiftly in the direction of the scratched area (Figure 3.2.7a).

Observations from the results conclude that even after 24 h of treatment, none of the group's scratch gap was filled, even though fibroblasts were present in each group in disproportionately huge numbers. However, the treatment group received SP NPs at a concentration of 200 µg mL^{-1}, which covered the scratch gap up to 70.0 ±26.4%, compared to the control group (21.2 ±6.2%), indicating a filling rate is approximately 3.3 times higher. As the doses of SP NPs increased, the other treatment groups also exhibited the dose-dependent impact, which showed a reduction in the scratch gap or increased coverage. For SP 50 µg mL^{-1} and SP 100 µg mL^{-1}, scratch gap coverage for treatment groups was found to be 53.4 ±28.9 and 60.2 ±31.4%, respectively. The scratch gap of the control group (PBS) was only significantly narrow after 48 h incubation, and the gap covered (%) at this stage is found to be 71.0 ±16.3%. Although the scratch gap of the untreated group showed wounds not wholly closed and some parts remained to fill, the

scratch gap of all treatment groups at the concentrations of SP NPs of 50, 100, and 200 µg mL^{-1} was found to be filled.

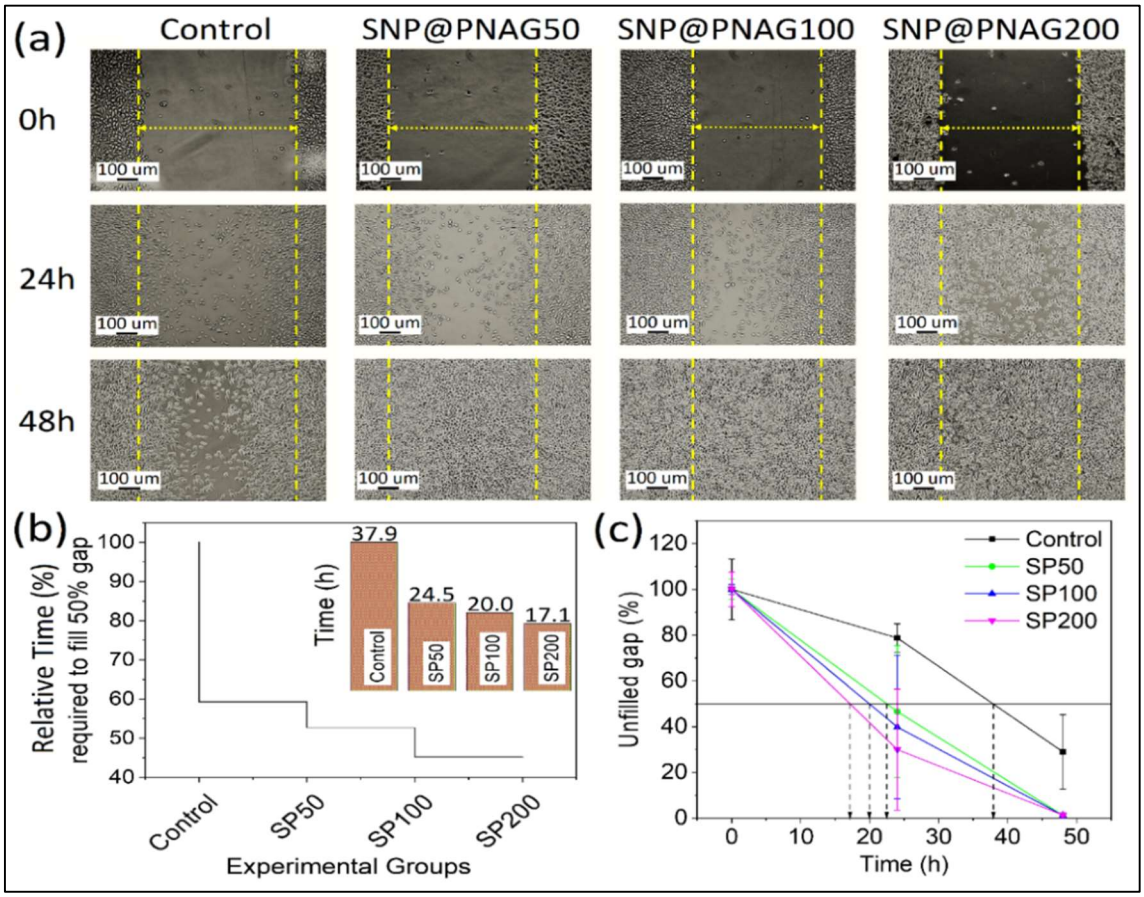

Figure 3.2.7: Scratch wound assay. (a) microscopic images of scratch wounds created in mouse fibroblast (L929) cells after being treated with SP NPs at concentrations of 50 µg mL^{-1}, 100 µg mL^{-1}, and 200 µg mL^{-1} compared to control at 0, 24, and 48 h. Images were acquired at 10x magnification, and the scale bar shows 100µm. (b) The time taken for cells to fill a 50% scratch gap determines how quickly cells migrated towards the scratch gap. (c) Remaining scratch area to be covered by cells.

Further, the live/dead assay of L929 cell line were performed by treating the cells with 50, 100 and 200 µg mL^{-1} of SP NPs and the results were compared with the PNAG NPs (100 µg mL^{-1}). The fluorescent microscopy images after treatment were acquired and the results confirmed (Figure 3.2.8) that the loading of NO in PNAG NPs enhances their viability with negligible sign of toxicity in the form of death of cells has been observed at day-1 (Figure 3.2.8a) for at all treatment concentrations. Whereas, on day -3 (Figure 3.2.8b), the PNAG NPs are showing some extent of apoptotic cell death while at all other

concentrations of SP NPs are safe and does not induces death of L929 cells.

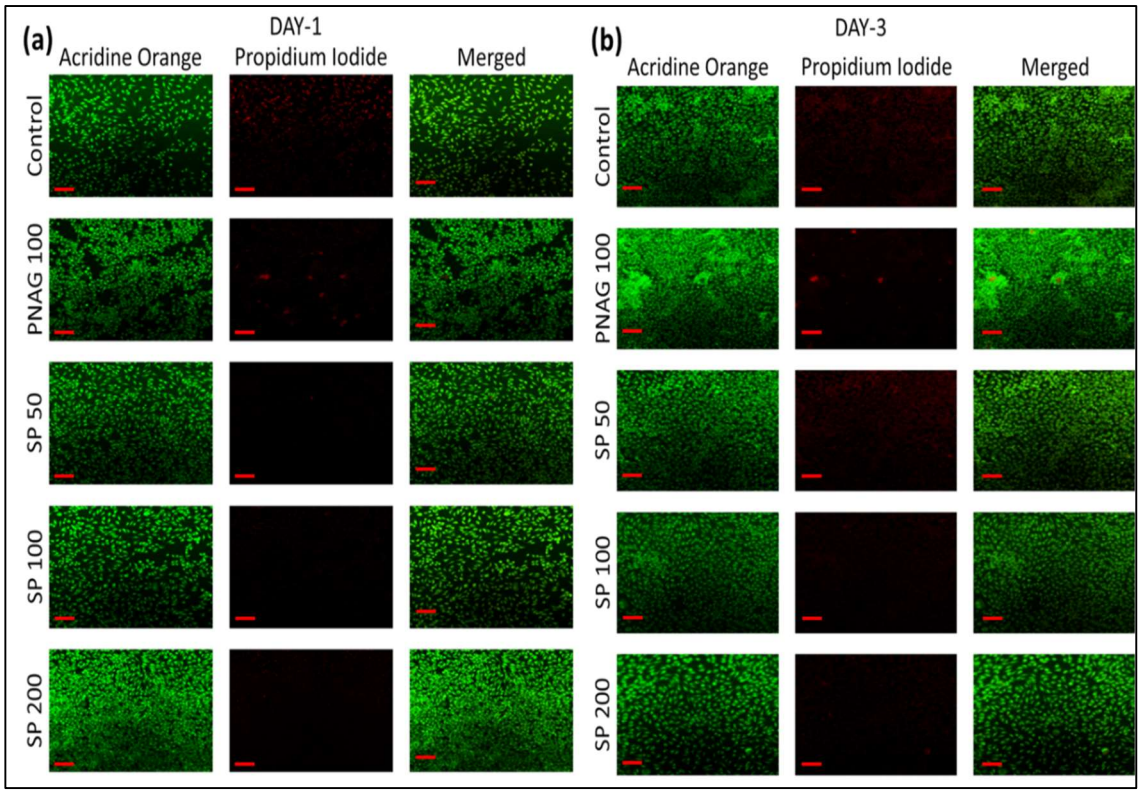

Figure 3.2.8: Live/ dead assay: Figures displaying illustrations of live and dead L929 cells, after day-1 (a) and day-3 (b) of treatment with control, PNAG at 100 µg mL^{-1}, SP NPs at 50, 100, 200 µg mL^{-1}. Scale bar = 100 µm. Cells were stained with Acridine orange and Propidium iodide.

3.2.4.5 Angiogenesis (Chick Embryo Membrane Assay: CEMA)

Angiogenesis can be precisely characterized as the process whereby new blood vessels emerge and proliferate from pre-existing vascular structures [35]. CEMA is one of the most used models for assessing *in vivo* angiogenic activity [36]. Chick embryos are incubated for 8 h with SP NPs (1–100 µg ml^{-1}), and without SP NPs (reference embryo) shows the development of blood vessels. Developed blood vessels are observed at 8^{th} h compared to the initial stage. The CEMA test in Figure 3.2.9 depicts vascular sprouting or angiogenesis under the influence of NO released from SP NPs compared to the reference embryos. Figure 3.2.9b–g shows the quantitative assessment of vascular development in treatment embryos under the

influence of SP NPs, and in untreated reference, embryos were estimated using explant area, vessel length, vessel area, total number of junctions, total number of endpoints, and average vessel length. The quantitative data demonstrates that SP NPs treated at 1 and 10 μg ml^{-1} caused a significant rise in the development of blood vessels, while at 100 μg ml^{-1} exhibits adverse effects (seen as the development of distorted and damaged vasculature: Figure 3.2.9a, SP 100) at higher concentrations. These findings assured that the SP NPs could have both pro-angiogenic or anti-angiogenic effects, depending on the dosage used, both *in vitro* and *in vivo*. Experimental outcomes depict (Figure 3.2.9a) that the chick embryos treated with SP NPs at 1 μg ml^{-1} have exhibited better development than reference embryos. The embryos treated at 10 μg ml^{-1} showed flushing of blood vessels along with dilation for up to 4 h, while at 8 h, the flushing subsided, and vessels tended to reach their normal stage. On the other hand, embryos treated at a higher concentration (100 μg ml^{-1}) show no flushing, but after 2 h, damaged blood vasculature is observed, and after 4 h, the vasculature tends to revert to normalize anatomy and developmental stage; thus it can be concluded that this distortion is temporary and may be occurred due to the access availability of NO (Figure 3.2.9a).

The overall region in which blood vessels are developed is called the explant area (Figure 3.2.9b). Embryos treated at lower concentrations of SP NPs (1 and 10 μg ml^{-1}) show a significant increase (158.6 ±5.5 %, and 173.6 ±7.9%, of initial area, respectively) compared to the reference (135.0 ±8.7 % of the initial area of reference). In contrast, the explant area of embryos treated with 100 μg ml^{-1} significantly decreased from 100% (initial explant area) to 95.7 ±5.7% for the first 2 h. However, after 2 h, it maintained the normal anatomy of the explant area and

continued to follow the trends of the reference embryo, and at the end of 8th h, it was found to be 114.0 ±6.7% of the initial area.

Vessels area is the total surface area of blood vessels occupied in the explants area. The general trend increases vessel area as the blood vessels develop and grow. In our experiment, each group's vessel area (Figure 3.2.9c) increased by 113-173% of the initial vessel area. The vessels area measured at 8 h is found to be 121.8 ±8.7, 166.9 ±5.7, 173.7 ±8.3 and 113.3 ±6.1% of the initial vessels area of reference, and the treatment group treated with SP NPs at a concentration of 1, 10 and 100 μg ml^{-1}, respectively. Herein, the vessel area in embryos treated at high concentrations is lower than in the reference group. Therefore, these findings imply that the SP NPs have both pro-angiogenic and anti-angiogenic effects, depending on the dosage. Further, the junctions are the places from where a new blood capillary starts to arise. In our experiment, we observed an increase in the number of junctions. The highest junction density has been found in embryos treated at 10 μg ml^{-1}, followed by 1 μg ml^{-1}, reference and 100 μg ml^{-1} (Figure 3.2.9d). Total vessel length is the sum of lengths of blood vessels found in the explants area. The total vessel length (Figure 3.2.9e) was measured. At the 8th h of post-treatment, it has been found a significant increased in embryos treated with 10 μg ml^{-1} of SP NPs (187.9 ±9.4). However, a non-significant increase (142.2 ±5.7) is found at 1 μg ml^{-1}, while a significant decrease (123.8 ±6.6) is found at higher concentrations (10 μg ml^{-1}) compared to the reference embryos (140.0 ±8.6). Average vessel length (Figure 3.2.9f) is highest in embryos treated with 10 μg ml^{-1}, followed by a decreasing order at 1 μg ml^{-1}, reference and 100 μg ml^{-1}. From the above results, it is clear that the embryos treated with 10 μg ml^{-1} show the formation of large blood vessels, while the embryos treated with 100 μg ml^{-1} formed smaller blood vessels.

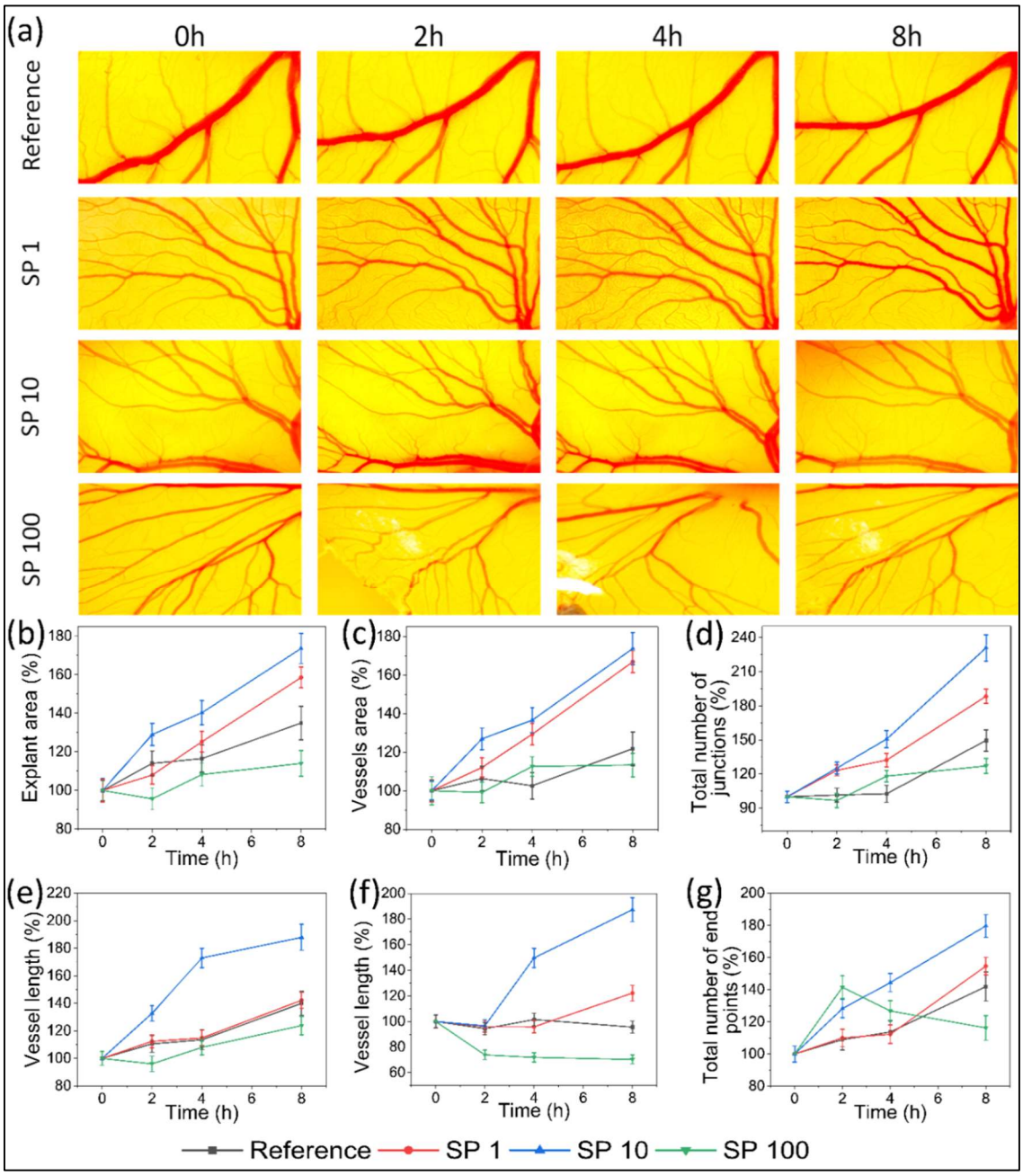

Figure 3.2.9: In vivo Chick Embryo Angiogenesis Assay (CEMA): (a) Determination of the effect of SP NPs on the formation and development of blood vessels in chick embryo model. Corresponding quantitative assessment of vascular development: (b) explant area, (c) vessels area, (d) total number of junctions, (e) vessel length, (f) average vessel length, and (g) total number of endpoints.

Further, the highest blood vessel endpoints (Figure 3.2.9g) are found in embryos treated with 10 µg ml^{-1}, whereas a decreasing order of blood vessel formation is observed once it was treated with 1 µg ml^{-1} SP NPs, reference and 100 µg ml^{-1}. It can be noted that the embryos treated with 100 µg ml^{-1} of SP NPs shows a complex phenomenon within the

first 2 h of treatment. At the same time, the highest endpoints were recorded after 2 h of treatment, such as the endpoints decreased and the blood vessels fused.

3.2.4.6 SP nanoformulation

Table 3.2.2: Qualitative evaluation of SP Nanoformulation

S. No.	Quality Parameter	Required quality	Formulation base	SP-nanoformulation
1	Colour	Same as API's colour or white/ off white	Colourless/ White	Colourless/ White
2	Appearance	Homogenous	Homogenous	Homogenous
3	Consistency/ Homogeneity	Good	Good	Good
4	Phase Separation	No	No	No
5	Odour	Same as API's odour/ Odourless	Odourless	Odourless

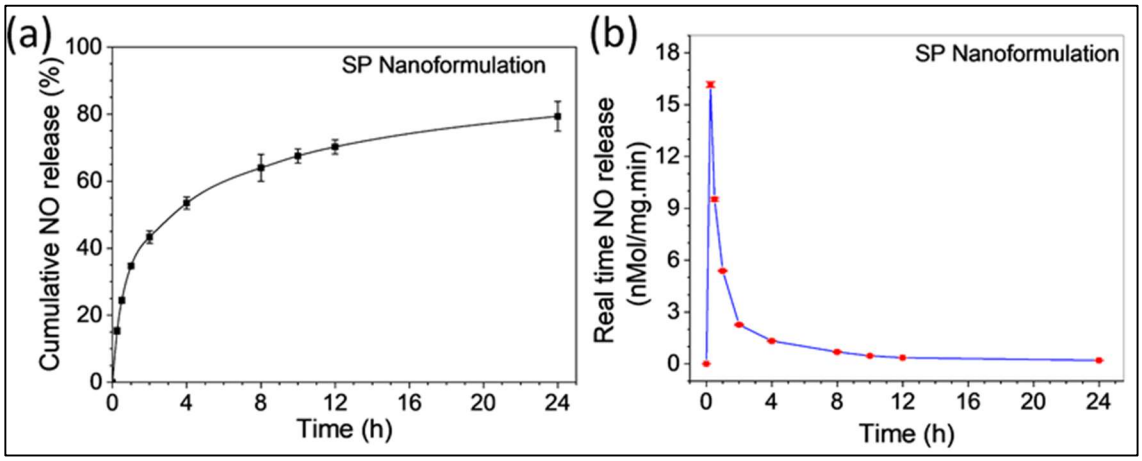

Figure 3.2.10: NO release profile of SP nanoformulation (PBS, pH 6.8, 37°C, n=3). (a) Cumulative drug release, 79.35 ±4.43% NO was released from SP nanoformulation within 24h, showing controlled and sustained release, (b) Real-time NO release profile.

To modify the SP NP's consistency and ease of application on wounds, the SP NPs were mixed with the oleaginous base, one of the most often used ingredients in ointments. The nanoformulation was examined to check for phase homogeneity, aggregation, and discolouration (Table 3.2.2). It seemed uniform, white to off-white, smooth, and devoid of aggregation. Results further indicate that the SP nanoformulation had mean content uniformity of 97.29 ±7.54% for the samples taken from the top, middle, and bottom of each nanoformulation-filled syringe. With a small amount of variance (SD 0.2), the pH

of the nanoformulation found to be at the desired level of pH (pH 7). Assessment of pH variations is crucial because it affects the *in vitro* release of drugs [37] and, ultimately, bioavailability as well as patient acceptance.

3.2.4.7 NO release from nanoformulation

SNP is a hydrophilic drug molecule entrapped easily within hydrophilic PNAG NPs. Oleaginous bases are used to prepare SP NPs nanoformulation to increase the control over NO release. The *in vitro* drug release has been used to determine changes in the formulation's composition and process factors modulating the formulation's *in vitro* and *in vivo* performance (USFDA, 2016). NO-release profile from SP nanoformulation (37 ±2 ℃, pH 6.8) was established, and the outcomes are represented into micromoles per milligram (μmol mg^{-1}) of net SP NPs (Figure 3.2.10).

Experimental setup for estimation of NO release from SP nanoformulation is shown in experimental section of Chapter 2 (Page No. 79, Section 2.7.2 (ii)). In the current investigation, the cumulative NO released per unit area is also measured as a benchmark of the release profile for topical administration rather than cumulative percentage release. SP nanoformulation significantly sustains the release rate of NO in comparison to SP NPs. The observed percent cumulative NO release (%CDR) is 79.35 ±4.43% and 97.37 ±8.19%, for SP nanoformulations and SP NPs, respectively. Within the 1st h of release, around 2.73 ±0.062 μmol, NO was released, which is 43.75 ±0.99% of total CDR (%) (34.72 ±0.79 % of total loaded NO content per 5.0 mg of net SP NPs) from SP nanoformulation, while the rest of ~ 56.25% of CDR (%), was released gradually in subsequent 23 h (Figure 3.2.10a and Figure 3.2.10b). These results suggest that the release of all NO content from the SP nanoformulation requires more than 24 h, as well as maintaining the therapeutic level at the application site. The highest cumulative NO release rate (nmol mg^{-1} min^{-1} cm^{-2}) was found to be 5.146 ±0.050 for the first 15 min,

while the lowest release rate (0.064 ±0.003) was observed in the last 12 h, and while SP nanoformulation releases NO at an average 0.276 ±0.006 nmol mg^{-1} min^{-1} cm^{-2} for 24 h. This shows a controlled and sustained release of NO from the nanoformulation and is beneficial for WH [38].

3.2.4.8 Biological evaluation and effectiveness of treatment

3.2.4.8.1 Skin irritation

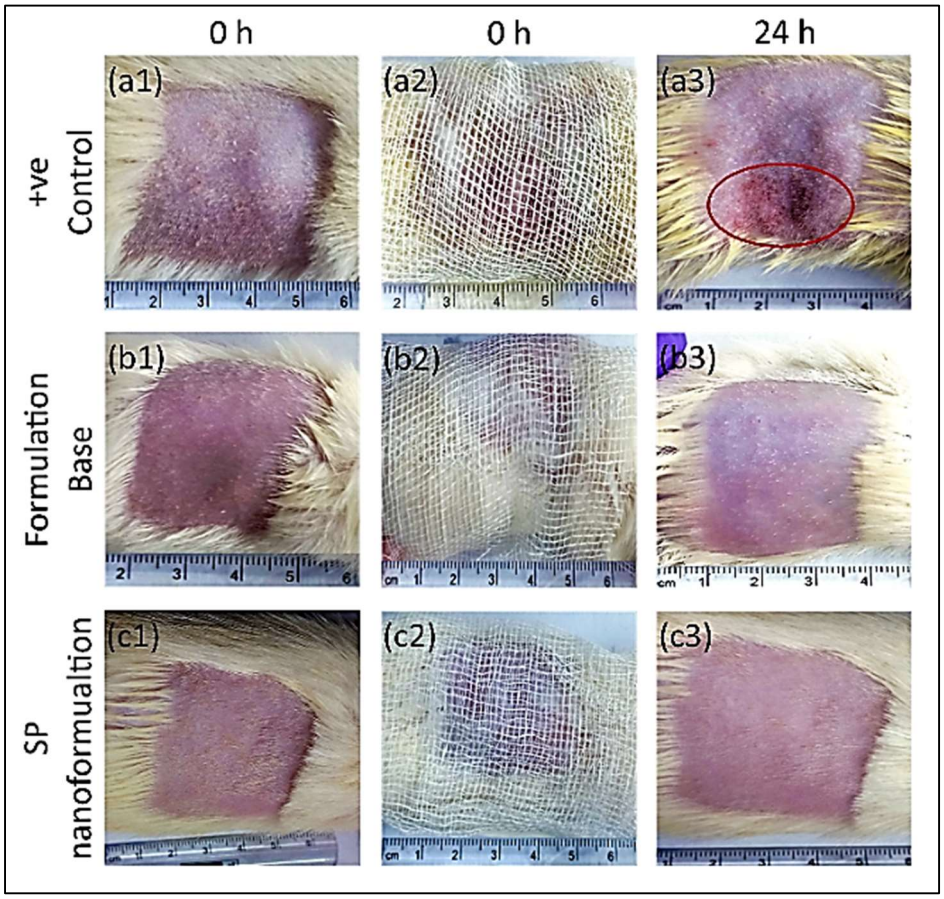

Figure 3.2.11: Photographs of skin irritation study. Positive control (a1) before treatment, (a2) application of 1% formalin solution, (a3) erythema and oedema (shown in red circle) after 24h of application of 1% standard solution, (b1, b2 and b3) control (formulation base) treatment group and (c1, c2 and c3) treatment (SP nanoformulation) group not showing any skin sensitivity and irritation after 24 h of treatment of the respective samples.

Skin irritation study was performed following the method discussed in the experimental section. Here, during the study, no animal deaths occurred during the test. In all cases, skin colour is noted for up to 48 h following the dermal treatment (Figure 3.2.11). Finally,

aside from the positive group, which exhibits substantial irritation at the site of application of 1% formalin solution, no skin reaction is observed in the control and SP nanoformulation-treated animals at the site for 24 h to 72 h after administration. The PDII score for the positive control group was 2.5, whereas the PDII for the control and SP nanoformulation treatment groups was found to be 0.25.

3.2.4.8.2 *In vivo* wound healing

The *in vivo* WH studies were performed after qualifyin the materials and the procedure, as discussed in the experimntal section. Findings revealed that the SP NPs exhibited strong cytocompatibility and enhanced cell proliferation, while SP nanoformulation is non-irritant, both advantageous for the healing of injured skin. Based on the loading capacity of PNAG NPs (48.23 ±5.63%) and maximum NO content found in SP nanoformulation (97.29 ±7.54%) and cumulative NO release from SP nanoformulations has been calculated to be 79.35 ±4.43%.

The dose of SP nanoformulation has been determined and applied to the wounds. SP nanoformulation 100 ±10 mg (contains 5% w/w SP NPs) was applied to the cutaneous wounds since this amount of nanoformulation can be released at a rate of 80.79 ±0.78 nmol min^{-1} for the first 15 min, 47.67 ±0.44 nmol min^{-1} for next 15 min and 45.57 ±52 nmol min^{-1} for next 30 min of nanoformulation treatment. These effective dosages cause nitrosative signalling (for nitrosative signalling, NO concentration must be more than 10 nmol) in the microbes, if any, present at the surface of a wound. After 2 h, these doses can maintain the concentration of NO release enough below to 10 nmol for subsequent 22 h of application, which helps in effective WH [39].

However, the impact of SP nanoformulation on Wistar rats' WH was investigated (Figure 3.2.12). It is noted that under normal circumstances, wounds tend to heal with time, and it is a normal phenomenon of body homeostasis.

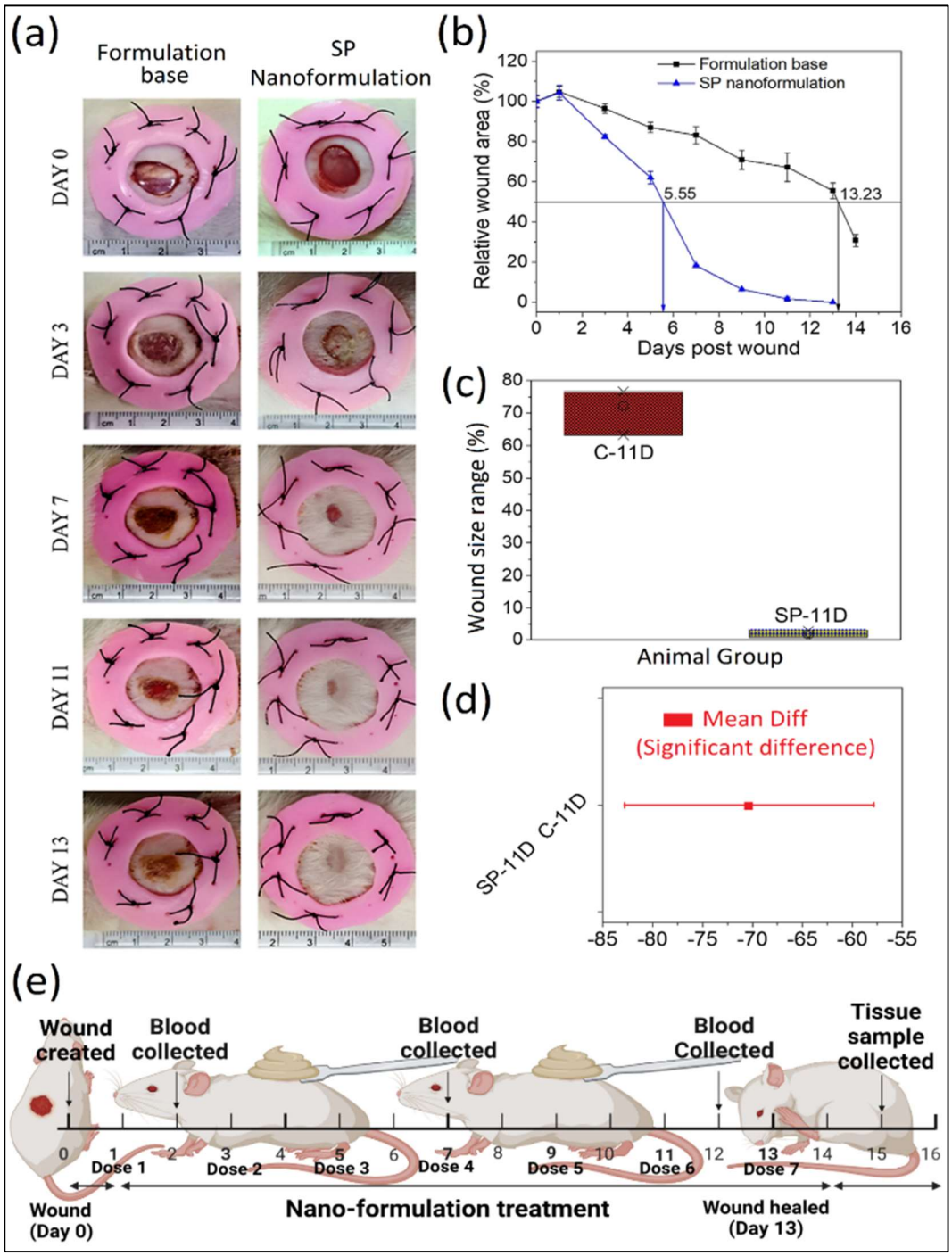

Figure 3.2.12: In vivo wound healing assessment: (a) Macroscopic images of wounds. (b) Measurement of relative wound area remaining to heal. (c) Range of wound size at 11th day that remained to heal. (d) Significant difference representation of mean wound size on the 11th day using the Tukey test to compare the mean. (e) Time-line of in vivo animal experimentation.

However, we observed that the wound closure in the SP nanoformulation-treated rats moved along swiftly, while in the control group (formulation base treated group) was

noticeably delayed (Figure 3.2.12a). These results suggest that SP nanoformulation can accelerate the WH efficiency and can result in full wound closure within 12–13 days of treatment while in the control group, complete wound closure was not achieved even after 15 days of post-treatment. Consequently, the rate of gross wound closure in the treatment group increased at least 5 days earlier compared to the control group.The percentage of wound area was determined to gauge the WH process (Figure 3.2.12b). The corresponding percentages of wound closure in treatment group are found to be 17.6 ±1.1%, 81.7 ±0.4%, and 98.3 ±1.0% and in control group it is found to be 3.6 ±2.4%, 16.9 ±4.3%, and 32.9 ±7.2%, on days 3^{rd}, 7^{th}, and 11^{th} of post-surgery/treatment, respectively. Rat wounds treated with SP nanoformulation heal at a much faster rate than the control for all time points (Figure 3.2.12b). On day 7^{th}, the extent of wound closure is found to be 16.85 ±4.28% for the control group, whereas it is 81.74 ±0.41% for the treatment group. These findings showed that SP nanoformulation has superior healing capacity, which is attributable due to NO release. Further, the histopathology studies have been verified and supported the positive effects of SP nanoformulation on WH, covered in the next section. These findings revealed an apparent propensity for NO therapy to accelerate WH [21, 38]. However, it can also be observed from images (Figure 3.2.12a) that after 3^{rd} day of post-treatment, both treatment and control groups developed dark red-coloured wound scabs, which prevented the passage of further blood and other fluids [30]. Compared to the control group, inflammatory cells in the treatment group have considerably less. This indicates that on 3^{rd} day, the early stages of the inflammatory healing process occurred in all groups, although it progressed more efficiently in the treatment group.

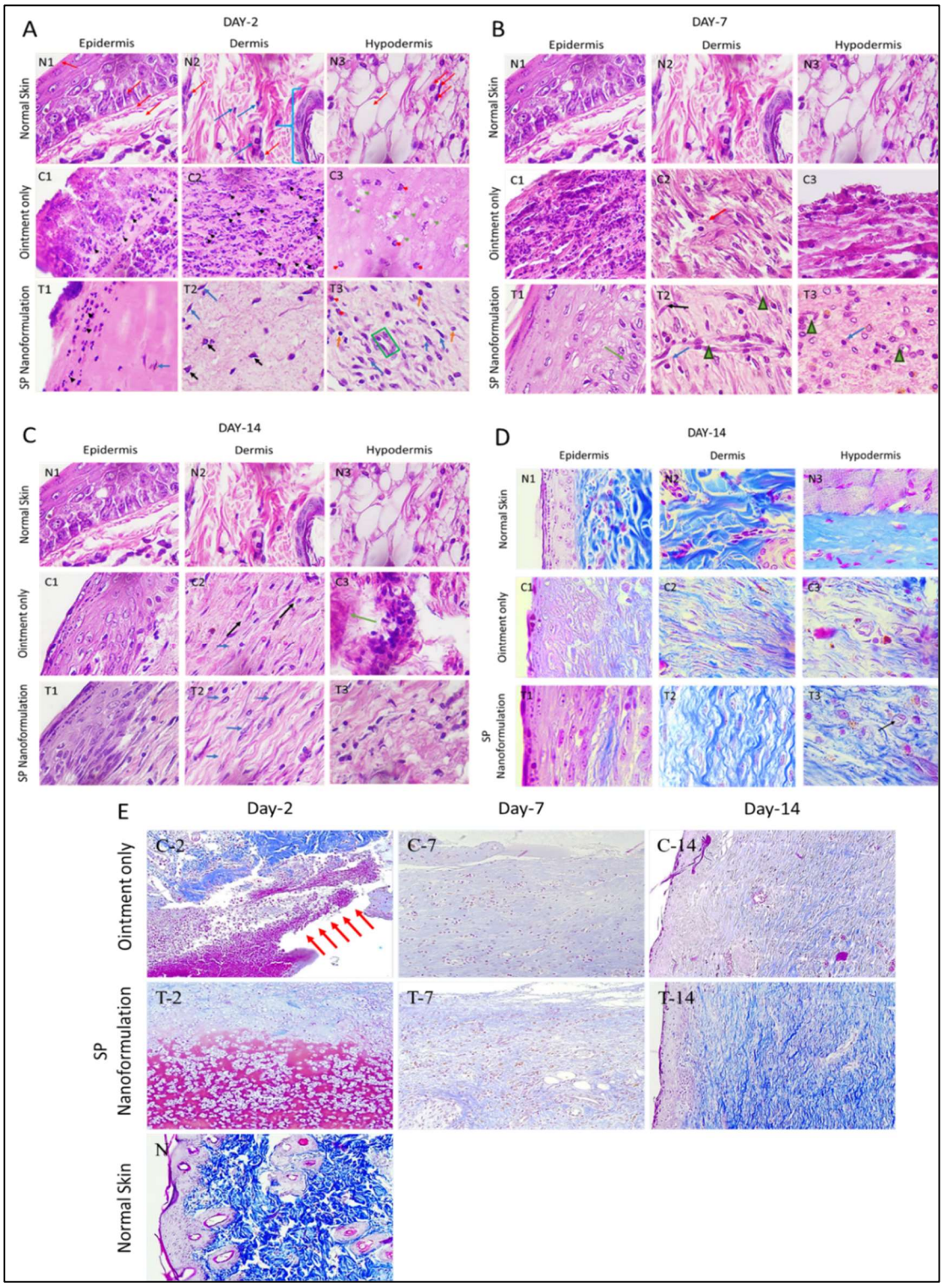

Figure 3.2.13: Histological analysis of skin wound through staining with H & E stain and Mallory's trichrome stain. Histological assessment and comparative histological analysis of wound at post-injury with normal tissue stained with H & E (A, B and C) respectively at 2nd, 7th and 14th day and with Mallory's trichrome stain at 14th day (D) and comparative evaluation on 2nd, 7th and 14th day (E). Letter N, C and T denotes the images of healthy skin, control group (ointment base treated group) and treatment group (SP nanoformulation treated group), respectively. Image A, B, C and D at 100X and E at 20X.

This could happen since NO produced by SP nanoformulation can limit the production of inflammatory mediators and stimulate growth factors like IGF-1 (Figure 3.2.15e), which activate NF-κβ and treat the inflammatory phase while accelerating WH [40]. From images (Figure 3.2.12a), developing layers of skin and wound surrounds are unclear, and these alignments are very loosely maintained because of the inflammatory phase, which promotes platelet clotting and macrophage generation rather than re-epithelialization and dermal remodelling [30]. As anticipated, the granulation tissue production in the treatment group was much higher than in control groups within the 7^{th} day post-treatment. On the 13^{th} day, the wound of the SP nanoformulation-treated group is surrounded and covered by fully developed skin layers, while for the control group, a significant wound area remains to unhealed.

3.2.4.8.3 Histology study

Development of granulation tissue, collagen deposition, and angiogenesis are crucial processes in WH and must be carefully managed. An external infusion of NO can regulate these three aspects of WH [38]. Skin layer morphology was scrutinised during the healing process and shown in this section (Figure 3.2.13). The slices of the wounded skin were stained with H&E and Mallory's trichrome stain to show the formation of granulation tissue and re-epithelialization during WH.

Healthy skin histological features are shown (Figure 3.2.13 A, B, C and D: N1, N2 and N3 and Figure 3.2.13E: N) and after 2^{nd}, 7^{th} and 14^{th} days of post-surgery, for cotrol and SP nanoformulation treated shown in respective images which demonstrated granulation tissue generation (Figure 3.2.13A, B, C, D and E).

Hematoxylin and eosine staining

Healthy Skin (Figure 3.2.13A): Well defined and fully differentiated skin epidermis layer (N1, red arrows), epithelium, in dermis layer some resting fibroblasts (N2, blue arrow)

and active fibroblasts (N2, red arrow), collagen fibre or bundles connected hypodermis, and smooth muscle fibre, skin hair follicle appendages (N2, blue bracket), fat cells and active fibroblasts in hypodermis (N3, red arrow).

Day 2nd of WH (Figure 3.2.13A): Numerous Inflammatory cells (C1 and C2, black arrow) are present below the clot edge and the middle region of wound. Dermal layers shows infiltration of neutrophils and other immune cells (C3, red arrow) in without treatment indicating strong inflammatory reaction and numerous inflammasome are present (C3, green arrow). The clot is very thin (T1), it was removed, whereas fewer inflammatory cells (T1 and T2, black arrow) and fibroblast migration (T1 and T2, blue arrow) in hypodermal wound region can be seen. Few fibroblasts (blue arrow) along with macrophages (black arrow) migrating to dermal region and hypodermal region enriched with some active (blue arrow) and inactive fibroblasts (orange arrow) of wound with fewer inflammatory cells (red arrow) in epidermal region of wounded site. Development of blood vessels has been started as tube forming cells are clubbed (green box).

Day 7th of WH (Figure 3.2.13B): In control group, epidermis is full of inflammatory cells and mashy tissue (C1), fewer fibroblasts along with large immune cells are present in dermal region (C2, red arrow) and inactive fibroblasts in extra cellular matrix are present in the hydermal layer with large and bigger inflammasome (C3) while thick epidermis (T1), numerous blood vessels (T2 and T3, green arrow), immune cells (blue arrow) and numerous active fibroblasts (black arrow) are present in treatment group. Epithelial cells with thicker layer are present in treatment group (T3).

Day 14th of WH (Figure 3.2.13C): In control group, the epidermis with diffused basement membrane and thin stratum corneum, stratum granulosum and thicker stratum spinosum (C1), inactive (C2, black arrow) and active fibrolasts (C2, blue arrow), clumped collagen can be observed may indicate excessive collagen deposition in fibrotic tissue with

clumped fibroblasts whereas treatment group shows, well defined layers of epidermis including stratum corneum, stratum granulosum and stratum spinosum as like to normal skin and basement membrane is also fully developed and differentiated (T1). Elastin like fibres with active fibroblasts with more euchromatin and basophilic cytoplasm with larger nuclei in treatment group are present in dermis layer (T2). T3 represents thick collagen bundles with irregular arrangement and laying cellular components may representing the remodeling state.

Mallory's trichrome staining: "Mallory's trichrome staining" is a histological staining technique used to visualize connective tissues, muscle fibers, and collagen in tissue samples. It's often employed in the study of liver, kidney, and cardiac tissues."

Healthy skin (Figure 3.2.13D and Figure 3.2.13E (N)): Thin pink coloured epidermis and thick blue coloured collagen bundles having irregular arrangement (N1), irregular thick collagen fibres along with skin appendages (hair follicale) (N2), pinnacles muscle layer between hypodermis and dermis (N3).

Control group (Figure 3.2.13D (C1, C2 and C3) and Figure 3.2.13E (C-2, C-7 and C-14): Immature and broken epidermis with diffused basement membrane with minimal collagn deposition was observed, wound edge (C-2, red arrow). Thin collagen bundles (C2 and C-14) with haphazard arrangement with numerous immune cells (C-7) was observed. Regions with less collagen deposition and thin irregular collagen fibres were present (C-7 and C-14).

Treatment group (Figure 3.2.13D and Figure 3.2.13E): Well defined basement membrane with some extent of collagen fibre and well defined layers of epidermis(T1 and T-14). Thicker collagen fibre bundles with elastin fibre like arrangement with other cells (T2) was observed whereas blood capillaries and thicker and more collagen bundles (T-14) irregular arrangement was observed may represent remodelling phase (T3). The SP

nanoformulation treatment group outperformed the control groups with the skin histology features of complete re-epithelialisation, well-differentiated epithelium, and decreased wound scab area.

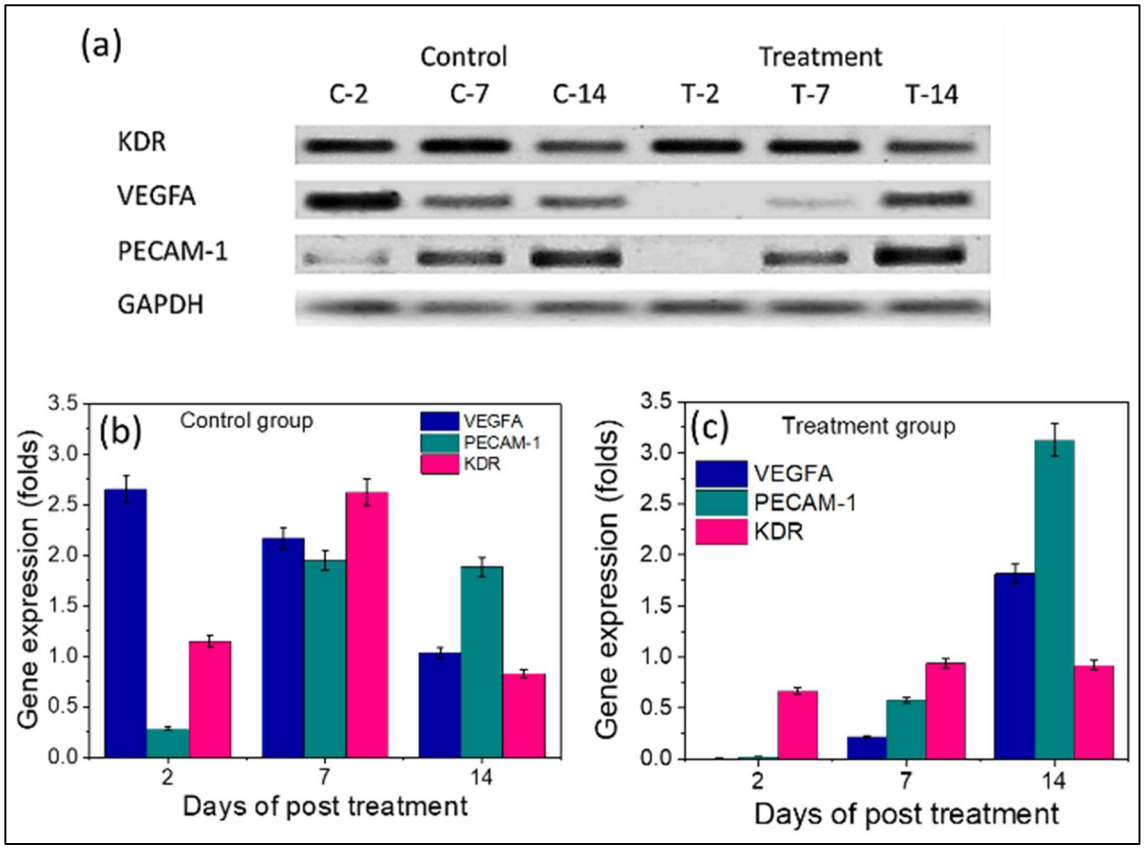

Figure 3.2.14: sqRT-PCR outcomes. (a) Relative expression of various genes during wound healing. (b) and (c) represent the gene expression level relative to GAPDH (in folds) for control and treatment group respectively for VEGFA, PECAM-1 and KDR. In figure, band of gene expression for the day 2 (C-2), day 7 (C-7) and day 14 (C-14) for control group and for the day 2 (T-2), day 7 (T-7) and day 14 (T-14) for the treatment group

The onset of the proliferative phase of WH, as well as the proliferation of keratinocytes, endothelial cells, and fibroblasts, have been demonstrated to be modulated by NO [30]. Therefore, the exogenous administration of NO from SP nanoformulation is anticipated to have similar stimulating effects. These processes, such as re-epithelialization and collagen deposition, would be carried out after the diffusion of NO to wound tissue and hence, NO plays a vital role in the WH process. Therefore, the present formulation can

successfully enhance WH. Additionally, angiogenesis promotes the development of new blood vessels that carry oxygen and nutrients for tissue repair and rebuilding during the healing of wounds [38].

3.2.4.8.4 Semi-quantitative reverse transcription and polymerase chain reaction (sqRT-PCR)

To study the gene expression during the WH a sqRT-PCR study was performed as mentioned in the experimental section and the results have been shown in Figure 3.2.14a-c. Figure 3.2.14a shows the band of gene expression at 2^{nd}, 7^{th}, and 14^{th} day for control (C-2, C-7 and C-14) and for treatment group (T-2, T-7 and T-14), repectively. It can be noted that the GAPDH is a housekeeping gene and is used as a reference control in gene expression analysis. Furthermore, in our study, the gene expression analysis using sqRT-PCR revealed that the expression level for KDR gene is found to be higher in the control group with respect to the treatment group for all the treatment days (Figure 3.2.14b and c), however, the gene expression difference is non-significant. In WH, the VEGFA plays both direct and indirect role. Under the influence of VEGFA the migration of inflammatory cells and keratinocytes with inducing proliferation and collagen deposition in the remodelling phase takes place [41].

VEGFA is also interact with receptor KDR and mediate the internalisation of KDR to the nucleus and, finally activation of PI3-kinase/AKT occurred [42]. The expression of VEGFA is higher on Day 2^{nd} and downregulated at day 7^{th} and 14^{th} in the control group (Figure 3.2.14b and c). This high expression could have occurred due to the increased migration of inflammatory cells to the wounded region in the control group. While, in the treatment group, the VEGFA expression was observed downregulated on day 2^{nd} and observed at base line on day 7^{th} and increased on Day 14^{th} of treatment. These results suggested that the SP NPs formulation have a major role in enhancing the scarless WH.

Similarly, PECAM-1 (CD31) plays a central regulatory role in WH as a representive of angiogenesis. However, the increased expression of PECAM-1 is occurred with day of treatment in the control group. In the treatment group, on day 2 the PECAM-1 expression was downregulated, whereas for day 7 and 14 of post treatment, the same has been increased compared to the control group (Figure 3.2.14). Thus, SP nanoformulation has regulatory effect on KDR, VEGFA and PECAM-1 expression for the regeneration of wounded tissue.

3.2.4.8.5 Wound healing markers and inflammation study

On the inflammatory phase (2^{nd} day), proliferative phase (7^{th} day), and remodelling phase (12^{th} day) of wounding, levels of cytokines in the blood serum of treatment and control group were determined by ELISA to assess the effects of SP nanoformulation. During these phases, the level of cytokines changed significantly, demonstrating the impact of SP nanoformulation. It is also observed that on the 2^{nd}, 7^{th} and 12^{th} day of post-treatment, the relative levels of TNF-α, IL-1β, and IL-6 were considerably low in the treatment group than the control group (Figure 3.2.15). The C-reactive protein (CRP) is a blood protein that is seen in the acute phase and activates complement. In reaction to inflammatory cytokines, the liver releases CRP into the bloodstream. Herein, after tissue injury, CRP level quickly rises in response to inflammation and infection, then drops as the wound heals, and relative CRP levels are significantly lowered in the treatment group compared to the control group. On the 7^{th} and 12^{th} day, IGF-1 levels in the treatment group are considerably higher (Figure 3.2.15e), suggesting a higher likelihood of keratinocyte migration to the injured areas during the proliferation and remodelling phase [43].

In contrast, control groups have lower levels of IGF-1, while having high levels of pro-inflammatory cytokines (TNF-α, IL-1β, and IL-6). These deterrent effects on levels of pro-inflammatory cytokines are found due to the regulated NO release from SP

nanoformulation. Thus, it can be concluded that the NO functioned as an anti-inflammatory agent, and SP nanoformulation successfully protects the cells from inflammation via controlled-release profiles [44].

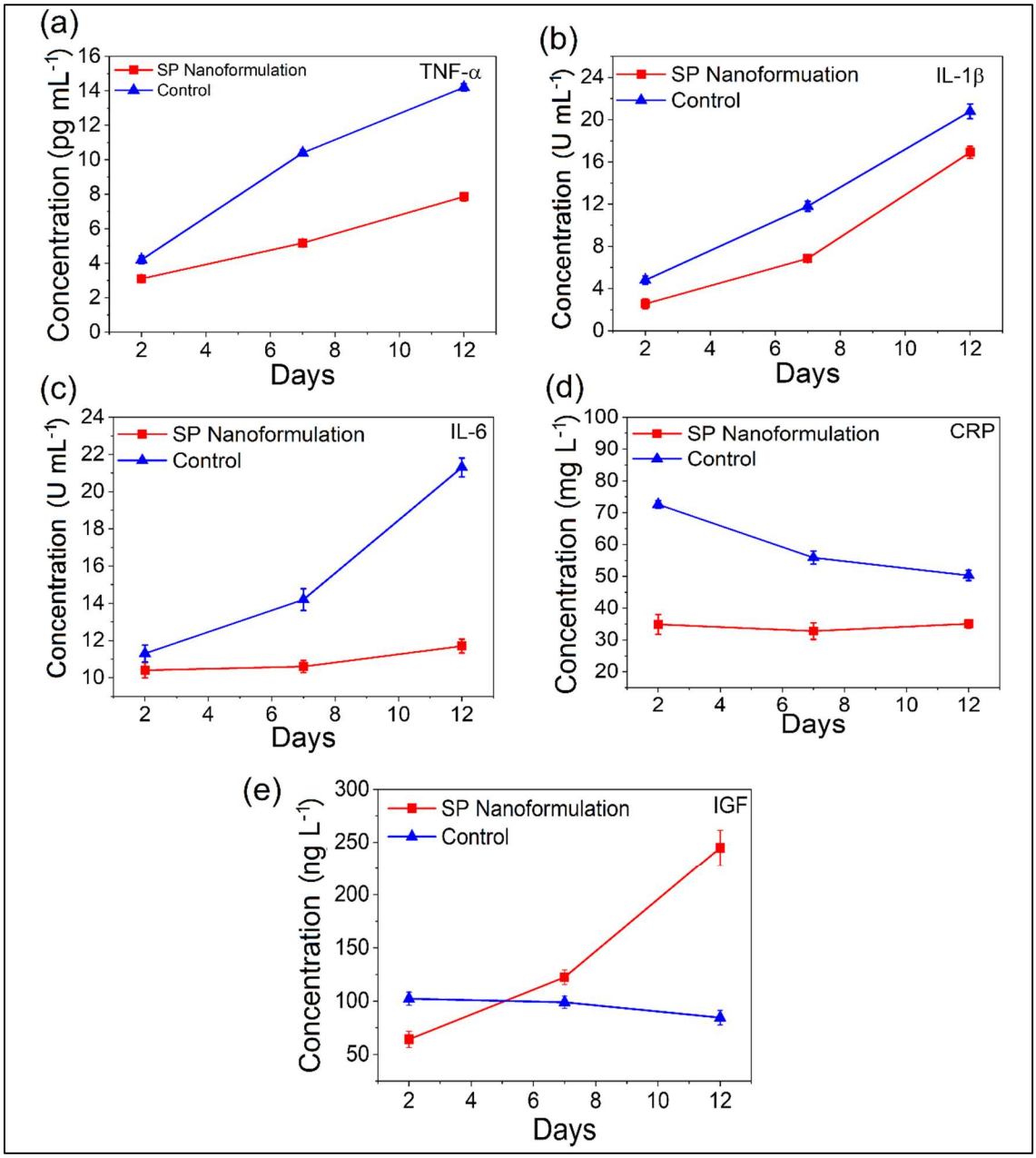

Figure 3.2.15: Wound healing markers analysis by ELISA on the 2nd, 7th and 12th days of post-wounding. (a) TNF-α, (b) IL-1β, (c) IL-6, (d) CRP and (e) IGF-1 levels. Each data point represents the average (± SD) of 3 independent determinations ($p<0.05$).

3.2.5 DISCUSSION

This study has formulated water-dispersible NO-releasing biosafe advanced polymeric

SP NPs by free radical polymerisation and subsequently loading with SNP. FTIR shows characteristic bands of cyano, NO and Fe-NO groups at 2148 cm^{-1}, 1941 cm^{-1}, and 662 cm^{-1} that confirmed the formation of NO-releasing NPs (SP NPs) (Figure 3.2.3c). Many parameters, such as formulation components, manufacturing processes or process factors including time, temperature, pressure, instrument type, lyophilisation, packaging and storage conditions, have an impact the average particle diameter of NPs. The particle size requirement and distribution of well-designed nanosystems should be in the submicron range [45] because the interactions between biochemical and cellular components of cells and nanocarriers take place only when particles are typically smaller than 200 nm, these interactions are distinct from those arising from relatively larger particles or implants made of biomaterials [46]. Therefore, using TEM and DLS, the morphology, size and distribution were examined, and due to an average size of 162 nm (dia), these SP NPs potentially exhibited bioactivity. Herein, zeta potential (ξ) found ~-32.8 mV, represents the colloidal stability of the SP NPs [45]. Due to the abundance of anionic carboxylate groups, SP NPs are stabilised by electrostatic repulsion and steric stabilisation. Drug loading is crucial when fabricating an NP-based delivery system since low loading requires significantly more formulation for an optimum therapeutic effect [47, 48]. Therefore, low drug loading is an obstacle to using nanotherapeutics, necessitating high LC and EE. Herein, high LC (48.23 ±5.63%) and high EE (40.97 ±1.52%) were found for SP NPs. The loading of SNP also confirmed by the elemental analysis of SP NPs which shows the availability of Fe and Na as metallic component of SNP (Figure 3.2.4). This proves that in fewer doses, SP NPs can deliver more NO. The reason for this high LC and EE are cross-linking of PNAG NPs with DVB, which also helps to retain their good water dispersibility. Thus, SP NPs also have good NO content measured as 98.29 ±2.79%, equivalent to 1.59 ±0.04 μmol mg^{-1} of SP NPs.

In vitro release plays several crucial functions during a drug product development and life cycle from the viewpoint of quality product. Thus, the quality control strategy at the early and late stages of product development guarantees batch-to-batch consistency and uniformity [49]. According to the literature, SNP's mean plasma elimination half-life in aqueous solution is around 2 minutes [50]. In the study of NO delivering and releasing biomaterials, the release time is one of the essential performance parameters. Numerous studies were done to modulate the release of NO [51-54]. The *in vitro* release of NO entrapped on the SP NPs was investigated in PBS at pH 7.4 and temperature 37 ±2°C to simulate the intestinal environment and CDR (%) was found to be 97.37 ±8.19% within 24 h. Figure 3.2.5 demonstrates that SP NPs successfully regulate and lower the release rate of NO. The requirement for frequent dosages may decrease with persistent NO administration. A regulated NO release is crucial for the actual clinical application of NO-releasing biomaterials [55]. For rapid and long-term pharmacological actions from NO-releasing biomaterials, sustained NO release for at least 24 h is necessary since once-daily dosing for chronic disorders can be manageable.

A successful demonstration of NPs biocompatibility through a series of *in vitro* and *in vivo* tests may evaluate cytotoxic or immunological impact triggered after their administration is required for the regulatory approval of innovative nanocarriers. An ideal material for a wound dressing should be biocompatible, reduce inflammatory receptivity, manage inflammation, and accelerate WH [40]. The clinical availability of nanocarriers for delivering medicines to target diseased tissues more successfully depends on an accurate biocompatibility assessment. It is well known that interactions between cells and biomaterials can lead to protein adsorption and cell contacts, activating host defence mechanisms such as thrombogenicity and inflammation. These reactions may result from the body directly detecting nano-biomaterials or an unintentional release of pro-

inflammatory cytokines, which results in cytotoxicity and, subsequently, loss of cell integrity in response to nano-biomaterials [56]. In this work, we found that SP NPs are well tolerated by mouse fibroblasts (L929) cells, exhibiting proliferation (Figure 3.2.6a) and do not cause cytotoxicity while exhibiting acceptable hemolysis (Figure 3.2.6d and e) at the highest concentration (1 mg mL^{-1}) tested for therapeutic purpose and having no adverse effects on the coagulation cascade (Figure 3.2.6b and c). Therefore, the absence of cytotoxicity assures the potential of SP NPs can be used for *in vivo* application. The experiments showed that SP NPs are biocompatible and have the potential to stimulate cell growth when loaded with SNP, and these findings also pointed to NO's cytoprotective properties. Therefore, our studies demonstrate both the biocompatibility of SP NPs and its ability to promote cell proliferation when loaded with SNP.

Conventional bioequivalence techniques based on plasma pharmacokinetic data sometimes may not be feasible and may not produce relevant results; in such a case demonstrating the therapeutic equivalence of topical semi-solid therapeutic might be difficult. Suppose two formulations (test and reference) release medication at different rates when compared under the same circumstances and when the case reference data are unavailable. In that case, an *in vitro* release test can reveal the most significant information changes in the microstructure of the two formulations [37]. As a result, the *in vitro* release test is crucial in determining how well a medication product performs.

The role of NO in WH is extensively explored [57]. It has been challenging to identify which of NO's functions could modulate WH, although the different effects of NO depend on the location and concentration because several elements and modulators affect WH. To mimic the cutaneous WH processes more closely, sterile silicone rings are stitched around the wound in our investigation, which avoids WH through tissue contraction. This mechanism was utilised to focus on the re-epithelialization process as a crucial stage in

WH since skin contraction is more evident in murine models of WH than in human wounds. We observed that NO treatment promotes tissue repair after damage by direct re-epithelialization (Figure 3.2.12).

Our findings also demonstrated that the topically applying SP nanoformulation to skin wounds in rats supplemented NO levels slightly above physiological levels and markedly speed up the WH process [43]. Notably, by entering the cell and assaulting microbes DNA and cellular machinery, NO is anti-microbial, successfully boosting the host immune system and helping eliminate the microbial burden [21, 52, 58, 59].

SP nanoformulation enhances WH by fostering fibroblast migration and collagen depositions at the site of the injured area. By enhancing fibroblasts proliferative capability and motility, increased granulation tissue development hastens WH [60]. SP NPs significantly increased the number of fibroblasts in the scratched region of a plate, indicating particles up-regulate fibroblasts mobility and proliferation (Figure 3.2.6a and Figure 3.2.7) simultaneously not inducing any adverse effect which may cause toxicity to cells and may result in the death of fibroblasts (Figure 3.2.8). Fibroblasts are crucial in the regeneration of new tissue in wounded regions, as they create the groundwork for the keratinocyte's migration and finally for the WH. When considered as a whole, these findings demonstrated that the NO seems to be involved in controlling fibroblast migration and proliferation through interlinked processes, eventually improving WH (Figure 3.2.7).

Earlier findings concerning the function of NO are encouraging to angiogenesis [61, 62]. In comparison to the untreated CEMA, the SP NPs treated CEMA showed much more significant vascular sprouting (Figure 3.2.9). The quantitative data demonstrates that SP NPs treated with 1 and 10 µg cause a significant rise in the development and maturation of blood vessels, but at higher dose (100 µg) it exhibits adverse actions during the starting

hours of dosing (development of distorted and damaged vasculature). These findings imply that SP NPs have both pro-angiogenic and anti-angiogenic effects, depending on the dosage. The mechanism of the angiogenic effect can be given in the context that enhancing and recruiting angiogenesis-supporting elements like TGF-β and vascular endothelial growth factor (VEGF) provide enough blood flow towards a healing wound, and NO can support improved WH [60]. For instance, TGF-β helps to increase the tissue debridement at the wound site brought on by macrophages and results to encourages the recruitment of more and more inflammatory cells. Here, we postulated that by controlling and regulating the interactions among the fibroblasts, inflammatory cells, cytokines, and remodelling proteins, the topical administration of NO-releasing nanoformulation could reduce the time and accelerates the rate of WH [60].

Additionally, NO's favourable effects on fibroblast migration and proliferation enhanced effectiveness and accelerated WH. The SP nanoformulation with huge potency undoubtedly caused by NPs changes the biodistribution and release of NO (Figure 3.2.10) [63]. With the topical administration of the SP NPs nanoformulation, we did not see any adverse effects in the form of skin irritation and sensitivity (Figure 3.2.11), which is in line with other study [60] showed topically administered NO-releasing NPs might cause local immunological modulation with minor inflammation (Figure 3.2.15). The application of nanotechnology in the delivery of NO can make it possible to administer a precise dosage which would adequately heal the wound in a regulated manner without producing undesirable outcomes such as tissue damage or severe scarring confirmed through the expression of various gene during the WH treatment. An important protein expressed during wound haling is VEGFA, which have both direct and indirect effect on WH [41]. The relatively higher expression of VEGFA in control group on day-2 is responsible for the attraction of inflammatory cells while the level of same is decreasing

in control group as time shows improper healing as VEGFA is responsible for angiogenesis, inflammation, cell proliferation and migration, granulation tissue formation, collagen synthesis and finally wound contraction [41], which is accordingly expressing higher in the treatment group and accelerating the healing process through the above said mechanisms (Figure 3.2.14). The dynamic regulation of KDR gene expression is cruscial for orchestrating the angiogenic response during WH. Proper control of KDR activation ensures the formation of a functional vascular network that supports the delivery of oxygen, nutrients, and immune cells to the healing tissue, ultimately promoting effective wound repair [64], Another important aspect of accelerated WH is the expression of PECAM-1 molecules which involved in the regulation of endothelial cell function and leukocyte recruitment, during the initial stages of WH, it involved in leukocyte recruitment and migration to the site of injury and regulates a critical step in the inflammatory response [65]. Availability of PECAM-1 during later stage of WH is necessary because it also promotes the tissue undergoes remodeling and maturation contribute to the maintenance of vascular integrity during tissue repair [66]. Thus, our early outcomes are promising and encouraging to apply these polymeric nanobiomaterials for regenerative nanomedicine. Additionally, it would be appropriate to carefully examine the suitability of SP NPs and their nanoformulation for long-term, non-healing wounds and for enhancing difficult WH. However, long-term investigations are necessary to evaluate the potential consequences of administering SP NPs and its topical nanoformulation on the skin [60, 63].

3.2.6 CONCLUSIONS

The synthesised novel PNAG NPs are loaded with NO donor (SNP) and transformed into NO-releasing PNAG NPs (SP NPs) with high loading efficiency. SP NPs can be used to deliver the NO *in vitro* and *in vivo*. The prepared system can release NO in PBS (pH 7.4

and 6.8) for more than 24 h when tested *in vitro*. The cytotoxicity analysis indicated that SP NPs exhibited good biocompatibility in mouse fibroblast (L929) cell lines and displayed negligible hemolytic behaviour on rat RBCs. To evaluate the effect of SP NPs on promoting WH, we prepared SP NPs impregnated nanoformulation using an oleaginous ointment base for enhancing residence time and smooth application during application. The nanoformulation is non-irritant for rat's skin. Both NO and PNAG NPs show synergistic effects on cutaneous WH by enhancing granulation tissue formation, collagen depositions, angiogenesis and regulating cytokines and chemokines and may prove superior compared to the traditional treatment methods. Therefore, SP NPs and SP nanoformulation is a versatile NO-releasing formulation with a promising future in regenerative medicine and is paramount for therapeutic technology.

3.2.7 REFERENCES

1. Wang, S., et al., *Responsive hydrogel dressings for intelligent wound management.* BMEMat, 2023. **1**(2): p. e12021. DOI: https://doi.org/10.1002/bmm2.12021.

2. Sen, C.K., *Human Wound and Its Burden: Updated 2020 Compendium of Estimates.* Adv Wound Care (New Rochelle), 2021. **10**(5): p. 281-292. DOI: 10.1089/wound.2021.0026.

3. Shukla, V.K., M.A. Ansari, and S.K. Gupta, *Wound Healing Research: A Perspective From India.* The International Journal of Lower Extremity Wounds, 2005. **4**(1): p. 7-8. DOI: 10.1177/1534734604273660.

4. Abaffy, P., et al., *The role of nitric oxide during embryonic wound healing.* BMC Genomics, 2019. **20**(1): p. 815. DOI: 10.1186/s12864-019-6147-6.

5. LUO, J.-d. and A.F. CHEN, *Nitric oxide: a newly discovered function on wound healing.* Acta Pharmacologica Sinica, 2005. **26**(3): p. 259-264. DOI: https://doi.org/10.1111/j.1745-7254.2005.00058.x.

6. Friebe, A., P. Sandner, and A. Schmidtko, *cGMP: a unique 2nd messenger molecule–recent developments in cGMP research and development.* Naunyn-schmiedeberg's Archives of Pharmacology, 2020. **393**: p. 287-302.

7. Wang, X., et al., *Flourishing Antibacterial Strategies for Osteomyelitis Therapy.* Advanced Science, 2023. **10**(11): p. 2206154. DOI: https://doi.org/10.1002/advs.202206154.

8. Yang, Y., et al., *Nitric oxide based strategies for applications of biomedical devices.* Biosurface and Biotribology, 2015. **1**(3): p. 177-201. DOI: https://doi.org/10.1016/j.bsbt.2015.08.003.

9. Bernatchez, S.F., et al., *Nitric oxide levels in wound fluid may reflect the healing trajectory.* Wound Repair and Regeneration, 2013. **21**(3): p. 410-417. DOI: https://doi.org/10.1111/wrr.12048.

10. Yamasaki, K., et al., *Reversal of impaired wound repair in iNOS-deficient mice by topical adenoviral-mediated iNOS gene transfer.* J Clin Invest, 1998. **101**(5): p. 967-71. DOI: 10.1172/jci2067.

11. Lee, P.C., et al., *Impaired wound healing and angiogenesis in eNOS-deficient mice.* Am J Physiol, 1999. **277**(4): p. H1600-8. DOI: 10.1152/ajpheart.1999.277.4.H1600.

12. Lizarbe, T.R., et al., *Nitric oxide elicits functional MMP-13 protein-tyrosine nitration during wound repair.* FASEB J, 2008. **22**(9): p. 3207-15. DOI: 10.1096/fj.07-103804.

13. Amadeu, T.P. and A.M.A. Costa, *Nitric oxide synthesis inhibition alters rat cutaneous wound healing.* Journal of Cutaneous Pathology, 2006. **33**(7): p. 465-473. DOI: https://doi.org/10.1111/j.1600-0560.2006.00472.x.

14. Malone-Povolny, M.J., S.E. Maloney, and M.H. Schoenfisch, *Nitric Oxide Therapy for Diabetic Wound Healing.* Adv Healthc Mater, 2019. **8**(12): p. e1801210. DOI: https://doi.org/10.1002/adhm.201801210.

15. Shekhter, A.B., et al., *Beneficial effect of gaseous nitric oxide on the healing of skin wounds.* Nitric Oxide, 2005. **12**(4): p. 210-219. DOI: https://doi.org/10.1016/j.niox.2005.03.004.

16. Badr, G., et al., *Bee Venom Accelerates Wound Healing in Diabetic Mice by Suppressing Activating Transcription Factor-3 (ATF-3) and Inducible Nitric Oxide Synthase (iNOS)-Mediated Oxidative Stress and Recruiting Bone Marrow-Derived Endothelial Progenitor Cells.* 2016. **231**(10): p. 2159-2171. DOI: https://doi.org/10.1002/jcp.25328.

17. Shalaby, M.A., M.M. Anwar, and H. Saeed, *Nanomaterials for application in wound Healing: current state-of-the-art and future perspectives.* Journal of Polymer Research, 2022. **29**(3): p. 91. DOI: 10.1007/s10965-021-02870-x.

18. Riccio, D.A. and M.H. Schoenfisch, *Nitric oxide release: Part I. Macromolecular scaffolds.* Chemical Society Reviews, 2012. **41**(10): p. 3731-3741. DOI: 10.1039/C2CS15272J.

19. Yamala, A.K., et al., *Poly-N-acryloyl-(l-phenylalanine methyl ester) hollow core nanocapsules facilitate sustained delivery of immunomodulatory drugs and exhibit adjuvant properties.* Nanoscale, 2017. **9**(37): p. 14006-14014. DOI: 10.1039/C7NR03724D.

20. Quinn, J.F., M.R. Whittaker, and T.P. Davis, *Delivering nitric oxide with nanoparticles.* Journal of Controlled Release, 2015. **205**: p. 190-205. DOI: https://doi.org/10.1016/j.jconrel.2015.02.007.

21. Cao, J., et al., *Nitric Oxide-Releasing Thermoresponsive Pluronic F127/Alginate Hydrogel for Enhanced Antibacterial Activity and Accelerated Healing of Infected Wounds.* Pharmaceutics, 2020. **12**(10): p. 926. DOI: https://doi.org/10.3390/pharmaceutics12100926.

22. Li, M., et al., *Antimicrobial Nitric Oxide-Releasing Electrospun Dressings for Wound Healing Applications.* ACS Materials Au, 2022. **2**(2): p. 190-203. DOI: 10.1021/acsmaterialsau.1c00056.

23. Bindu, T.H., et al., *Preparation and evaluation of chitosan-gelatin composite films for wound healing activity.* 2010. **24**(3): p. 122-130.

24. Wei, D. and X. Zhang, *Biosynthesis, bioactivity, biotoxicity and applications of antimicrobial peptides for human health.* Biosafety and Health, 2022. **4**(2): p. 118-134. DOI: https://doi.org/10.1016/j.bsheal.2022.02.003.

25. Zhang, Y., et al., *Microneedle system for tissue engineering and regenerative medicine.* Exploration, 2023. **3**(1): p. 20210170. DOI: https://doi.org/10.1002/EXP.20210170.

26. Yang, J. and J. Ding, *Nanoantidotes: A Detoxification System More Applicable to Clinical Practice.* 2023. **4**: p. 0020. DOI: doi:10.34133/bmef.0020.

27. Shimanovich, U., et al., *Tetracycline Nanoparticles as Antibacterial and Gene-Silencing Agents.* Advanced Healthcare Materials, 2015. **4**(5): p. 723-728. DOI: https://doi.org/10.1002/adhm.201400631.

28. WHO. *WHO model list of essential medicines, 20th list (March 2017, amended August 2017)*. 2017 [cited 2023 12-05-2023]; Available from: https://apps.who.int/iris/bitstream/handle/10665/273826/EML-20-eng.pdf.

29. Ahmed, R., et al., *Nitric oxide-releasing biomaterials for promoting wound healing in impaired diabetic wounds: State of the art and recent trends.* Biomedicine & Pharmacotherapy, 2022. **149**: p. 112707. DOI: https://doi.org/10.1016/j.biopha.2022.112707.

30. Kang, Y., et al., *Nitric oxide-releasing polymer incorporated ointment for cutaneous wound healing.* Journal of Controlled Release, 2015. **220**: p. 624-630. DOI: https://doi.org/10.1016/j.jconrel.2015.08.057.

31. Razmi, H. and H.J.A.B. Heidari, *Nafion/lead nitroprusside nanoparticles modified carbon ceramic electrode as a novel amperometric sensor for l-cysteine.* 2009. **388**(1): p. 15-22.

32. Xun, Z., et al., *Effects of a surfactant on the electrocatalytic activity of cobalt hexacyanoferrate modified glassy carbon electrode towards the oxidation of dopamine.* 2004. **16**(8): p. 674-683.

33. Chakraborty, A., et al., *Nanoparticle-Reinforced Tough Hydrogel as a Versatile Platform for Pharmaceutical Drug Delivery: Preparation and in Vitro Characterization.* Molecular Pharmaceutics, 2023. **20**(1): p. 767-774. DOI: 10.1021/acs.molpharmaceut.2c00564.

34. Goyal, T. and C.L. Schmotzer, *Validation of Hemolysis Index Thresholds Optimizes Detection of Clinically Significant Hemolysis.* American Journal of Clinical Pathology, 2015. **143**(4): p. 579-583. DOI: 10.1309/ajcpdude1hra0ymr.

35. Li, R., et al., *Bioactive materials promote wound healing through modulation of cell behaviors.* Advanced Science, 2022. **9**(10): p. 2105152.

36. Mukherjee, S., et al., *Graphene oxides show angiogenic properties.* Advanced healthcare materials, 2015. **4**(11): p. 1722-1732.

37. Kamal, N.S., et al., *Identification of critical formulation parameters affecting the in vitro release, permeation, and rheological properties of the acyclovir topical cream.* International Journal of Pharmaceutics, 2020. **590**: p. 119914. DOI: https://doi.org/10.1016/j.ijpharm.2020.119914.

38. Zhang, Y., et al., *A polyethylenimine-based diazeniumdiolate nitric oxide donor accelerates wound healing.* Biomaterials Science, 2019. **7**(4): p. 1607-1616. DOI: 10.1039/C8BM01519H.

39. González, R., et al., *Regulation of Cell Survival, Apoptosis, and Epithelial-to-Mesenchymal Transition by Nitric Oxide-Dependent Post-Translational Modifications.* Antioxidants & Redox Signaling, 2017. **29**(13): p. 1312-1332. DOI: 10.1089/ars.2017.7072.

40. Deng, P., et al., *Chitosan-based hydrogels with injectable, self-healing and antibacterial properties for wound healing.* Carbohydrate Polymers, 2022. **276**: p. 118718. DOI: https://doi.org/10.1016/j.carbpol.2021.118718.

41. Wilgus, T.A., *Vascular Endothelial Growth Factor and Cutaneous Scarring.* Adv Wound Care (New Rochelle), 2019. **8**(12): p. 671-678. DOI: 10.1089/wound.2018.0796.

42. Constantino Rosa Santos, S., et al., *VEGF and VEGFR-2 (KDR) internalization is required for endothelial recovery during wound healing.* Experimental Cell Research, 2007. **313**(8): p. 1561-1574. DOI: https://doi.org/10.1016/j.yexcr.2007.02.020.

43. Póvoa, V.C.O., et al., *Wound healing action of nitric oxide-releasing self-expandable collagen sponge.* 2020. **14**(6): p. 807-818. DOI: https://doi.org/10.1002/term.3046.

44. Oh, Y., et al., *Controlled Nitric Oxide Release Using Poly(lactic-co-glycolic acid) Nanoparticles for Anti-Inflammatory Effects.* Biomacromolecules, 2020. **21**(12): p. 4972-4979. DOI: 10.1021/acs.biomac.0c01176.

45. Moreno-Sastre, M., et al., *Stability study of sodium colistimethate-loaded lipid*

nanoparticles. J Microencapsul, 2016. **33**(7): p. 636-645. DOI: 10.1080/02652048.2016.1242665.

46. Ernst, L.M., et al., *The Interactions between Nanoparticles and the Innate Immune System from a Nanotechnologist Perspective.* 2021. **11**(11): p. 2991.

47. Tan, J., et al., *Surface Modification of Cisplatin-Complexed Gold Nanoparticles and Its Influence on Colloidal Stability, Drug Loading, and Drug Release.* Langmuir, 2018. **34**(1): p. 154-163. DOI: 10.1021/acs.langmuir.7b02354.

48. Thauvin, C., et al., *Functionalized PLA polymers to control loading and/or release properties of drug-loaded nanoparticles.* International Journal of Pharmaceutics, 2018. **548**(2): p. 771-777. DOI: https://doi.org/10.1016/j.ijpharm.2017.11.001.

49. Xu, X., et al., *Kinetics of drug release from ointments: Role of transient-boundary layer.* International Journal of Pharmaceutics, 2015. **494**(1): p. 31-39. DOI: https://doi.org/10.1016/j.ijpharm.2015.07.077.

50. Holme, M.R. and T. Sharman. *Sodium nitroprusside*. 2020 24-05-2022 [cited 2023 07-05-2023]; StatPearls [Internet]. Treasure Island (FL):[Available from: https://www.ncbi.nlm.nih.gov/books/NBK557487/.

51. Liu, S., et al., *Chitosan derivatives co-delivering nitric oxide and methicillin for the effective therapy to the methicillin-resistant S. aureus infection.* Carbohydrate Polymers, 2020. **234**: p. 115928. DOI: https://doi.org/10.1016/j.carbpol.2020.115928.

52. Lee, J., et al., *In vitro and in vivo evaluation of a novel nitric oxide-releasing ointment for the treatment of methicillin-resistant Staphylococcus aureus-infected wounds.* Journal of Pharmaceutical Investigation, 2020. **50**(5): p. 505-512. DOI: 10.1007/s40005-020-00472-1.

53. Duong, H.T.T., et al., *Intracellular nitric oxide delivery from stable NO-polymeric nanoparticle carriers.* Chemical Communications, 2013. **49**(39): p. 4190-4192. DOI: 10.1039/C2CC37181B.

54. Huang, M., et al., *Stearic acid modified nano CuMOFs used as a nitric oxide carrier for prolonged nitric oxide release.* RSC Advances, 2022. **12**(4): p. 2383-2390. DOI: 10.1039/D1RA08066K.

55. Ghalei, S., M. Douglass, and H. Handa, *Nitric Oxide-Releasing Gelatin Methacryloyl/Silk Fibroin Interpenetrating Polymer Network Hydrogels for Tissue Engineering Applications.* ACS Biomaterials Science & Engineering, 2022. **8**(1): p. 273-283. DOI: https://doi.org/10.1021/acsbiomaterials.1c01121.

56. Rout, G.K., et al., *Current advances in nanocarriers for biomedical research and their applications.* Artificial Cells, Nanomedicine, and Biotechnology, 2018. **46**(sup2): p. 1053-1062. DOI: 10.1080/21691401.2018.1478843.

57. Wu, M., et al., *Recent advances in the development of nitric oxide-releasing biomaterials and their application potentials in chronic wound healing.* Journal

of Materials Chemistry B, 2021. **9**(35): p. 7063-7075. DOI: 10.1039/D1TB00847A.

58. Lee, J., et al., *Nitric Oxide-Releasing S-Nitrosoglutathione-Conjugated Poly(Lactic-Co-Glycolic Acid) Nanoparticles for the Treatment of MRSA-Infected Cutaneous Wounds.* Pharmaceutics, 2020. **12**(7): p. 618. DOI: https://doi.org/10.3390/pharmaceutics12070618.

59. Nurhasni, H., et al., *Nitric oxide-releasing poly(lactic-co-glycolic acid)-polyethylenimine nanoparticles for prolonged nitric oxide release, antibacterial efficacy, and in vivo wound healing activity.* Int J Nanomedicine, 2015. **10**: p. 3065-80. DOI: 10.2147/ijn.S82199.

60. Han, G., et al., *Nitric Oxide–Releasing Nanoparticles Accelerate Wound Healing by Promoting Fibroblast Migration and Collagen Deposition.* The American Journal of Pathology, 2012. **180**(4): p. 1465-1473. DOI: https://doi.org/10.1016/j.ajpath.2011.12.013.

61. Mukherjee, S., et al., *Graphene Oxides Show Angiogenic Properties.* Adv Healthc Mater, 2015. **4**(11): p. 1722-32. DOI: https://doi.org/10.1002/adhm.201500155.

62. Yamamoto, N., et al., *VEGF and bFGF induction by nitric oxide is associated with hyperbaric oxygen-induced angiogenesis and muscle regeneration.* Scientific Reports, 2020. **10**(1): p. 2744. DOI: 10.1038/s41598-020-59615-x.

63. Pereverzeva, E., et al., *Toxicological study of doxorubicin-loaded PLGA nanoparticles for the treatment of glioblastoma.* Int J Pharm, 2019. **554**: p. 161-178. DOI: 10.1016/j.ijpharm.2018.11.014.

64. Bao, P., et al., *The role of vascular endothelial growth factor in wound healing.* J Surg Res, 2009. **153**(2): p. 347-58. DOI: 10.1016/j.jss.2008.04.023.

65. Martin, P. and S.J. Leibovich, *Inflammatory cells during wound repair: the good, the bad and the ugly.* Trends in Cell Biology, 2005. **15**(11): p. 599-607. DOI: https://doi.org/10.1016/j.tcb.2005.09.002.

66. Woodfin, A., et al., *PECAM-1: a multi-functional molecule in inflammation and vascular biology.* 2007. **27**(12): p. 2514-2523.

CHAPTER 3: PART III

3.3 Comprehensive Biological Activity Assessment of Metal Oxides in Wound Healing

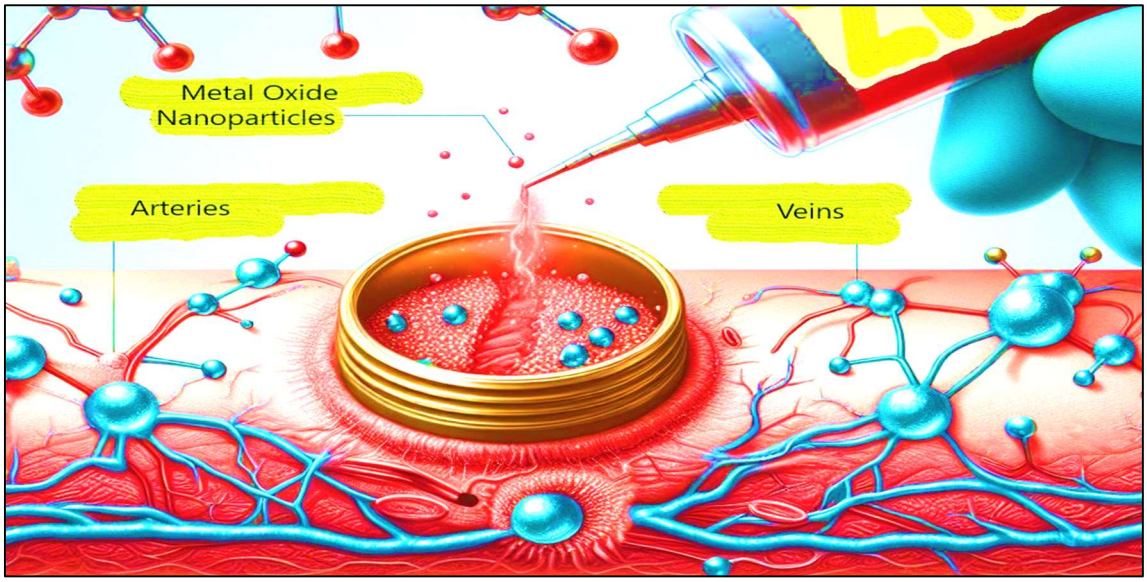

Figure 3.3.1: Illustrative image showing the metal oxide nanoparticles penetrating the deep tissue, interacting with microbes, creating a protective aura in the wound microenvironment and supporting the vascular system.

3.3.1 ABSTRACT

The third objective of my thesis revolves around the biological assessment of MO antimicrobials (ZnO, ZnO-SnO_2, ZnO-Ag_2O/Ag, and ZnO-CuO) and their composites to explore their potential applications in treating complex microbial-infected wounds. Addressing the global public health threat of antimicrobial resistance, as highlighted by the World Health Organization (WHO), is paramount. Numerous metals, especially in their "nanoparticle form", are increasingly employed for their antimicrobial properties, preventing adhesion, and treating microbial infections. The burgeoning demand for metal and MONPs stems from their physiochemical properties, making them invaluable in meeting diverse biomedical needs.

In our preceding investigation, we demonstrated the outstanding antimicrobial efficacy

of zinc oxide (ZnO) and its composite nanoparticles — (ZnO, ZnO-SnO_2, ZnO-Ag_2O/Ag, and ZnO-CuO) — against various microbes [1, 2]. These composite nanoparticles, particularly in combination with polymeric nanoparticles, exhibit significant potential in inhibiting microbial growth at wound sites. Notably, their antimicrobial prowess is evident even at a remarkably low dose of 0.010 μg mL^{-1} against Gram-positive/ Gram-negative bacteria and fungal strains.

Microscopic analysis through TEM images reveals the mesoporous nature of these nanoparticles, with a crystalline structure having a size below 10 nm in diameter. These MOs are synthesized through the solvothermal reduction method using $NaBH_4$. XRD confirms their crystallinity. Their antibacterial activity is dose and time-dependent, showcasing effectiveness against a broad spectrum of microbes. Hemocompatibility assessments indicate acceptable levels of haemolysis, with zinc oxide-copper oxide exhibiting the lowest haemolytic nature. Cytotoxicity evaluations using MTT assays in L929 and PC12 cell lines unveil differential compatibility, directing us towards potential applications in tissue regeneration for wound healing.

Scratch wound healing assays underscore the varied proliferative and migratory activities of MO nanocomposites, with zinc oxide-stannous oxide leading in both aspects. Evaluation through the chicken embryo membrane assay indicates angiogenic potential, with zinc oxide-copper oxide displaying the highest activity. Overall, the nanocomposites exhibit haemolytic activity, which may be attributed due to their low particle size, ensuring therapeutic concentrations below 10 μg mL^{-1}. This aligns with their antimicrobial efficacy, demonstrating superior cell compatibility with L929 compared to PC12 cells, thus affirming their migratory and proliferative nature. In conclusion, these MO nanocomposites present multifaceted attributes that hold promise for therapeutic applications in tissue regeneration.

3.3.2 INTRODUCTION

In the intricate tapestry of nanomaterials, MOs stand as versatile entities, offering a plethora of applications that extend far beyond traditional domains [3]. Among these, zinc oxide (ZnO), with its inherent biocompatibility and antimicrobial prowess, has emerged as a compelling candidate for various biomedical applications [4]. Expanding on this foundation, hybrid nanocomposites, such as ZnO-SnO_2, ZnO-Ag_2O/Ag, and ZnO-CuO, have ventured into the realm of innovative biomedical solutions, each bringing its unique set of properties to the forefront [2, 5].

This chapter explores the biological activities inherent in ZnO and its hybrid counterparts (ZnO-SnO_2, ZnO-Ag_2O/Ag, and ZnO-CuO). From the microcosm of antimicrobial efficacy to the macrocosm of biomedical wound healing applications, we navigate the diverse landscape of these MOs, seeking to unravel their potential impact on the intersection of materials science, biology, pharmaceutical science, and tissue engineering. The journey begins by delving into the intrinsic antimicrobial properties of ZnO [2], a characteristic that has captured the attention of researchers worldwide. As we navigate the intricate world of MOs, we encounter the amalgamation of ZnO with silver oxide (Ag_2O), copper oxide (CuO) and tin oxide (SnO_2) for different biomedical applications such as wound healing [6] and antimicrobial activity [1, 2]. These hybrid formations transcend the boundaries of their individual components, giving rise to synergistic effects and novel functionalities that hold promise in biomedical applications [1, 2].

As we embark on this exploration, it becomes evident that ZnO and its hybrid counterparts are not mere entities of material science but dynamic agents with the potential to revolutionize biomedical landscapes [7]. Through meticulous examination and synthesis of existing knowledge [1, 2], this chapter aims to provide a nuanced understanding of the biological activities exhibited by ZnO, ZnO-SnO_2, ZnO-Ag_2O/Ag, and ZnO-CuO. In

doing so, we pave the way for a deeper investigation of the transformative potential of these MOs, which hold an intricate activity in accelerating wound healing and regenerative nanomedicine.

3.3.3 EXPERIMENTAL

3.3.3.1 Synthesis of metal oxide composite nanoparticles

The methodology for synthesis of MONPs has been described in the experimental section of Chapter 2 (Page No. 63-65, Section 2.2.2).

3.3.3.2 Characterization and antibacterial activity evaluation

All synthesized MONPs have been characterized for their size using TEM, for porosity using BET analysis, for crystallinity using XRD and for antibacterial activity etc, all are published in our research group paper [1, 2]. Representative results of the NPs are provided in the results section.

3.3.3.3 Haemolysis

The investigation of haemolytic activity of MOs, specifically ZnO, ZnO-SnO_2, ZnO-Ag_2O/Ag, and ZnO-CuO, holds considerable significance within the context of healthcare. The methodology for haemolysis has been described in experimental section of Chapter 2 (Page No. 70-71, Section 2.5.1)

3.3.3.4 Biocompatibility Assay

The significance of conducting MTT (3-(4,5-dimethylthiazol-2-yl)-2,5-diphenyltetrazolium bromide) assay or biocompatibility/ cytocompatibility assays for MOs (ZnO, ZnO-SnO_2, ZnO-Ag_2O/Ag, and ZnO-CuO) in the context of wound healing and healthcare formulations is crucial to ensure the safety and efficacy of these materials in biological systems. The methodology for haemolysis has been described in experimental section of Chapter 2 (Page No. 67-68, Section 2.4.1)

3.3.3.5 Angiogenesis

Angiogenesis, the formation of new blood vessels from pre-existing ones [8], is a fundamental process in the human body crucial for various physiological and pathological conditions [9]. Among its many roles, angiogenesis plays a pivotal role in wound healing and regenerative medicine. This intricate process involves a series of tightly regulated events that contribute to tissue repair and regeneration. The methodology for haemolysis has been described in experimental section of Chapter 2 (Page No. 77-78, Section 2.8.1)

3.3.3.6 Scratch Wound Assay

The scratch wound assay have significant importance in the study of wound healing, offering a versatile and widely employed *in vitro* model. This assay allows for the investigation of various cellular processes associated with wound repair. The methodology for haemolysis has been described in experimental section of Chapter 2 (Page No. 69-70, Section 2.4.2)

3.3.4 RESULTS

3.3.4.1 Characterization and antibacterial activity evaluation

The ZnO, ZnO-CuO, ZnO-Ag_2O/Ag, and ZnO-SnO_2 NPs were synthesized through an *in situ* solvo-chemical reduction method using $NaBH_4$, as detailed in the experimental section. Some of characterizationas and activity of the above synthesized material have been evaluated by Dr. Monica Pandey, our research group members. The synthesis methods have been filed for patents and the preliminary work has been published earlier [1, 2]. The same materials have been used in this work to evaluate the biological properties under study. Their properties are as follows. The high-resolution transmission electron microscopy (HRTEM) micrographs of ZnO, ZnO-CuO, ZnO-Ag_2O/Ag, and ZnO-SnO_2 NPs are depicted in Figure 3.3.2 (a) to (d), respectively, demonstrating well-dispersed forms of all NPs.

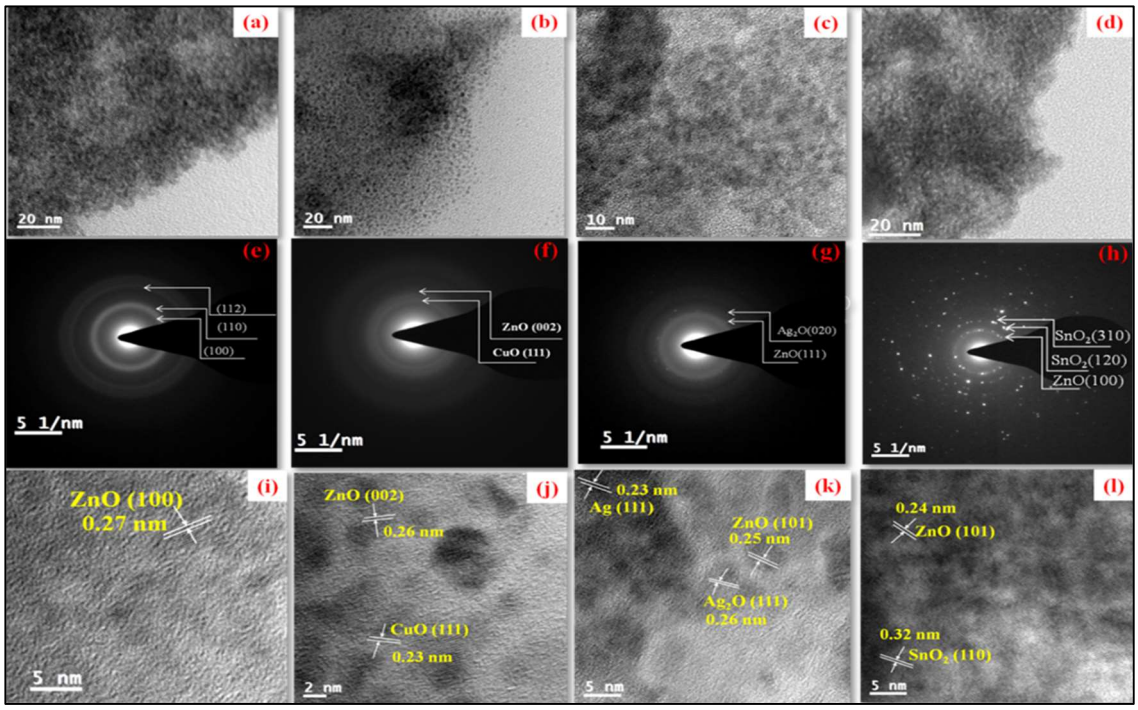

Figure 3.3.2: HR-TEM image of: (a) ZnO, (b) ZnO-CuO (c) ZnO-Ag_2O/Ag, (d) ZnO-SnO_2 NPs; SAED pattern for (e) ZnO, (f) ZnO-CuO, (g) ZnO-Ag_2O/Ag (h) ZnO-SnO_2 NPs and d-spacing for (i) ZnO, (j) ZnO-CuO, (k) ZnO-Ag_2O/Ag, (l) ZnO-SnO_2 [2]

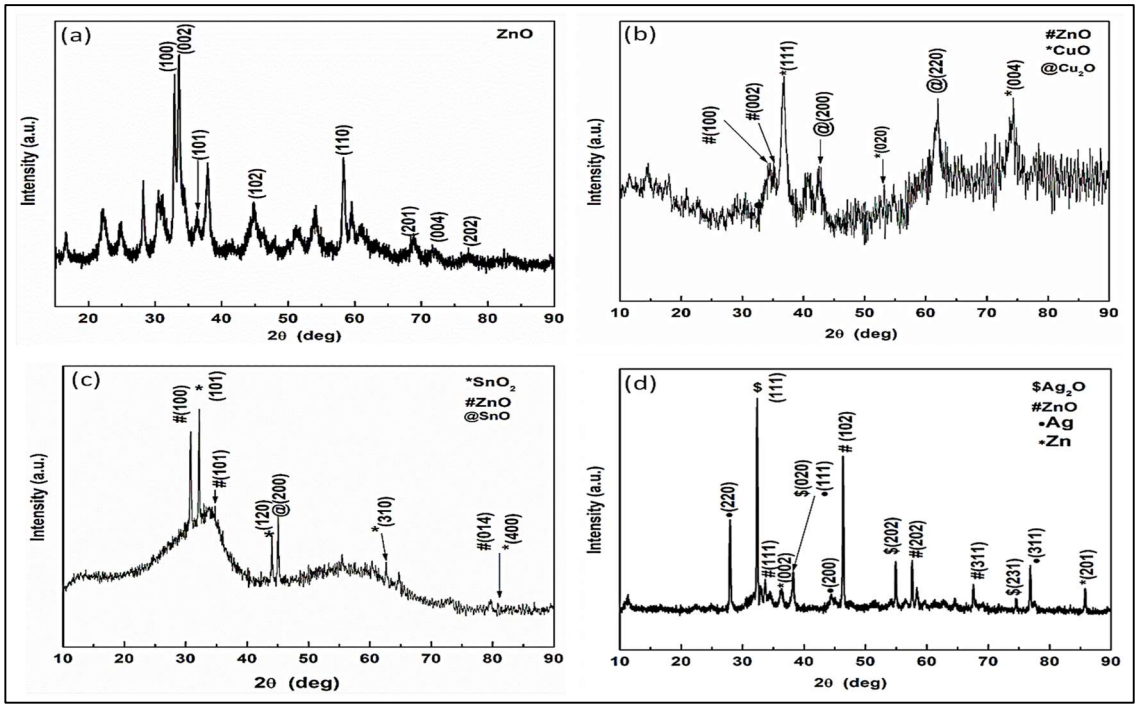

Figure 3.3.3: X-Ray diffraction pattern of (a) ZnO (b) ZnO-CuO (c) ZnO-SnO_2 (d) ZnO-Ag_2O/Ag NPs [2].

The HRTEM images in Figure 3.3.2 reveal the size and morphology of the NPs.

Specifically, ZnO NPs exhibit a quasi-spherical shape with an average diameter of approximately 2.25 ±0.3 nm. ZnO-CuO NPs (Figure 3.3.2b) display an average size of 2.1 ±0.2 nm, while the monodispersed ZnO-Ag_2O/Ag NPs (Figure 3.3.2c) have a diameter of 3.2 ±0.2 nm, and ZnO-SnO_2 NPs (Figure 3.3.2d) have a diameter of 5 ±0.2 nm. The selected area electron diffraction (SAED) patterns for ZnO, ZnO-CuO, ZnO-Ag_2O/Ag, and ZnO-SnO_2 are shown in Figure 3.3.2 (e), (f), (g), and (h), respectively.

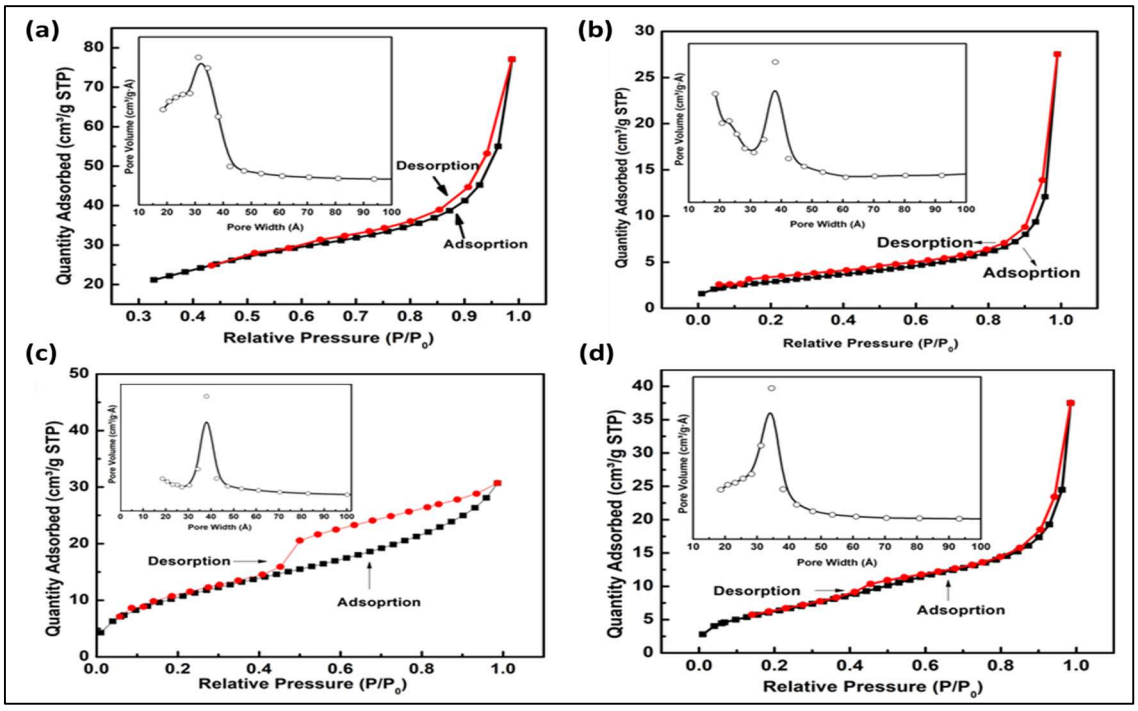

Figure 3.3.4: BET surface area of (a) ZnO, (b) ZnO-SnO_2 (c) ZnO-CuO and (d) ZnO-Ag_2O/Ag NPs [2].

The d-spacing values, obtained from HRTEM images, were calculated. For ZnO, a d-spacing of 0.27 nm corresponding to ZnO (100) was observed (Figure 3.3.2i), consistent with pure ZnO NPs. In the case of ZnO-CuO, the d-spacing values were calculated to be 0.23 nm for CuO (111) and 0.26 nm for ZnO (002) (Figure 3.3.2j). For ZnO-Ag_2O/Ag, the d-spacing of ~0.25 nm corresponds to ZnO (101), 0.23 nm for Ag (111), and 0.26 nm for Ag_2O (111) (Figure 3.3.2k). For ZnO-SnO_2, the d-spacing values are 0.24 nm for ZnO (102) and 0.32 nm for SnO_2 (110) (Figure 3.3.2*l*).The above results indicate the presence

of mixed oxide components in the samples, aligning well with the X-ray diffraction (XRD) findings discussed in the subsequent section. Further, the powder XRD patterns (Figure 3.3.3) were employed to scrutinize the solid-state crystal structure and phases of the synthesized MONPs. The XRD pattern of ZnO NPs (Figure 3.3.3a) aligns well with a prior report, corresponding to the hexagonal Wurtzite phase of ZnO NPs (JCPDS data card 89-0510). The discerned peaks at 2θ = 32.1°, 33.1°, 36.3°, 45.1°, 57.9°, 68.8°, 70.6°, and 77.1° correspond to the (100), (002), (101), (102), (110), (201), (004), and (202) diffraction planes, respectively.

The XRD pattern of ZnO-CuO NPs (Figure 3.3.3b) reveals diffraction peaks at 2θ ~34.4° and 34.9° corresponding to the (100) and (002) planes of ZnO Wurtzite hexagonal phase. Additionally, peaks at 2θ = 36.7°, 53.2°, and 74.3° are attributed to the (111), (020), and (004) planes, respectively, indicating the monoclinic crystalline phase of CuO (JCPDS file number 48-1548) [10]. A minor presence of cubic Cu_2O is evident in the composite system. Figure 3.3.3c displays the XRD pattern for ZnO-SnO_2, which concurs with a previous report [11]. Peaks at 2θ = 30.8° and 34.5° denote the hexagonal phase of ZnO with (100) and (101) diffraction planes, while peaks at 2θ = 32.1°, 42.7°, and 62.7° correspond to the tetragonal crystalline phase of SnO_2 with (101), (120), and (310) planes, respectively. Notably, the peak at 2θ = 80.17° indicates co-existing (400) planes of SnO_2 and (014) of ZnO, along with a trace amount of SnO (200).

Furthermore, Figure 3.3.3d illustrates the XRD peaks for ZnO-Ag_2O/Ag, revealing a cubic phase of ZnO and Ag_2O. The diffraction peaks at 2θ = 32.5°, 38.2°, 54.8°, and 74.5° correspond to the (111), (020), (202), and (231) diffraction planes of the cubic phase of Ag_2O. Peaks at 2θ ~33.5°, 56.3°, and 67.4° are characteristic of the cubic ZnO phase, representing the (111), (202), and (311) planes, respectively. The XRD confirms the presence of metallic Ag in the composite (ZnO-Ag_2O/Ag), with diffraction peaks at 2θ

~28°, 38.2°, 42.5°, and 77° corresponding to (220), (111), (200), and (311) diffraction planes, respectively.Additionally, the X-ray diffraction (XRD) analysis confirms the composition of the composite (ZnO-Ag_2O/Ag) with the presence of metallic Ag, as indicated by diffraction peaks at 2θ values of approximately 28°, 38.2°, 42.5°, and 77° corresponding to the (220), (111), (200), and (311) diffraction planes, respectively.

The above results unequivocally demonstrate the existence of significant diffraction peaks attributable to Ag_2O/Ag, SnO_2, and CuO in the final composition. It is noteworthy that no prominent diffraction peaks are observed, suggesting the absence of lattice site substitution of ZnO or other elements [12]. In conclusion, the XRD analysis establishes the presence of elemental Ag_2O/Ag, CuO, and SnO_2 in different combinations with ZnO, all exhibiting crystalline characteristics. These results align with TEM findings (fringes visible in Figure 3.3.2). In order to determine the physical characteristics such as surface area and porosity, we conducted BET surface area analysis for each of the samples. The calculated surface areas (Table 3.3.1) were 61.0 m^2/g, 40.1 m^2/g, 23.4 m^2/g, and 10.3 m^2/g for ZnO, ZnO-CuO, ZnO-Ag_2O/Ag, and ZnO-SnO_2 samples, respectively. All samples prepared for this study exhibited a porous nature, as evidenced by the BJH average pore size ranging from 3-4 nm for all samples, as shown in the inset of Figure 3.3.4.

Table 3.3.1: Samples and Corresponding BET Surface Areas

S. No.	Samples	BET surface area
1	ZnO	61 m^2/g
2	ZnO−CuO	40.1 m^2/g
3	ZnO−Ag_2O/Ag	23.4 m^2/g
4	ZnO−SnO_2	10.3m^2/g

The porous nature was further confirmed by the BJH isotherm (adsorption-desorption) of the type IV category (Figure 3.3.4), and the average pore size range indicated mesoporous characteristics, consistent with the porosity results obtained from HRTEM images. Observations revealed a decrease in specific surface area in mixed oxide NPs compared

to ZnO NPs, possibly attributed to the blocking of numerous micro-pores by the presence of small MONPs.

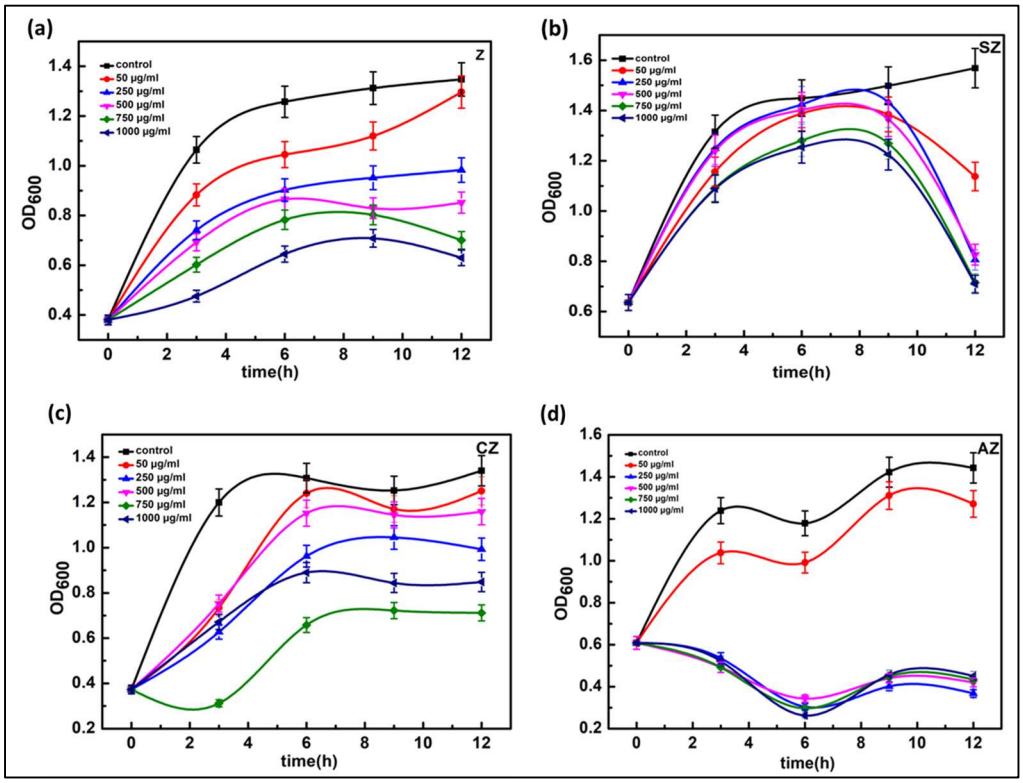

Figure 3.3.5: Antibacterial activity evaluation of (a) ZnO, (b) ZnO-SnO_2, (c) ZnO-CuO, (d) ZnO-AgO_2/Ag at different time interval with E. coli [2].

Additionally, the surface area of ZnO-CuO decreased with an increase in the average pore size. This phenomenon is linked to the inverse relationship between crystallinity/particle size and surface area, as indicated by the XRD pattern showing the amorphous nature of ZnO-CuO (Figure 3.3.3b) due to smaller particle size. It is noteworthy that the porous structure and particle size significantly influence antimicrobial properties, given the alterations in surface area and the availability of active interaction sites. Conclusively, the *in vitro* antimicrobial investigation was executed using E. coli, following the Kirby-Bauer method. The ODD values were computed at regular intervals of three hours for up to 12 hours for each set of samples and at various concentrations: 0 µg ml^{-1}, 50 µg ml^{-1}, 250 µg ml^{-1}, 500 µg ml^{-1}, 750 µg ml^{-1}, and 1000 µg ml^{-1}. Figure 3.3.5 illustrates the antibacterial

activity results of diverse NPs at different concentrations and time intervals. Across all NPs, a consistent trend emerged, revealing an augmentation in antibacterial activity or inhibition rate from 50 μg mL^{-1} to 1000 μg mL^{-1} after 3 h, yielding highly effective outcomes.

The antibacterial efficacy of ZnO operates through two mechanisms: (I) ROS generation and (ii) release/diffusion of Zinc ions [13]. Similarly, diverse antimicrobial mechanisms have been proposed for silver nanomaterials [14]. Ag NPs can infiltrate bacterial cell walls, inducing pits formation and releasing silver ions that impede microorganism growth. For CuO and SnO_2 NPs, antibacterial mechanisms have also been explored, emphasizing ions release and ROS formation, targeting vital cellular components to eliminate microorganisms [15, 16]. Further, metallic NPs exhibit the capability to hinder microorganism growth [17]. Accordingly, we can deduce that the current antibacterial materials adhere to the ROS mechanism. Notably, the combination of mixed bimetallic oxides with small metallic NPs (sized 2-3 nm) significantly enhances antimicrobial activities through a collaborative electrochemical mechanism, altering the band energy gap (Es) and subsequently promoting ROS formation [2].

3.3.4.2 Haemolysis

In the investigation of MONPs, haemolytic activity was systematically assessed across a range of concentrations from 1 to 10 μg mL^{-1}. The dose-dependent evaluation revealed varying degrees of haemolysis. The hemolytic outcomes observed in rat red blood cells represented in Figure 3.3.6 upon exposure to ZnO NPs were as follows: 1.21 ± 1.11, 1.51 ± 0.38, 1.67 ± 0.30, 2.30 ± 0.24, 2.49 ± 0.60, 2.74 ± 0.34, 3.04 ± 0.34, 3.36 ± 0.28, 3.90 ± 0.06, and 4.01 ± 0.34 at concentrations of 1, 2, 3, 4, 5, 6, 7, 8, 9, and 10 μg mL^{-1}, respectively.

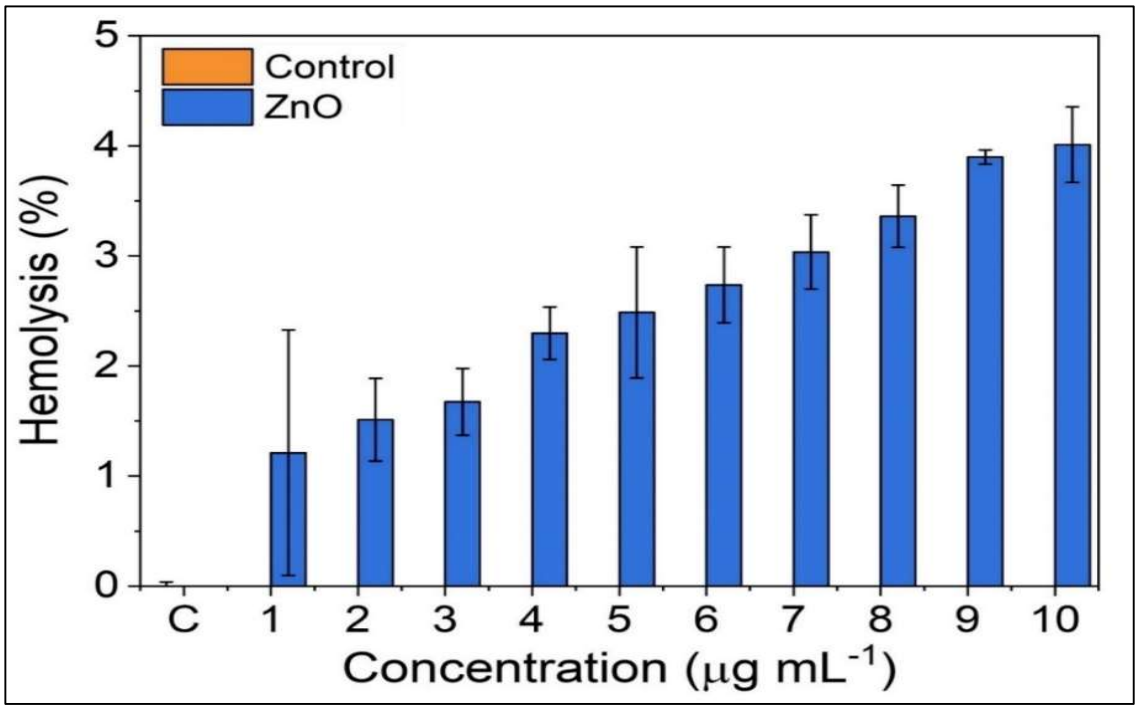

Figure 3.3.6: Haemolytic outcomes observed when rat RBCs treated with ZnO NPs.

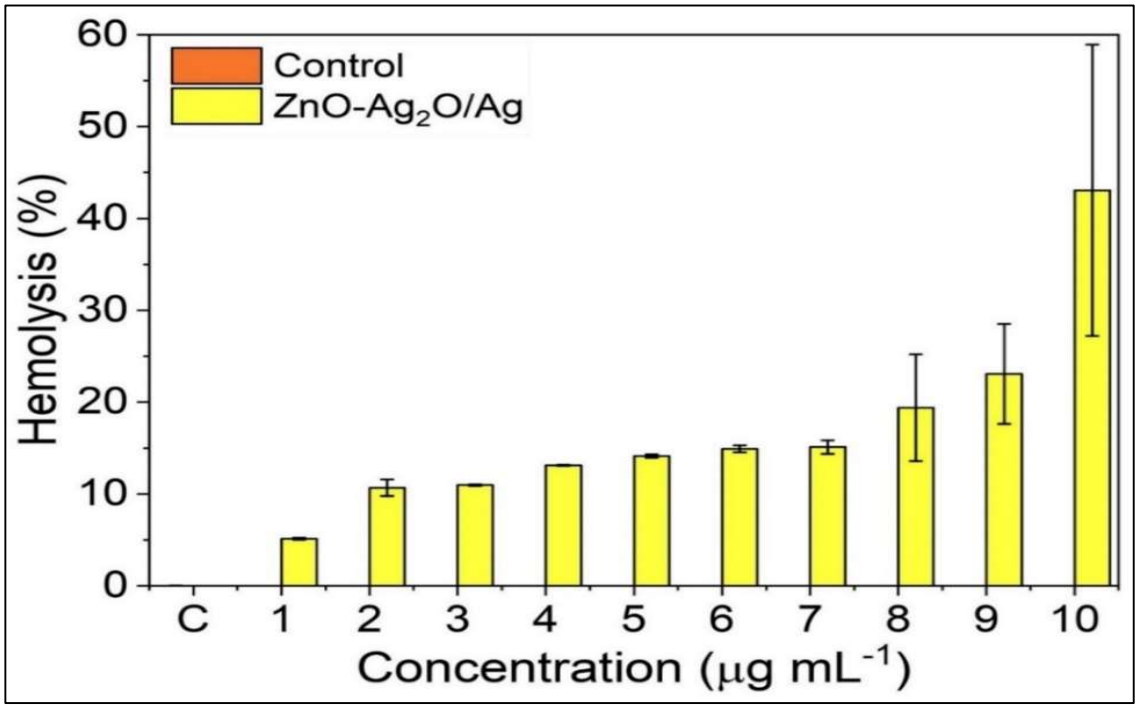

Figure 3.3.7: Haemolytic outcomes of ZnO-Ag_2O/Ag NPs when evaluated in rat RBCs at 37 ± 2 ℃.

The application of ZnO-Ag_2O/Ag NPs resulted in the following hemolytic outcomes (

Figure 3.3.7) when rat red blood cells (RBCs) were subjected to treatment for 24 hours at a concentrations of 1, 2, 3, 4, 5, 6, 7, 8, 9, and 10 µg mL^{-1}: 5.13 ± 0.10, 10.68 ± 0.89, 10.97 ± 0.09, 13.12 ± 0.07, 14.14 ± 0.18, 14.90 ± 0.38, 15.12 ± 0.74, 19.39 ± 5.81, 23.07 ± 5.44, and 43.07 ± 15.86, respectively. The results demonstrate a concentration-dependent increase in hemolytic activity of ZnO-Ag_2O/Ag NPs towards rat red blood cells (RBCs) after 24 hours of treatment.

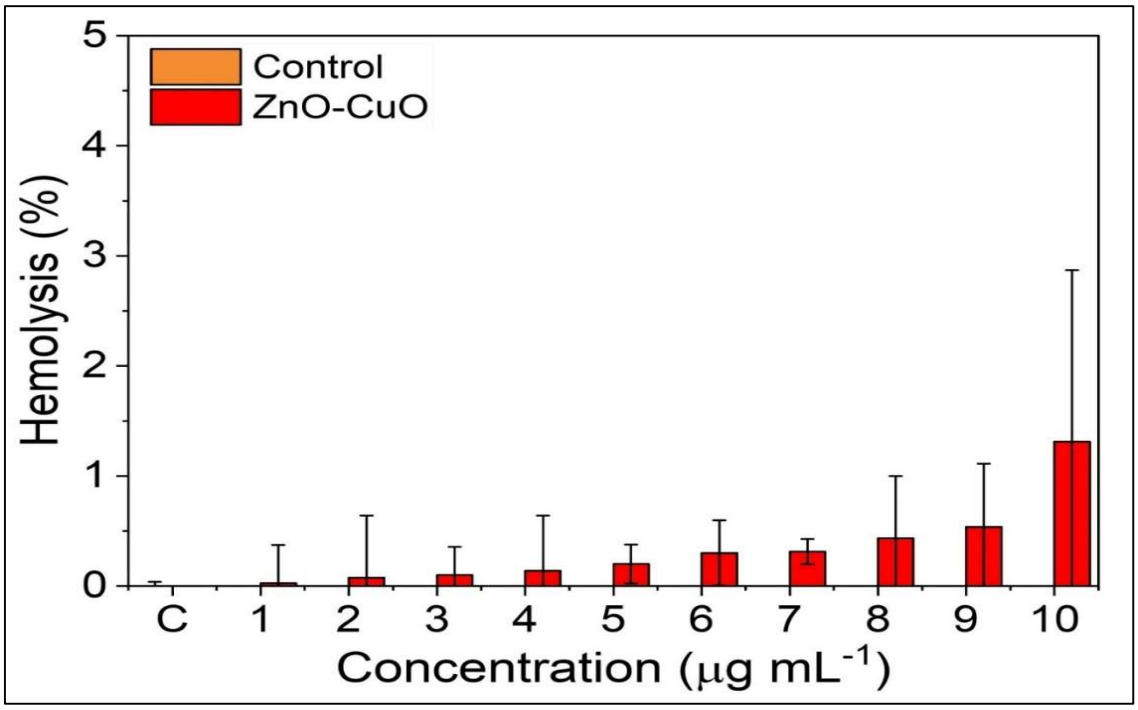

Figure 3.3.8: Haemolysis results of ZnO-CuO NPs interactions with rat RBCs

At lower concentrations (1-3 µg mL^{-1}), the hemolysis percentages were relatively low (5.13% - 10.97%). As the concentration increased (4-6 µg mL^{-1}), hemolysis showed a moderate rise (13.12% - 14.90%). A significant jump in hemolysis was observed at higher concentrations (7-10 µg mL^{-1}), reaching 15.12% at 7 µg mL^{-1} and exceeding 40% at 10 µg mL^{-1}. These findings suggest that ZnO-Ag_2O/Ag NPs possess dose-dependent cytotoxicity towards RBCs, potentially due to mechanisms like membrane disruption, reactive oxygen species (ROS) generation, or protein aggregation. Further investigations

are warranted to elucidate the specific mechanisms of hemolysis and assess the potential long-term effects of ZnO-Ag_2O/Ag NPs exposure on RBCs and overall health.

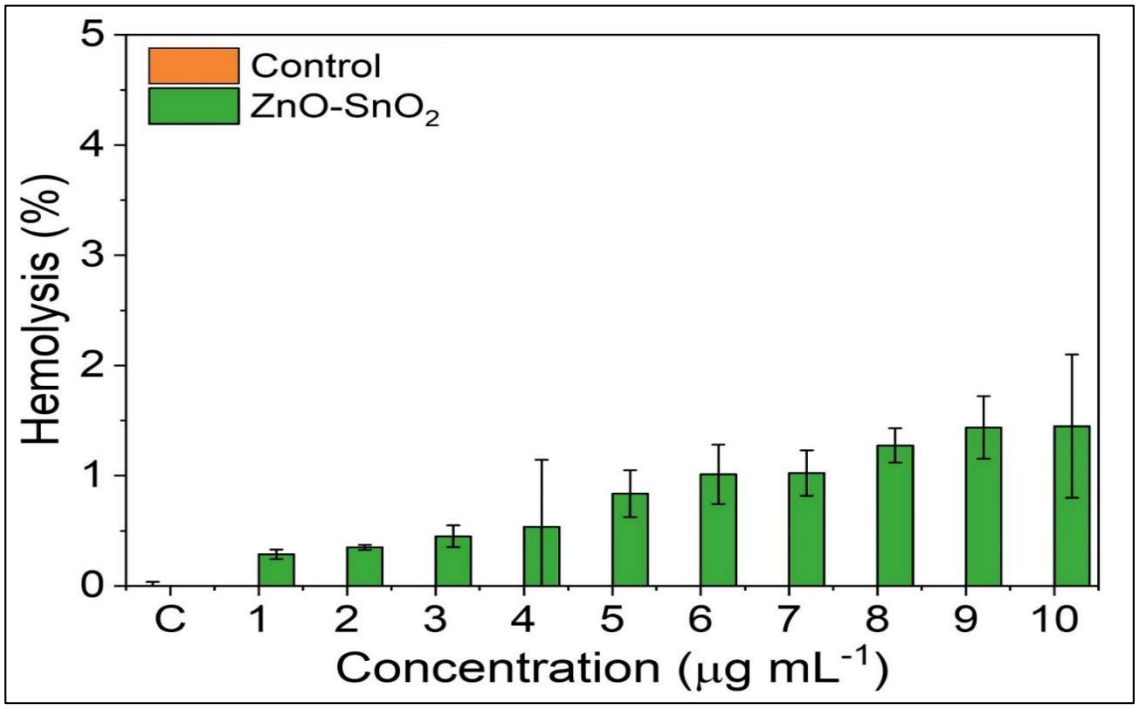

Figure 3.3.9: Haemolytic outcomes of ZnO-SnO_2 NPs in rat RBCs

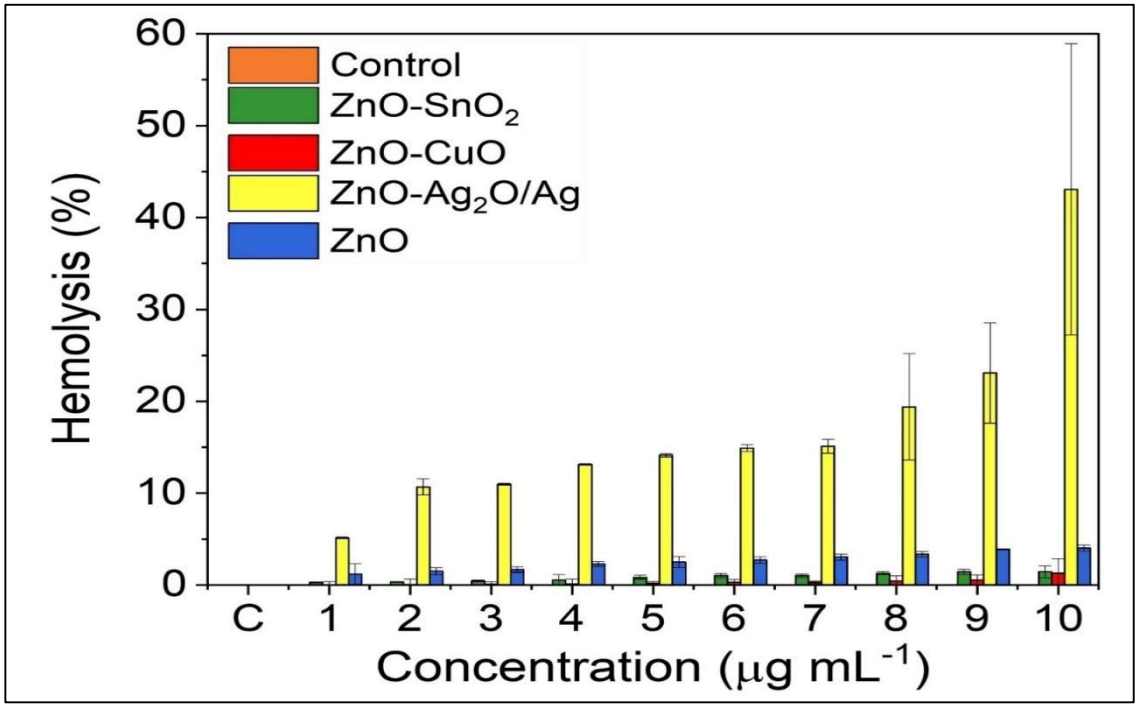

Figure 3.3.10: Comparative heamolytic activity of metal oxide NPs interacted with rat RBCs for 24 hours and 37°C.

The utilization of ZnO-CuO NPs led to the observed hemolytic effects (as illustrated in Figure 3.3.8) when rat red blood cells (RBCs) underwent a 24-hour treatment at concentrations ranging from 1 to 10 μg mL^{-1}. The resulting hemolysis values were as follows: 0.02 ± 0.35, 0.07 ± 0.57, 0.10 ± 0.26, 0.14 ± 0.50, 0.20 ± 0.18, 0.30 ± 0.30, 0.31 ± 0.11, 0.43 ± 0.56, 0.54 ± 0.57, and 1.31 ± 1.56, respectively. The application of ZnO-SnO_2 nanoparticles induced hemolytic effects, as depicted in Figure 3.3.9. Rat red blood cells (RBCs) subjected to a 24-hour treatment exhibited varying degrees of hemolysis at concentrations ranging from 1 to 10 μg mL^{-1}. The recorded hemolysis values were 0.29 ± 0.04, 0.35 ± 0.02, 0.45 ± 0.10, 0.54 ± 0.61, 0.84 ± 0.21, 1.01 ± 0.27, 1.02 ± 0.21, 1.27 ± 0.16, 1.44 ± 0.28, and 1.45 ± 0.65, respectively. This outcome underscores the dose-dependent nature of the hemolytic effects induced by ZnO-SnO_2 nanoparticles on RBCs.Notably, the extent of haemolysis exhibited an escalating trend with increasing MONP doses (Figure 3.3.10), yet in case of ZnO alone, ZnO-SnO_2 and ZnO-CuO it did not surpass 5% even at the highest tested dose when compared to the control. Statistical analysis revealed a non-significant difference (P>0.05) between the haemolytic activity of the above three treatment group and the negative control (PBS), emphasizing the biocompatibility of ZnO, ZnO-SnO_2 and ZnO-CuO NPs. Whereas, ZnO-Ag_2O/Ag shows significant haemolytic activity which is more than 5% at all the tested doses. These findings suggest that ZnO-Ag_2O/Ag NPs possess dose-dependent cytotoxicity towards RBCs, potentially due to mechanisms like membrane disruption, reactive oxygen species (ROS) generation, or protein aggregation. Further investigations are warranted to elucidate the specific mechanisms of hemolysis cuaed by ZnO-Ag_2O/Ag NPs.

3.3.4.3 Cell viability assay

Further, MTT assay was conducted to investigate the biocompatibility of MOs with biological system using L929 and PC12 cell lines. All MONPs (ZnO, ZnO-Ag_2O/Ag,

ZnO-CuO, ZnO-SnO_2) are biocompatible upto 10 µg mL^{-1}.

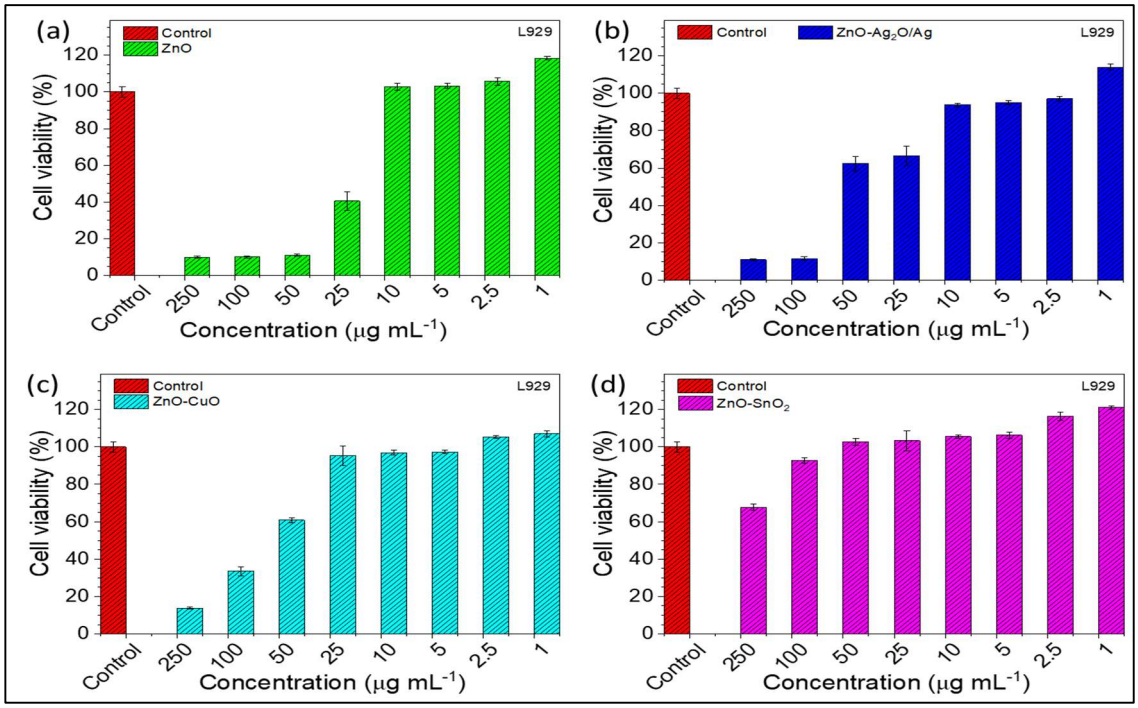

Figure 3.3.11: MTT assay of metal oxides in L929 cells. (a) ZnO, (b) ZnO-Ag_2O/Ag, (c) ZnO-CuO and ZnO-SnO_2.

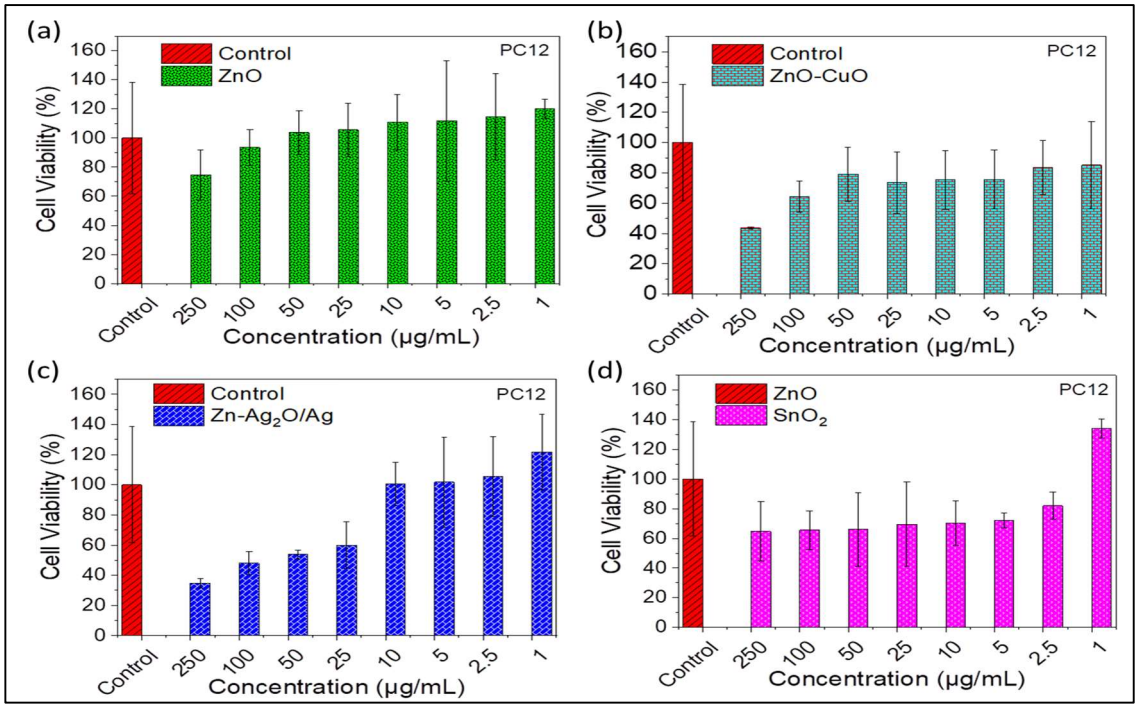

Figure 3.3.12: Cytocompatibility evaluation of metal oxide NPs in PC12 cell line. (a) ZnO, (b) ZnO-CuO, (c) ZnO-Ag_2O/Ag and (d) ZnO-SnO_2 are incubated in the concentrations range of 1-250 µg mL^{-1} with PC12 cell line.

At 10 µg mL^{-1}, cell viability was 102.77 ±2.04, 93.69 ±0.86, 96.96 ±1.35 and 105.56 ±0.97, respectively in L929 cell lines. MTT assay in L929 cells revels that among all tested MOs ZnO-SnO_2 is the most biocompatible. It reveals that approximately 100% viability of L929 cells are found at 25 µg mL^{-1}. ZnO NPs are showing toxicity at concentrations higher than 10 µg mL^{-1}, while other two MONPs are gradually following the ZnO NPs where at highest tested concentration all three MONPs (except ZnO-SnO_2) are showing common extant of viability of cells. The detailed information on viability of L929 cells in presence of different MONPs are illustrated in Figure 3.3.11.

To ascertain the potential modulatory effects of MOs on neurotrophic factors, cellular viability, proliferation, signalling cascades, migratory behaviour, and neuroprotective mechanisms during wound healing, an MTT assay was conducted utilizing PC12 cells as a model system. It was revealed that all MOs tested here are well and better tolerated by PC12 cells in comparison to L929 cells. ZnO which shows toxicity in L929 cells at 250 µg mL^{-1}, here it shows approximately 80% viable, while ZnO-SnO_2 which highly biocompatible in L929, here also shows constant viability. Other MOs (ZnO-CuO and ZnO-Ag_2O/Ag) have shown dose dependent effect on viability of PC12 cells. The detailed information of viability of PC12 cells in presence of different MONPs are illustrated in Figure 3.3.12.

In conclusion, the results of the MTT assay conducted on L929 and PC12 cell lines provide valuable insights into the biocompatibility of various MONPs. The findings indicate that all tested MOs, including ZnO, ZnO-Ag_2O/Ag, ZnO-CuO, and ZnO-SnO_2, exhibit biocompatibility up to the concentration of 10 µg mL^{-1} in L929 cells, with ZnO-SnO_2 demonstrating the highest biocompatibility among them. However, at higher concentrations, ZnO nanoparticles show toxicity in L929 cells, while ZnO-SnO_2 remains consistently biocompatible. Interestingly, in PC12 cells, all MOs are well-tolerated, with

$ZnO\text{-}SnO_2$ maintaining high biocompatibility.

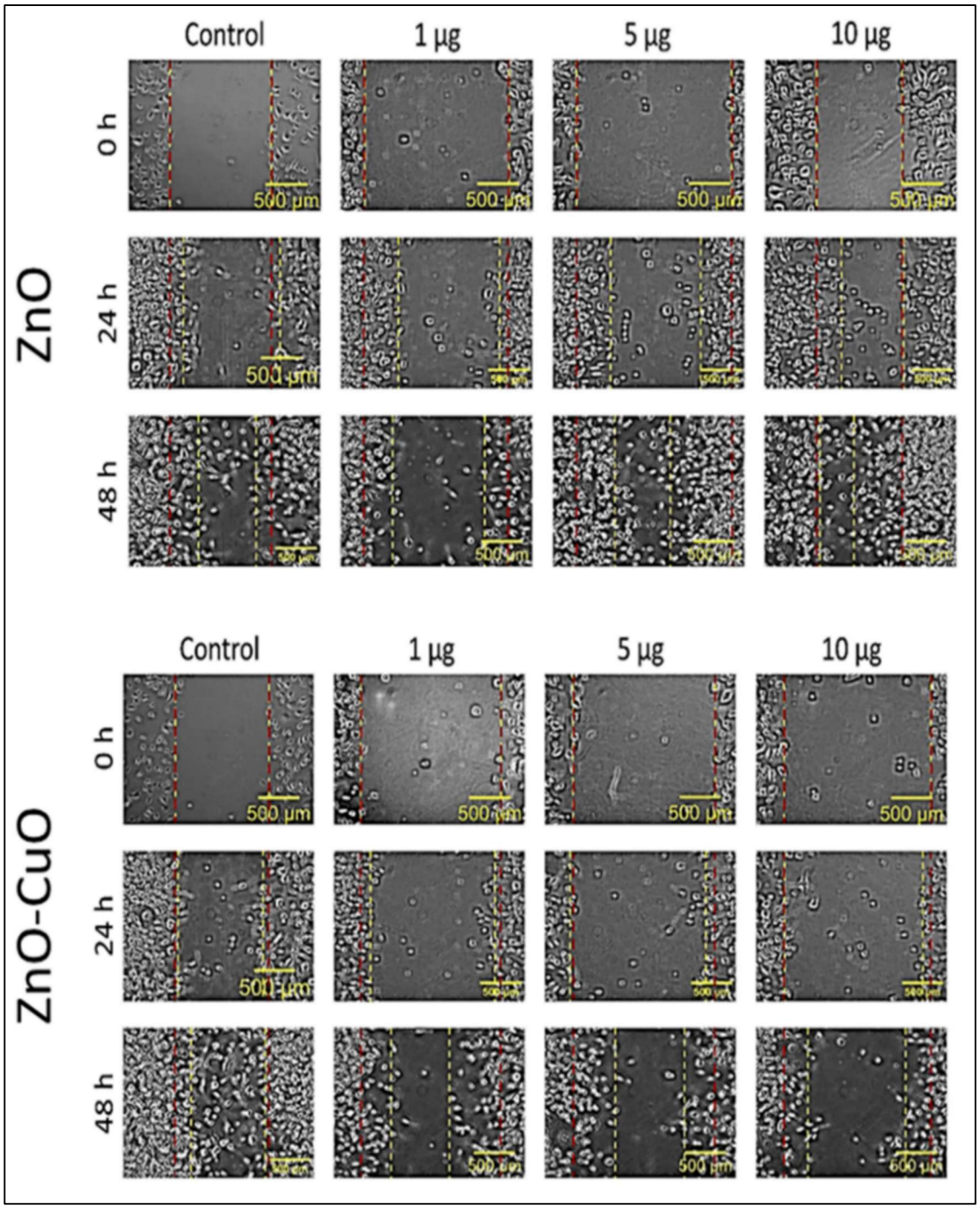

Figure 3.3.13: Scratch wound assay conducted on L929 cell line at different concentration of ZnO and ZnO-CuO.

These findings indicate that the biocompatibility of MONPs varies by cell line, highlighting the need to consider specific cellular contexts in their application. Further research is needed to understand the mechanisms behind cell-specific responses and

ensure safe use in biomedical applications like wound healing and regenerative medicine.

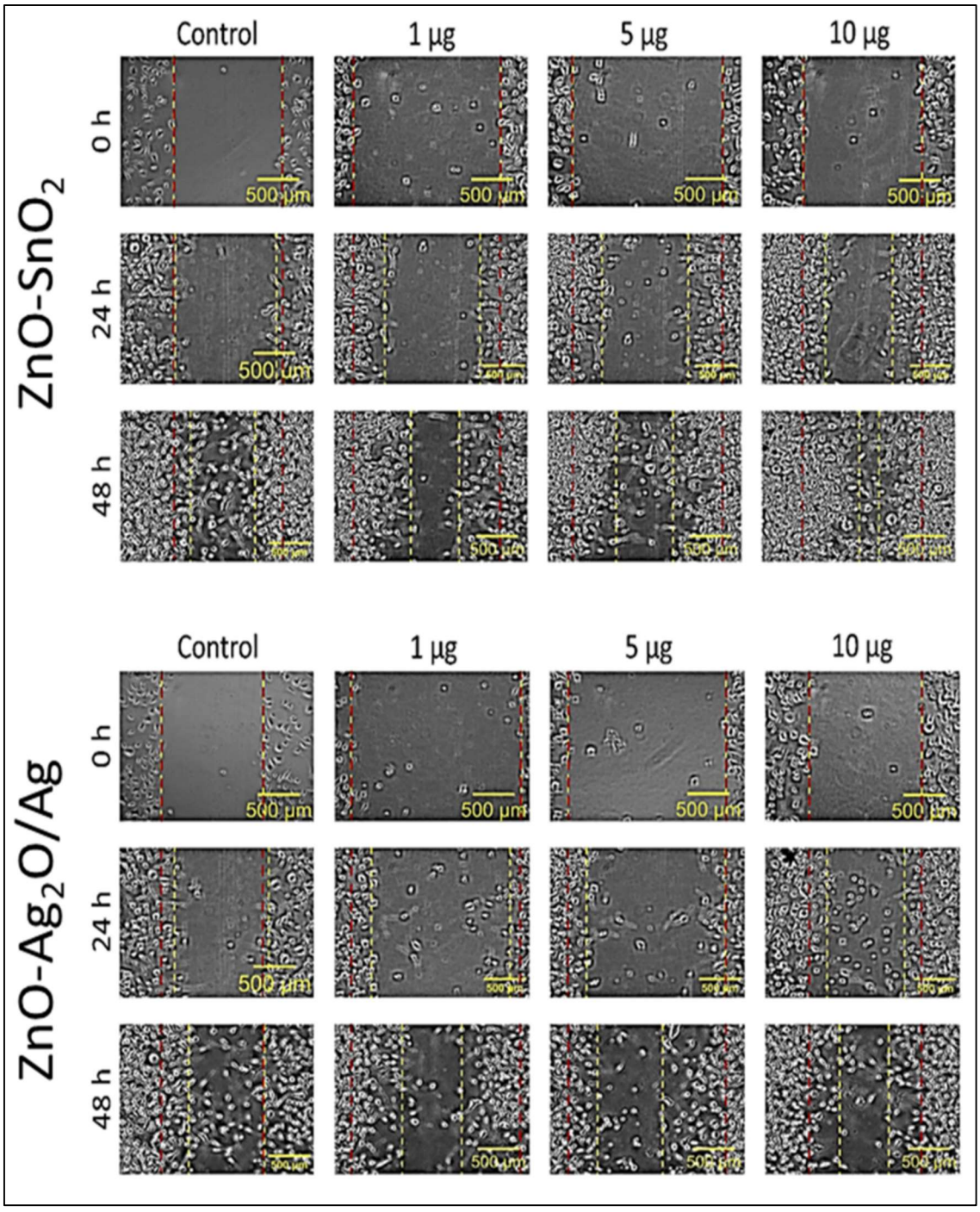

Figure 3.3.14: Scratch wound assay conducted on L929 cell line at different concentration of ZnO-SnO_2 and ZnO-Ag_2O/Ag.

3.3.4.4 Scratch wound assay

The scratch wound assay serves as a valuable and accessible tool in wound healing studies, offering a controlled platform for assessing cell migration, wound closure

dynamics, and the impact of various factors on the healing process. The versatility of scratch wound assay makes it a widely adopted method for investigating the cellular and molecular mechanisms underlying tissue repair.

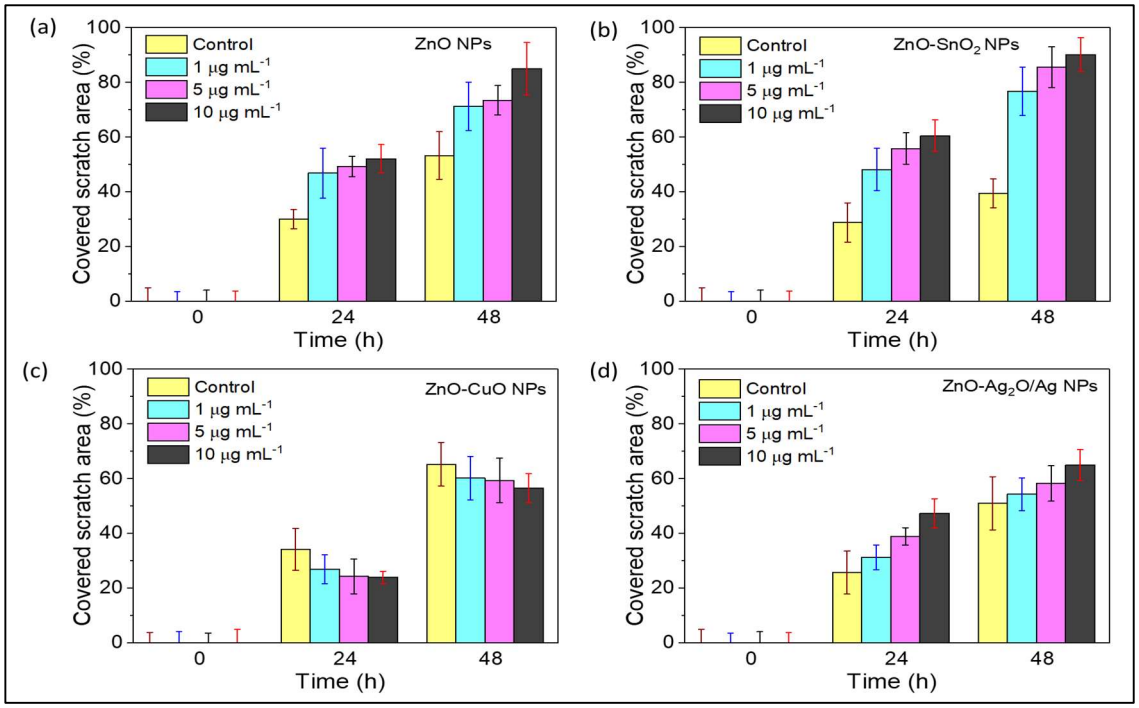

Figure 3.3.15: Scratch wound assay conducted in L929 cell lines by incubating metal oxides for 48 h. (a) ZnO, (b) ZnO- SnO_2, (c) ZnO-CuO and (d) ZnO- Ag_2O/Ag

In this study, the versatility of the scratch wound assay was harnessed to assess the wound closure dynamics in response to different concentrations of ZnO, ZnO-SnO_2, ZnO-CuO, and ZnO-Ag_2O/Ag MOs on the L929 cell line. The outcomes of assay have been captured in images and illustrated in Figure 3.3.13 and in Figure 3.3.14 along with the quantitative data are reported in Table 3.3.2. and the graphical representation in Figure 3.3.15 which are obtained in terms of covered scratch area (%) after incubation with MONPs. These results provide insight into the dose-dependent effects of the MONPs on cell migration and proliferation.

ZnO, ZnO-SnO_2 and ZnO-Ag_2O/Ag exhibited a clear dose-dependent impact, where an increase in concentration resulted in enhanced cell coverage of the scratched area (Figure 3.3.15). However, the study revealed intriguing findings regarding ZnO-CuO

nanoparticles. Contrary to expectations, these nanoparticles did not inhibit cell migration and proliferation, but their influence was weaker compared to the control cells. The most significant migratory and proliferative activity was observed in ZnO-SnO_2 nanoparticles, emphasizing their potential in promoting wound healing processes.

Table 3.3.2: Average scratch cover area (%) by L929 cell lines after incubation with metal oxide NPs at different concentrations for 48 h.

MONPs	Time (h)	(Control) 0	Concentration of MONPs (µg mL^{-1}) 1	5	10
ZnO	0	0.00 ±5.00	0.00 ±3.60	0.00 ±4.10	0.00 ±3.80
	24	30.02 ±3.48	46.84 ±9.14	49.28 ±3.72	52.10 ±5.19
	48	53.30 ±8.64	71.19 ±8.84	73.46 ±5.35	84.95 ±9.55
ZnO-CuO	0	0.00 ±3.80	0.00 ±4.10	0.00 ±3.60	0.00 ±5.00
	24	34.16 ±7.66	26.90 ±5.27	24.27 ±6.34	23.92 ±2.26
	48	65.26 ±8.01	60.17 ±7.90	59.33 ±8.14	56.49 ±5.28
ZnO-SnO_2	0	0.00 ±5.00	0.00 ±3.60	0.00 ±4.10	0.00 ±3.80
	24	28.81 ±7.20	48.11 ±7.77	55.85 ±5.70	60.51 ±5.76
	48	39.50 ±5.24	76.77 ±8.82	85.56 ±7.51	90.12 ±6.16
ZnO-Ag_2O/Ag	0	0.00 ±5.00	0.00 ±3.60	0.00 ±4.10	0.00 ±3.80
	24	25.72 ±7.90	31.21 ±4.52	38.93 ±3.18	47.35 ±5.31
	48	51.03 ±9.72	54.29 ±6.00	58.22 ±6.46	64.92 ±5.71

Scratch wound treated at a concentration of 10 µg mL^{-1} with ZnO alone and ZnO-SnO_2 is only able to cover 80-90% of scratch wound area, while ZnO-CuO is not able to cover more scratch wound area in comparison to control sample, however, ZnO-Ag_2O/Ag have better migratory and proliferative effect as it is able to cover approximately 65% of scratch area within 48 hours of post treatment (Table 3.3.2). The detailed information on scratch wound cover in presence of different MONPs are recorded in Table 3.3.2. The migratory potential of MO are varied in the order of ZnO- SnO_2>ZnO>ZnO-Ag_2O/Ag>ZnO-CuO (Figure 3.3.15). It also can be concluded that non of the MO have strong proliferative activity as non of them can able to cover the 100% scratch area even after 48 h of treatment with incubation of maximum safe concentration of MONPs (10 µg mL^{-1}). In conclusion, this scratch wound assay demonstrates the efficacy in evaluating the wound closure dynamics induced by various MONPs. The dose-dependent effects

observed with ZnO, ZnO-SnO_2, and ZnO-Ag_2O/Ag suggest their potential in influencing cell migration and proliferation. Notably, ZnO-CuO nanoparticles did not inhibit cell activities but exhibited weaker effects compared to the control. The order of migratory potential among the tested MOs was found to be ZnO-SnO_2 > ZnO > ZnO-Ag_2O/Ag > ZnO-CuO. Importantly, none of the tested MONPs displayed strong proliferative activity, as none achieved complete coverage of the scratch area even at the maximum safe concentration of 10 µg mL^{-1} after 48 h of treatment. These findings highlight the potential of MONPs in wound healing and emphasize the importance of selecting specific compositions for optimal therapeutic effects.

3.3.4.5 Angiogenesis (CAM assay)

Angiogenesis assays play a critical role in wound healing by providing a comprehensive assessment of vascularization processes. CAM assay offer valuable insights into the molecular and cellular events that contribute to the formation of new blood vessels, influencing tissue perfusion and overall wound healing outcomes.

Table 3.3.3: Angiogenic outcome of ZnO NPs

Angiogenesis Parameter	Time (h)	Control	ZnO NPs Dose (µg)		
		0	1	5	10
Explant area (%)	0	100.00±00.03	100.00±00.02	100.00±00.00	100.00±0.00
	2	122.87±00.09	119.18±00.00	106.71±00.00	96.37 ±0.01
	4	131.03±13.17	130.27±00.01	124.01±00.02	117.30±0.01
	8	146.17±00.05	136.16±00.00	140.47±00.02	119.83±0.04
Vessels area (%)	0	100.00±17.27	100.00±01.52	100.00±05.61	100.00±6.38
	2	117.53±21.33	105.69±02.56	112.19±10.59	92.85 ±5.76
	4	131.45±35.58	116.73±01.25	113.23±06.60	126.48±9.48
	8	152.31±19.16	120.31±02.16	127.32±07.59	115.72±8.83

All MONPs were evaluated for their angiogenic potential using the CAM assay, with outcomes shown in Figure 3.3.16. The CAM assay of ZnO NPs indicated that ZnO particles do not induce angiogenesis *in vivo* (*in ovo*). Neither the explant area nor the blood vessel area increased with different doses of ZnO NPs. In fact, as the dose of ZnO

NPs increased, both the total explant and vessel areas tended to decrease. Results are reported inTable 3.3.3. Figure 3.3. 17 shows that ZnO-Ag2O/Ag NPs do induce angiogenesis *in vivo* (*in ovo*).

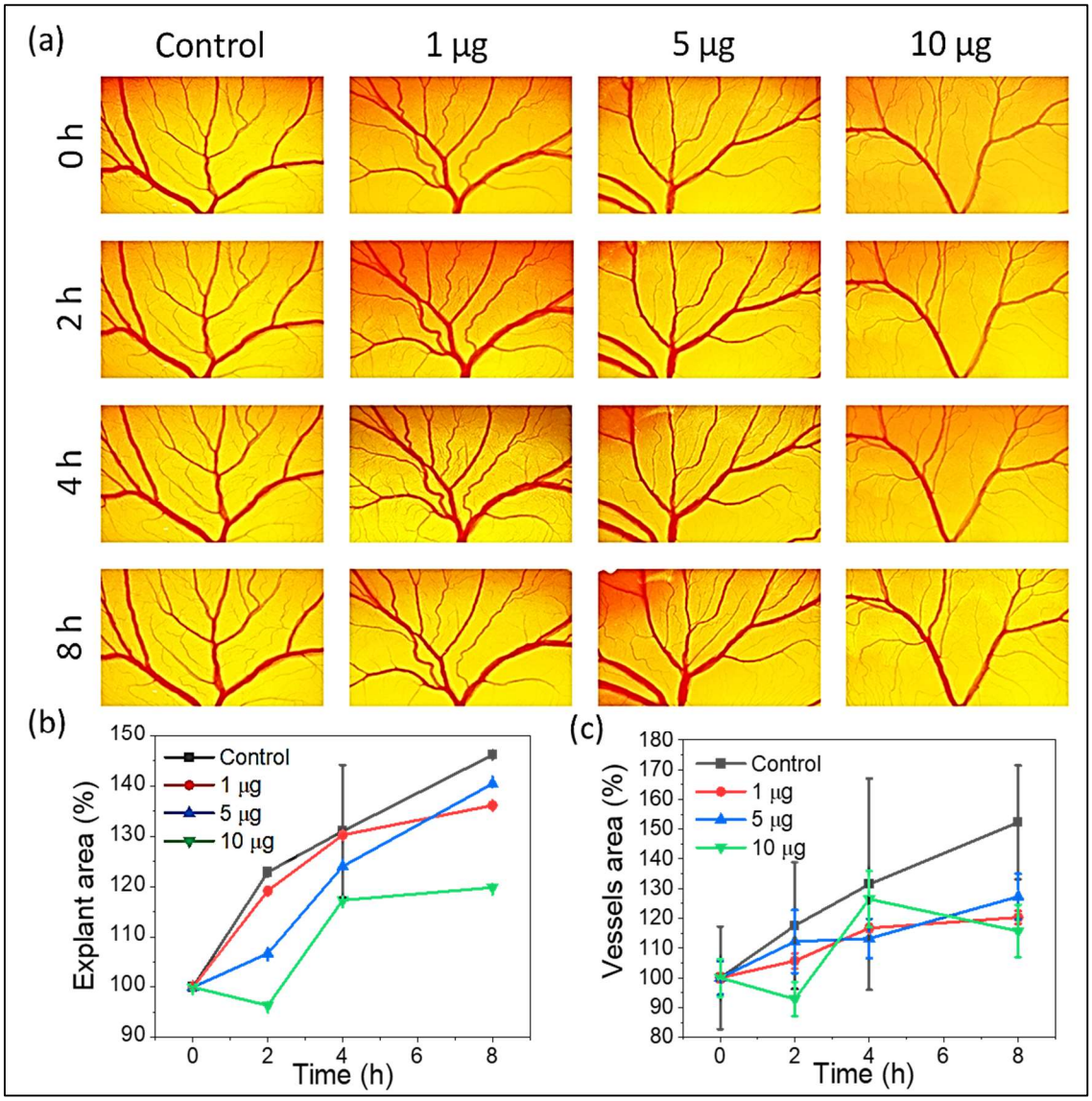

Figure 3.3.16: Angiogenic effect of ZnO NPs. (a) Photographic images of CAM at different time points, assessment of angiogenic parameter (b) explant area and (c) vessels area.

Furher, it can also be concluded that the explant area has increased approximately 1.5 fold in comaparison to control at a 5 µg dose of ZnO-Ag_2O/Ag NPs, while low dose (1 µg) does not significantly engance the explant and vessels area, on the other hand high dose (10 µg) gives a mixed and complex result, showing angiogenic trend (Figure 3.3. 17).

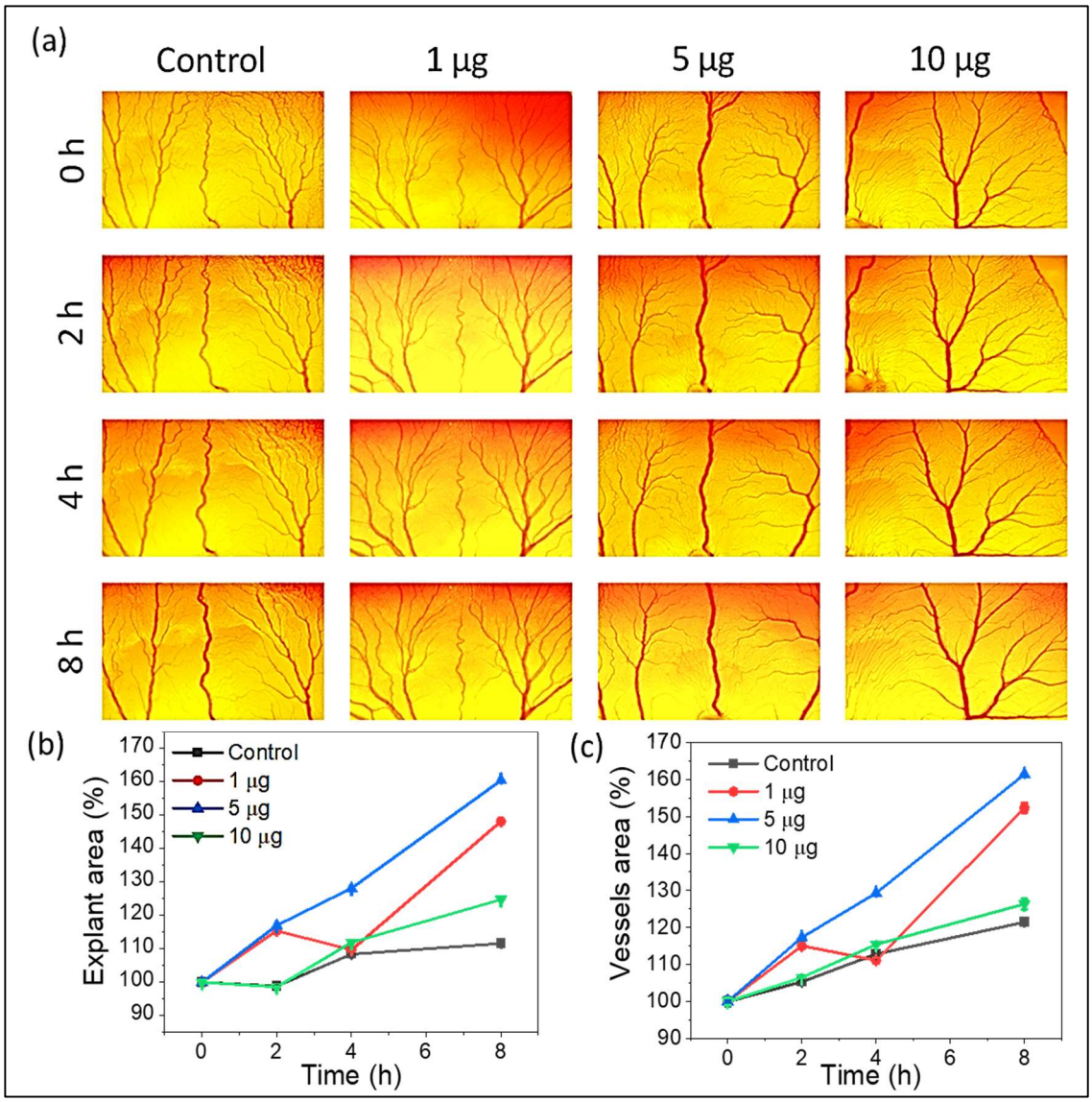

Figure 3.3. 17: Angiogenic effect of ZnO-Ag_2O/Ag NPs. (a) Photographic images of CAM at different time points, assessment of angiogenic parameter (b) explant area and (c) vessels area.

Table 3.3.4: Angiogenic outcome of ZnO-Ag_2O/Ag NPs.

Angiogenesis Parameter	Time (h)	Control 0	ZnO-Ag_2O/Ag NPs Dose (µg) 1	5	10
Explant area (%)	0	100.00±0.00	100.00±0.00	100.00±0.00	100.00±0.00
	2	98.85±0.00	115.45±0.00	117.02±0.00	98.64±0.00
	4	108.42±0.00	109.66±0.00	128.16±0.00	111.92±0.00
	8	111.63±0.00	148.21±0.00	160.45±0.01	124.78±0.00
Vessels area (%)	0	100.00±1.24	100.00±0.23	100.00±0.30	100.00±0.98
	2	105.30±0.39	115.04±0.60	117.33±0.08	106.47±0.06
	4	112.84±0.40	111.13±0.68	129.30±0.25	115.42±0.17
	8	121.43±0.08	152.32±1.35	161.36±0.23	126.33±1.48

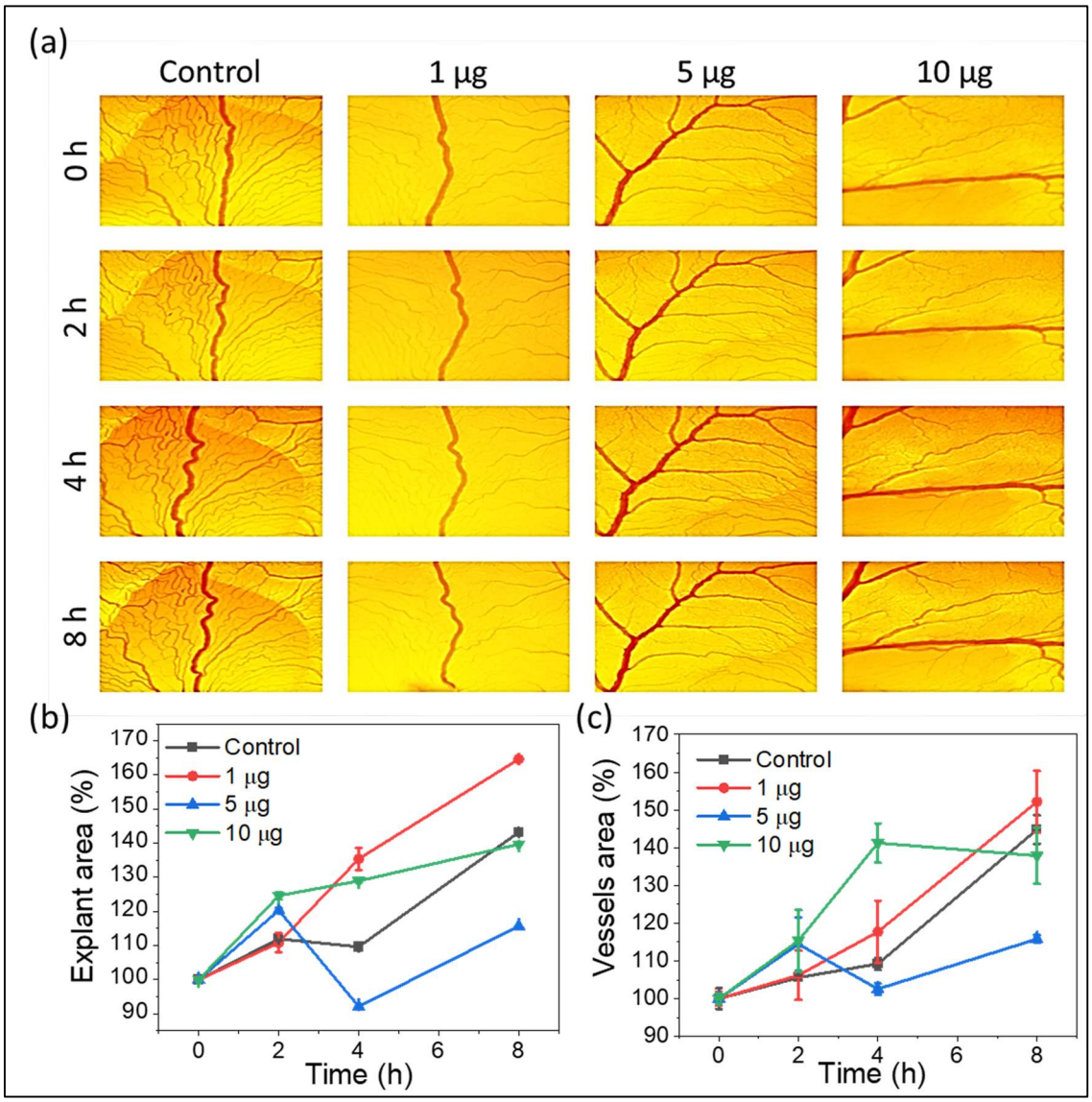

Figure 3.3.18: Angiogenic effect of ZnO-CuO NPs. (a) Photographic images of CAM at different time points, assessment of angiogenic parameter (b) explant area and (c) vessels area.

Table 3.3.5: Angiogenic outcome of ZnO-CuO NPs.

Angiogenesis Parameter	Time (h)	Control	ZnO-CuO NPs Dose (µg)		
		0	1	5	10
Explant area (%)	0	100.00±0.15	100.00±0.02	100.00±0.08	100.00±0.21
	2	111.96±0.43	110.84±2.78	120.31±0.64	124.61±1.08
	4	109.62±0.55	135.37±3.24	92.17±0.04	128.92±0.44
	8	143.18±0.19	164.61±0.82	115.71±0.11	139.68±0.10
Vessels area (%)	0	100.00±2.75	100.00±1.80	100.00±1.19	100.00±1.36
	2	105.58±0.67	106.20±6.54	114.42±7.08	115.38±8.09
	4	109.22±1.59	117.73±8.21	102.56±1.53	141.23±5.18
	8	144.79±3.79	152.14±8.18	115.80±0.98	137.85±7.50

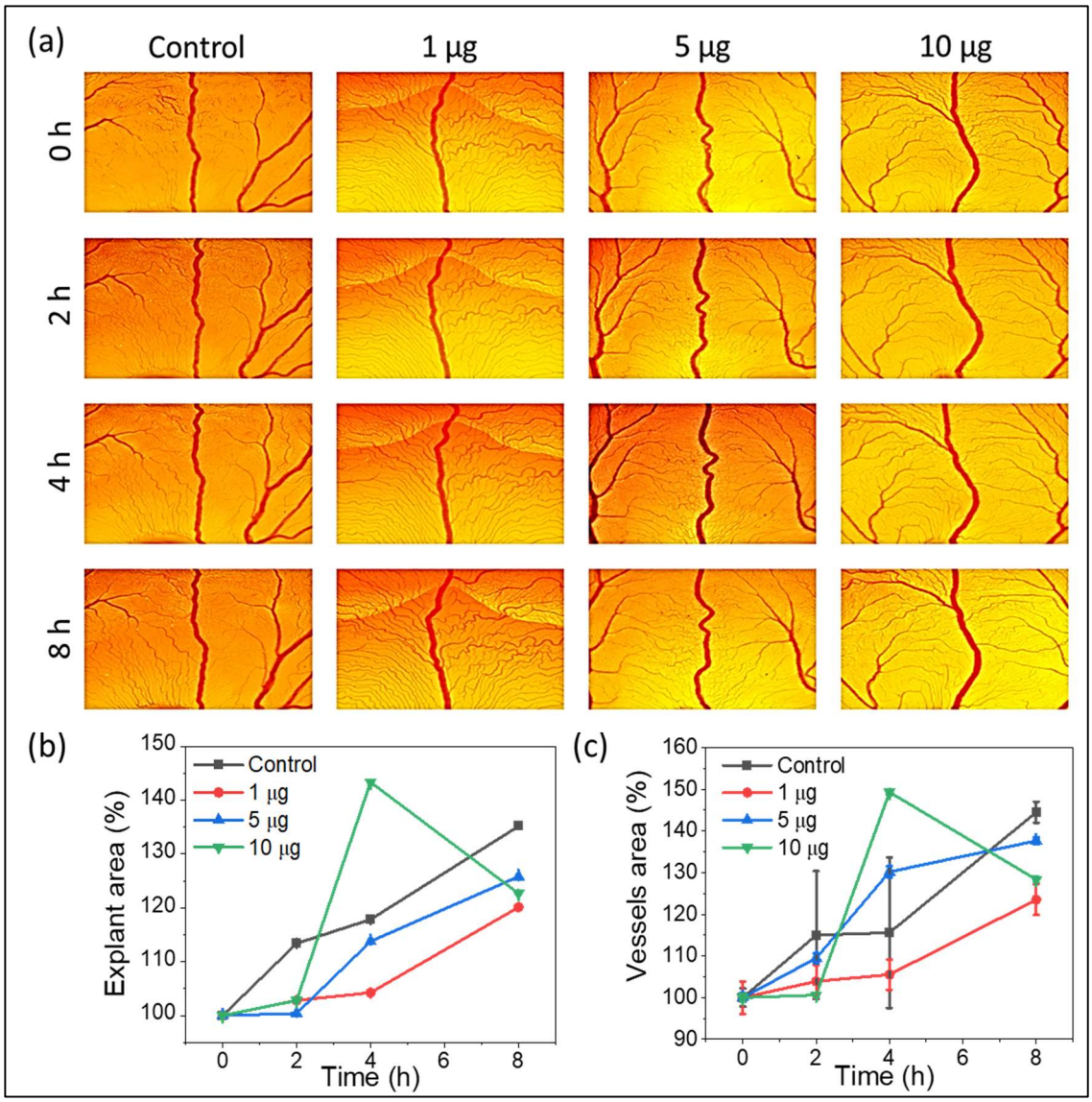

Figure 3.3. 19: Angiogenic effect of ZnO-SnO_2 NPs. (a) Photographic images of CAM at different time points, assessment of angiogenic parameter (b) explant area and (c) vessels area.

Table 3.3.6: Angiogenic outcome of ZnO-SnO_2 NPs.

Angiogenesis Parameter	Time (h)	Control	ZnO-SnO_2 NPs Dose (µg)		
		0	1	5	10
Explant area (%)	0	100.00±0.01	100.00±0.01	100.00±0.01	100.00±0.02
	2	113.41±0.02	102.82±0.00	100.41±0.02	102.81±0.02
	4	117.85±0.00	104.26±0.01	113.78±0.01	143.36±0.00
	8	135.16±0.00	120.12±0.00	125.82±0.00	122.69±0.05
Vessels area (%)	0	100.00±2.19	100.00±3.88	100.00±1.02	100.00±0.95
	2	114.98±15.35	103.90±3.89	109.48±1.20	100.63±0.51
	4	115.59±18.04	105.53±3.63	130.18±1.35	149.29±0.72
	8	144.48±2.51	123.52±3.73	137.63±0.83	128.35±0.70

Further, the detail on the angiogenic potential parameters outcome has been reported in Table 3.3.4. CAM assay of ZnO-CuO NPs revealed that these nanoparticles are angiogenic in nature at low dose (1 µg) *in vivo (in ovo)* condition because at only low dose explant area in increased while at higher dose complex results of explant area measurement are found, while low as well as high dose of ZnO-CuO NPs can able to produce higher blood vessels area (Figure 3.3. 17). Further, the detailed outcome of angiogenesis has been outlined in Table 3.3.5.

CAM assay of ZnO-SnO_2 NPs revealed that these nanoparticles have a complex action on angiogenesis. As low dose (1 µg and 5 µg) are not able to increase explant area, while only high dose of ZnO-SnO_2 is only able to induce angiogenic effect at the end of 2 hour of incubation but this effct also demised when readings are takin at 8 h.in case of vessels area development complex resuts are seen. To concludes the effect of ZnO-SnO_2 on angiogenesis, more animal modes are required and deep study with more time points and more doses are required. The detailed outcome of angiogenesis has been reported in Table 3.3.6

The effect of MOs on angiogenesis was assessed using chicken embryo angiogenesis assay. The results reveal that ZnO-Ag_2O/Ag and ZnO-CuO have some angiogenic effect as they have larger the explant area and vessels area in comparison to control (reference) while ZnO alone does not having inducing effect, however ZnO-SnO_2 shows a complex behaviour on angiogenesis.

3.3.5 DISCUSSION

The study comprehensively investigated the effects of various MONPs on biological activity. In haemolytic activity evaluation, MONPs were systematically evaluated in the concentration range of 1 to 10 µg mL^{-1}. ZnO, ZnO-SnO_2, and ZnO-CuO NPs displayed

minimal haemolysis, less than 5% even at the highest tested dose, emphasizing their biocompatibility. In contrast, ZnO-Ag_2O/Ag showed significant haemolytic activity above 5% at all tested doses.

In MTT assay on L929 cells, ZnO-SnO_2 demonstrated remarkable biocompatibility with almost 100% cell viability at 250 μg mL^{-1}. In contrast, ZnO alone displayed toxicity above 10 μg mL^{-1}, while ZnO-CuO and ZnO-Ag_2O/Ag displayed similar toxicity trends. MTT assays on PC12 cells revealed a surprising tolerance of all tested MOs compared to L929 cells. ZnO, which is toxic at 250 μg mL^{-1} in L929 cells, here, exhibits about 80% viability. ZnO-SnO_2 is highly biocompatible in L929 cells, exhibits sustained effects on PC12 cell viability. ZnO-CuO and ZnO-Ag_2O/Ag displayed dose-dependent effects.

In the scratch wound test, none of the MOs completely covered the wound area within the safe concentration range (1–10 μg mL^{-1}) of MOs even after 48 hours. ZnO and ZnO-SnO_2 covered 80–90% at 10 μg mL^{-1}, while ZnO-CuO covered less than 10%. In particular, ZnO-Ag_2O/Ag exhibited migratory and diffusion effects, covering more than 50% within 48 hours.

Transitioning to angiogenesis assay, ZnO-Ag_2O/Ag and ZnO-CuO demonstrated angiogenic effects, leading to larger explants and vessel areas compared to the control. In contrast, ZnO alone did not induce angiogenesis, and ZnO-SnO_2 displayed a complex behaviour in this context.

3.3.6 CONCLUSIONS

Our study reveals diverse effects of MONPs on wound healing processes spanning haemolytic activity, cellular viability, wound closure dynamics, and angiogenesis. These findings provide important insights into MONPs biocompatibility and potential therapeutic applications in wound healing. The results underline the importance of considering specific nanoparticle characteristics, concentrations, and cell types. The

observed differential responses emphasize the need for a nuanced understanding of the interactions of MONPs with biological systems. Further investigation of the underlying mechanisms may provide insight into safe biomedical applications of these materials.

3.3.7 REFERENCES

1. Pandey, M., et al., *Targeted specific inhibition of bacterial and Candida species by mesoporous Ag/Sn–SnO2 composite nanoparticles: in silico and in vitro investigation.* RSC Advances, 2022. **12**(2): p. 1105-1120. DOI: 10.1039/D1RA07594B.

2. Pandey, M., et al., *Targeted and Enhanced Antimicrobial Inhibition of Mesoporous ZnO–Ag2O/Ag, ZnO–CuO, and ZnO–SnO2 Composite Nanoparticles.* ACS Omega, 2021. **6**(47): p. 31615-31631. DOI: 10.1021/acsomega.1c04139.

3. Andreescu, S., et al., *Biomedical Applications of Metal Oxide Nanoparticles*, in *Fine Particles in Medicine and Pharmacy*, E. Matijević, Editor. 2012, Springer US: Boston, MA. p. 57-100. DOI: 10.1007/978-1-4614-0379-1_3.

4. Jha, S., R. Rani, and S. Singh, *Biogenic Zinc Oxide Nanoparticles and Their Biomedical Applications: A Review.* Journal of Inorganic and Organometallic Polymers and Materials, 2023. **33**(6): p. 1437-1452. DOI: 10.1007/s10904-023-02550-x.

5. Sharumathi, S., et al., *Copper oxide-anchored ZnO nanoflakes for the enhanced photocatalytic degradation performance and mechanistic investigations.* Physica B: Condensed Matter, 2023. **670**: p. 415336. DOI: https://doi.org/10.1016/j.physb.2023.415336.

6. Ye, L., et al., *The CuO and AgO co-modified ZnO nanocomposites for promoting wound healing in Staphylococcus aureus infection.* Mater Today Bio, 2023. **18**: p. 100552. DOI: 10.1016/j.mtbio.2023.100552.

7. Murthy, S., P. Effiong, and C.C. Fei, *11 - Metal oxide nanoparticles in biomedical applications*, in *Metal Oxide Powder Technologies*, Y. Al-Douri, Editor. 2020, Elsevier. p. 233-251. DOI: https://doi.org/10.1016/B978-0-12-817505-7.00011-7.

8. Tahergorabi, Z. and M. Khazaei, *A review on angiogenesis and its assays.* Iran J Basic Med Sci, 2012. **15**(6): p. 1110-26.

9. Richarz, N., A. Boada, and J.J.A.d.-s. Carrascosa, *Angiogenesis in dermatology–insights of molecular mechanisms and latest developments.* 2017. **108**(6): p. 515-523.

10. Ethiraj, A.S. and D.J. Kang, *Synthesis and characterization of CuO nanowires by a simple wet chemical method.* Nanoscale Research Letters, 2012. **7**(1): p. 70. DOI: 10.1186/1556-276X-7-70.

11. Das, I., et al., *Development, optimization and characterization of a two step sol–gel synthesis route for ZnO/SnO 2 nanocomposite.* Journal of Materials Science: Materials in Electronics, 2018. **29**: p. 4128-4135.

12. Bazant, P., et al., *Synthesis and effect of hierarchically structured Ag-ZnO hybrid on the surface antibacterial activity of a propylene-based elastomer blends.* Materials, 2018. **11**(3): p. 363.

13. Sirelkhatim, A., et al., *Review on zinc oxide nanoparticles: antibacterial activity and toxicity mechanism.* Nano-micro letters, 2015. **7**: p. 219-242.

14. Prabhu, S. and E.K. Poulose, *Silver nanoparticles: mechanism of antimicrobial action, synthesis, medical applications, and toxicity effects.* International nano letters, 2012. **2**: p. 1-10.

15. Amininezhad, S.M., et al., *The antibacterial activity of SnO 2 nanoparticles against Escherichia coli and Staphylococcus aureus.* Zahedan Journal of Research in Medical Sciences, 2015. **17**(9).

16. Hsueh, Y.-H., P.-H. Tsai, and K.-S. Lin, *pH-dependent antimicrobial properties of copper oxide nanoparticles in Staphylococcus aureus.* International journal of molecular sciences, 2017. **18**(4): p. 793.

17. Wang, L., C. Hu, and L. Shao, *The antimicrobial activity of nanoparticles: present situation and prospects for the future.* International journal of nanomedicine, 2017: p. 1227-1249.